

AN ABSTRACT OF THE DISSERTATION OF

Lynza H. Sprowl for the degree of Doctor of Philosophy in Chemical Engineering presented on May 9, 2018.

Title: Analyzing the Kinetics and Thermodynamics of Surface Reactions using Density Functional Theory

Abstract approved: _____

Líney Árnadóttir

The interactions of chemical species with a solid surface play a role in many everyday applications such as heterogeneous catalysis, corrosion, and degradation reactions. Understanding the reaction kinetics and thermodynamics via rate constants and equilibrium constants, which require knowledge of the adsorbed species' entropy, is essential for tuning these surface reaction mechanisms. To reach this goal, we developed a hindered translator and hindered rotor model for calculating the surface entropy and implemented it into two existing python packages for atomic simulation and reaction modeling analysis. We use density functional theory, a computational modeling technique for determining electronic structures at the atomic scale, to calculate surface entropies as well as surface reaction energies. One such reaction we consider is the dissociation of CO into atomic C and O, as a precursor to corrosion reactions in metals. The process of CO breakdown on twelve nickel-based alloy surfaces to make corrosive O and C adsorbates is explored to understand the effect of the alloying atom on the CO reaction energetics. Another surface reaction we consider is the electro-reductive degradation of an electrolyte solvent on the anode surface in lithium-ion batteries. The dissociation of fluoroethylene carbonate on two lithium silicide surfaces is explored to understand the mechanisms and energetics of the degradation reaction and to understand the role of different battery charge states on the reaction. Altogether, these studies serve to advance the field of surface science.

©Copyright by Lynza H. Sprowl
May 9, 2018
All Rights Reserved

Analyzing the Kinetics and Thermodynamics of
Surface Reactions using Density Functional Theory

by
Lynza H. Sprowl

A DISSERTATION

submitted to

Oregon State University

in partial fulfillment of
the requirements for the
degree of

Doctor of Philosophy

Presented May 9, 2018
Commencement June 2018

Doctor of Philosophy dissertation of Lynza H. Sprowl presented on May 9, 2018

APPROVED:

Major Professor, representing Chemical Engineering

Head of the School of Chemical, Biological and Environmental Engineering

Dean of the Graduate School

I understand that my dissertation will become part of the permanent collection of Oregon State University libraries. My signature below authorizes release of my dissertation to any reader upon request.

Lynza H. Sprowl, Author

ACKNOWLEDGEMENTS

Thank you to everyone who has had an impact on my education. From my kindergarten teacher to my graduate advisor and everyone in between, I thank you. This dissertation is a product of all you have taught me and pushed me to learn.

Thank you Líney Árnadóttir for being a wonderful advisor and for helping develop me into the scientist I am today. Thank you to everyone who has ever been on my committee for your guidance and support – Greg Herman, Chih-hung Chang, Brady Gibbons, Nick AuYeung, Zhenxing Feng, and Alex Greaney. Thank you to all of my research group members, past and present, who have helped me along the way – Qin Pang, Dennis Petersen, Kofi Oware Sarfo, Kingsley Chukwu, Sean Seekins, Yousif Almulla, Ashaen Patel, Alvin Chang, Merissa Schneider-Coppolino, Jimmy Beaty, Weinan Zhao, and Jie Zhou.

Thank you Maria Chan at Argonne National Laboratory for accepting me into your group for a year. You are an amazing advisor and mentor and I learned so much. Thank you to everyone in the group at Argonne for sharing your time and wisdom – Joseph Kubal, Spencer Hills, Kendra Letchworth-Weaver, Liang Li, Fatih Sen, Yasaman Ghadar, Eric Schwenker, Yi Xia, and Arun Mannodi Kanakkithodi.

Thank you Alyssa Deline, Grace Panther, and Hannah Rolston for working with me to improve fellowship application material, encouraging me to be a better graduate student, and having fun along the way. I also thank Paul LeDuff, Chris and Greta Brueck, Omar Chiriboga, Ramya Raman, and Thaddeus Golbek for your friendship through the years. It has been a great ride.

Thank you to my parents, Tom and Cathi Halberstadt, for your love and support. Thank you to my siblings, Weston, Jaret, and Isaac, for always being there and always challenging me. Thank you Sam Bartling and Barrett Rosteck for becoming family during my time in Corvallis and thank you Cooper Bartling for allowing me to be a kid whenever I want. Last, but certainly not least, thank you Lauren Sprowl for all you do for me, as I cannot say how much it all means.

CONTRIBUTION OF AUTHORS

Chapter 3 develops a hindered translator and hindered rotor model and tests the model using density functional theory calculations. I assisted in development of the model, performed all the calculations, and wrote the first draft of the manuscript. Charles T. Campbell and Líney Árnadóttir guided the model development and assisted in preparing and editing the manuscript.

Chapter 4 summarizes applications of the hindered translator model and implements the hindered translator and hindered rotor model into two commonly used atomistic modeling codes. I summarized the literature on the hindered translator and wrote all the hindered translator and hindered rotor code that went into the two existing python packages.

Chapter 5 analyzes the impact of an alloying atom in a nickel surface on the breakdown of carbon monoxide to better understand corrosion in nickel-based alloys. I performed all the calculations, analyzed the results, and wrote the first draft of the manuscript. Julie D. Tucker, Benjamin M. Adam, and Líney Árnadóttir assisted in experimental design, interpretation of results, and manuscript editing.

Chapter 6 investigates the breakdown of fluoroethylene carbonate on lithium silicide surfaces to understand what happens in lithium-ion batteries. I developed the research idea and wrote the DOE-SCGSR proposal to get funding for the project. I performed all the calculations, analyzed the results, and wrote the first draft of the manuscript. Maria K. Y. Chan and Líney Árnadóttir assisted in proposal editing, experimental design, interpretation of results, and manuscript editing.

TABLE OF CONTENTS

	<u>Page</u>
CHAPTER 1: INTRODUCTION	1
General Introduction	2
Surface Entropy Modeling	4
Corrosion Resistant Metals	7
Lithium-Ion Battery Anodes	8
References	9
CHAPTER 2: COMPUTATIONAL TECHNIQUES	11
Density Functional Theory	12
Van der Waals Corrections	17
Vienna Ab-initio Simulation Package	17
Nudged Elastic Band	18
Vibrational Frequency Analysis	19
Density of States Analysis	21
Bader Charge Analysis	22
References	22
CHAPTER 3: HINDERED TRANSLATOR AND HINDERED ROTOR MODELS FOR ADSORBATES: PARTITION FUNCTIONS AND ENTROPIES	26
Abstract	27
Introduction	28
Theory	31
Ideal 2D Hindered Translator: Partition Function	31
Hindered Rotor: Partition Function	35

TABLE OF CONTENTS (Continued)

	<u>Page</u>
Thermodynamic Functions	37
Computational Methods.....	42
Results and Discussion	44
Comparison of Predicted Entropies of Small Adsorbates on Pt(111) to Experiments	44
Dependence of Adsorbate Entropy on System Parameters.....	54
Conclusions.....	58
Acknowledgements.....	59
References.....	59
Supporting Information.....	62
CHAPTER 4: APPLICATIONS OF THE HINDERED TRANSLATOR AND HINDERED ROTOR MODEL	69
Introduction.....	70
Discussion.....	71
Conclusions.....	78
Code for Atomic Simulation Environment.....	79
Documentation	79
Code	80
Example	85
Code for Catalysis Microkinetic Analysis Package.....	87
Documentation.....	88
Code	88

TABLE OF CONTENTS (Continued)

	<u>Page</u>
References.....	91
CHAPTER 5: FIRST-PRINCIPLES STUDY OF THE PRODUCTS OF CO₂ DISSOCIATION ON NICKEL-BASED ALLOYS: TRENDS IN ENERGETICS WITH ALLOYING ELEMENTS.....	93
Abstract.....	94
Introduction.....	95
Methods.....	97
Computational Details	97
Surface Models	98
Results and Discussion	101
Oxygen Binding.....	101
Carbon Binding.....	106
Carbon Monoxide Binding	111
Alloying Atom Effect	114
Carbon Monoxide Reactions.....	120
Conclusions.....	125
Acknowledgements.....	127
References.....	127
Supporting Information.....	134
CHAPTER 6: FLUOROETHYLENE CARBONATE BREAKDOWN MECHANISMS AND ENERGETICS ON TWO LITHIUM SILICIDE SURFACES	142
Abstract.....	143

TABLE OF CONTENTS (Continued)

	<u>Page</u>
Introduction.....	144
Methods.....	148
Results and Discussion	151
Determining the Most Stable LiSi and Li ₁₅ Si ₄ Surfaces.....	151
Determining the Most Stable Fluoroethylene Carbonate Binding Configurations.....	153
Setting up the Surface Mesh	154
Fluoroethylene Carbonate on LiSi	156
Fluoroethylene Carbonate on Li ₁₅ Si ₄	159
Comparing Fluoroethylene Carbonate Reduction on LiSi and Li ₁₅ Si ₄	163
Conclusions.....	165
Acknowledgements.....	165
References.....	166
CHAPTER 7: CONCLUSION	170
General Conclusions	171
Future Work	173
References.....	175

LIST OF FIGURES

<u>Figure</u>	<u>Page</u>
1.1	Reaction scheme with and without a catalyst2
2.1	Progression from considering all electrons in the many-body Schrödinger equation to considering the electron density with the Kohn-Sham equations as is done with density functional theory.....14
2.2	Schematic of the density functional theory process.....16
3.1	Example potential energy surface for adsorbate motions parallel to the surface30
3.2	Quantum harmonic oscillator and hindered translator partition functions35
3.3	Calculated energy barrier versus coordinate of different adsorbates on Pt(111) for hindered translations and hindered rotations.....47
3.4	Entropy contributions as a function of temperature for two hindered translations, the hindered rotation, the $3n-3$ vibrations, and the total entropy48
3.5	Plot of standard-state entropies determine for different adsorbates on Pt(111).....51
3.6	Effect of system parameters on the translational contribution to the entropy as determined from a hindered translator and compared with a harmonic oscillator and a free translator.....55
3.7	Effect of system parameters on the rotational contribution to the entropy as determined from a hindered rotor and compared with a harmonic oscillator and a free rotor57
3.S1	Initial state and transition state binding configurations for methanol on Pt(111) with and without van der Waals corrections.....64
3.S2	Initial state and transition state binding configurations for propane (C2) on Pt(111) with and without van der Waals corrections.....65
3.S3	Initial state and transition state binding configurations for propane (C1) on Pt(111) with and without van der Waals corrections.....66
3.S4	Initial state and transition state binding configurations for ethane on Pt(111) with and without van der Waals corrections.....67

LIST OF FIGURES (Continued)

<u>Figure</u>	<u>Page</u>
3.S5 Initial state and transition state binding configurations for methane on Pt(111) with and without van der Waals corrections.....	68
4.1 The one-dimensional potential energy surface as approximated by the harmonic oscillator, hindered translator, and free translator models.....	72
5.1 Unique binding sites on the (100) and (111) facets	99
5.2 Binding energy of C, CO, and O adsorbates versus the shift in d-band center of the alloyed (100) and (111) surfaces.....	119
5.3 Binding energies of CO dissociation reactants and products relative to CO in the gas phase on the (100) and (111) facets of Ni surfaces alloyed with the indicated elements.....	122
5.4 Binding energies of reactants and products in the Boudouard reaction relative to two gas phase CO molecules on the (100) and (111) facets of Ni surfaces alloyed with the indicated elements.....	124
5.S1 Binding energies of CO ₂ breakdown steps via CO dissociation relative to gas phase CO ₂ on the (100) facet of Ni surfaces alloyed with the indicated elements	140
5.S2 Binding energies of CO ₂ breakdown steps via CO dissociation relative to gas phase CO ₂ on the (111) facet of Ni surfaces alloyed with the indicated elements	140
5.S3 Binding energies of CO ₂ breakdown steps via the Boudouard reaction relative to gas phase CO ₂ on the (100) facet of Ni surfaces alloyed with the indicated elements.....	141
5.S4 Binding energies of CO ₂ breakdown steps via the Boudouard reaction relative to gas phase CO ₂ on the (111) facet of Ni surfaces alloyed with the indicated elements.....	141
6.1 Schematic of a lithium-ion battery with a silicon anode.....	144
6.2 Fluoroethylene carbonate skeletal formula and atomic model with labels to differentiate each individual atom	146
6.3 Representations of the five calculated low-index surface facets of LiSi	152

LIST OF FIGURES (Continued)

<u>Figure</u>	<u>Page</u>
6.4	Representations of the three calculated low-index surface facets of $\text{Li}_{15}\text{Si}_4$.153
6.5	Side views of the initial FEC binding configurations and final most stable binding configurations for FEC on LiSi and $\text{Li}_{15}\text{Si}_4$154
6.6	Top views of the 1 x 1 Ångstrom surface mesh employed across the LiSi and $\text{Li}_{15}\text{Si}_4$ surfaces to determine where FEC binds.....155
6.7	Molecular structure representations as fluoroethylene carbonate dissociates155
6.8	Final FEC configurations on LiSi after starting with FEC in the F-up configuration and F-down configuration156
6.9	Binding configurations of FEC as it dissociates on the LiSi surface.....157
6.10	Final FEC configurations on $\text{Li}_{15}\text{Si}_4$ after starting with FEC in the angled configuration with O_1 down and F up.....160
6.11	Binding configurations of FEC as it dissociates on the $\text{Li}_{15}\text{Si}_4$ surface.....161
6.12	Density of states plots of intact FEC on the LiSi and $\text{Li}_{15}\text{Si}_4$ surfaces before charge transfer or decomposition occurs164

LIST OF TABLES

<u>Table</u>	<u>Page</u>
1.1	Translational, rotational, and vibrational degrees of freedom for chemical species composed of one, two, or three atoms.....6
3.1	Summary of hindered translator data for several adsorbates on Pt(111)45
3.2	Summary of hindered rotor data for several adsorbates on Pt(111)46
3.3	Separation of the entropy contributions to the standard-state molar entropy of the probe adsorbates on Pt(111)50
3.S1	Binding energies, in eV, of the initial state, translational transition state, and rotational transition state on a Pt(111) surface.....62
3.S2	Distances, in Ångstroms, between O and C atoms and the Pt(111) surface for the initial state, translational transition state, and rotational transition state configurations63
4.1	Prefactors for the CO oxidation reaction mechanism on Pt(111) using the harmonic oscillator, hindered translator, free translator, and potential energy sampling models compared to experiments78
5.1	Effects of substituting an alloying atom for a single Ni surface atom on oxygen adsorption.....103
5.2	Summary and comparison to previous studies of the change in binding energy, ΔE_{bind} , of atomic O on (111) Ni-based alloy surfaces compared to a pure Ni(111) bulk/surface105
5.3	Effects of substituting an alloying atom for a single Ni surface atom on carbon adsorption.....108
5.4	Summary and comparison to previous studies of the change in binding energy, ΔE_{bind} , of atomic C on (111) Ni-based alloy surfaces compared to a pure Ni(111) bulk/surface110
5.5	Effects of substituting an alloying atom for a single Ni surface atom on carbon monoxide adsorption.....112
5.6	Summary and comparison to previous studies of the change in binding energy, ΔE_{bind} , of CO on (111) Ni-based alloy surfaces compared to a pure Ni(111) bulk/surface114

LIST OF TABLES (Continued)

<u>Table</u>	<u>Page</u>
5.7	Effects of substituting an alloying atom for a single Ni surface atom on the d-band of the top surface layer for the (100) and (111) facets.....116
5.8	Binding energy range, eV, of O, C, and CO over the twelve alloy surfaces at each unique hollow site.....118
5.9	Effects of substituting an alloying atom for a single Ni surface atom on CO dissociation reaction energies on the (100) and (111) facets of Ni-based alloys.....121
5.10	Effects of substituting an alloying atom for a single Ni surface atom on Boudouard reaction energies on the (100) and (111) facets of Ni-based alloys123
5.S1	Binding energies, in eV, for O adsorption on Ni-based alloy (100) surfaces 134
5.S2	Binding energies, in eV, for O adsorption on Ni-based alloy (111) surfaces 135
5.S3	Binding energies, in eV, for C adsorption on Ni-based alloy (100) surfaces 136
5.S4	Binding energies, in eV, for C adsorption on Ni-based alloy (111) surfaces 137
5.S5	Binding energies, in eV, for CO adsorption on Ni-based alloy (100) surfaces138
5.S6	Binding energies, in eV, for CO adsorption on Ni-based alloy (111) surfaces139
6.1	Surface energies, in J/m ² , of the low-index LiSi surface facets.....152
6.2	Surface energies, in J/m ² , of the low-index Li ₁₅ Si ₄ surface facets, including the (100) facet with a surface Si atom exchanged for a subsurface Li atom.....153
6.3	Bader charge, e , and binding energy, eV, of FEC and its breakdown products on LiSi.....158
6.4	Bader charge, e , and binding energy, eV, of FEC and its breakdown products on Li ₁₅ Si ₄162

CHAPTER 1
INTRODUCTION

General Introduction

The field of surface science got its start with applications in heterogeneous catalysis, but has since been expanded to include many more applications such as semiconductor fabrication, film growth, corrosion, and degradation reactions. Chemical reactions at solid surfaces occur as an alternative to gas phase or liquid phase reactions because the surface can stabilize the chemical species and facilitating the reaction. The catalytic surface breaks the reaction down into elementary steps and lowers the kinetic energy barriers of the reaction, resulting in a different and more facile chemical reaction mechanism, as shown in Figure 1.1.

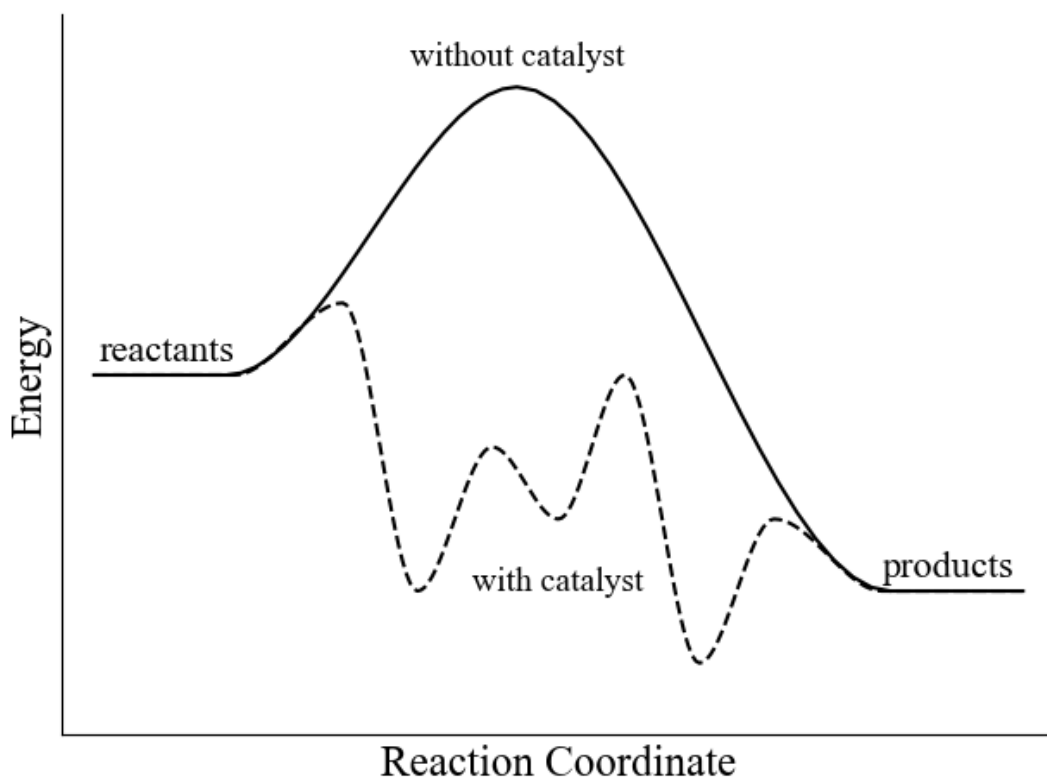


Figure 1.1 Reaction scheme with and without a catalyst.

Surface reactions have a long history that started over a century ago. In the 1880s and 1890s, the Germany company BASF discovered that platinum could be used to facilitate the oxidation reaction of sulfur dioxide to sulfur trioxide,



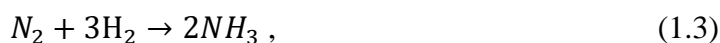
This reaction is the key step in the commercial manufacturing of sulfuric acid, which is known as the universal chemical because of its wide use in almost every chemical industry [1].

Soon after, around 1897, Paul Sabatier developed a method of adding hydrogen to carbon compounds, for a reaction such as



using a nickel catalyst in a simple, safe, and convenient manner. This reaction method allows unsaturated organic substances to absorb hydrogen and is used in many industrial processes such as converting liquid oils into solid fats, as is done when producing margarine. Paul Sabatier was awarded a share of the Nobel Prize in 1912 “for his method of hydrogenating organic compounds in the presence of finely disintegrated metals whereby the progress of organic chemistry has been greatly advanced in recent years” [2].

After the turn of the century, around 1913, Fritz Haber developed a process of fixing nitrogen from the air and reacting it with hydrogen to make ammonia,



by using an iron oxide catalyst. Ammonia production is necessary for making fertilizer and explosives, for which the German Fritz Haber had initially intended in World War I, and controversially led to Fritz Haber receiving a Nobel Prize in 1918 “for the synthesis of ammonia from its elements” [3].

Other Nobel Prize winners in surface science include Irving Langmuir, who in 1932 received a Nobel Prize “for his discoveries and investigations in surface chemistry” [4], and Gerhard Ertl, who in 2007 was awarded a Nobel Prize “for his studies of chemical processes on solid surfaces” [5]. Clearly, surface reactions and surface science have a long history that is still very much relevant today.

Surface Entropy Modeling

Any introductory thermodynamics textbook [6] is apt to discuss the kinetics and thermodynamics of a chemical reaction. The thermodynamics of a process relate to the change in energy between the reactants and products and can be understood through an equilibrium constant. The kinetics of a reaction relate to the energy barriers that must be overcome for reactants to become products and can be understood through a rate constant.

The equilibrium constant for a chemical reaction relates the concentration of products to the concentration of reactants and is used to determine what the final reaction concentrations will be. The equilibrium constant, K_{eq} , is given by

$$K_{eq} = \exp \left[\frac{-\Delta G}{RT} \right], \quad (1.4)$$

where ΔG is the change in Gibbs free energy between the reactants and products, R is the gas constant, and T is the temperature. The Gibbs free energy change is given by

$$\Delta G = \Delta H - T\Delta S, \quad (1.5)$$

where ΔH is the change in enthalpy and ΔS is the change in entropy between reactants and products.

The rate constant for a chemical reaction relates the rate of the reaction to the concentration of the reactants and is used to determine the speed of a chemical reaction. The rate constant, k , is given by the Arrhenius equation as

$$k = A \exp \left[\frac{-E_a}{RT} \right], \quad (1.6)$$

where A is called the frequency factor, pre-exponential factor, or simply the prefactor and E_a is the activation energy of the reaction. The rate constant depends on the frequency of collision, incorporated into the prefactor, and the energy of the collision, indicated by the activation energy. The prefactor is defined as

$$A = \frac{k_B T}{h} \exp \left[\frac{\Delta S}{R} \right], \quad (1.7)$$

where k_B is the Boltzmann constant, h is Planck's constant, and ΔS here is the change in entropy between the reaction transition state and the initial state.

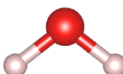
The partition function of a system is an equation that can express all macroscopic properties of the system, such as the free energy, pressure, chemical potential, heat capacity, and entropy. From the partition function, Q , the entropy is calculated as

$$S = \frac{d}{dT} [k_B T \ln Q]. \quad (1.8)$$

The partition function can be divided into a translational term, rotational term, and vibrational term corresponding to the degrees of freedom of the chemical species.

Every N -atomic species has $3N$ degrees of freedom, with the degrees of freedom for four small, simple chemical species indicated in Table 1.1. Three of the degrees of freedom correspond to translational motion of the center of mass and are referred to as translational degrees of freedom. Additional degrees of freedom correspond to rotational motion about the three perpendicular axes and are referred to as rotational degrees of freedom. A single atom has zero rotational degrees of freedom (as any rotation does not change the atomic position), a linear molecule has two rotational degrees of freedom (in the two axes perpendicular to the axis of the molecule), and a nonlinear molecule has three rotational degrees of freedom. The remaining degrees of freedom correspond to internal vibrations of the molecule such as symmetric stretching, antisymmetric stretching, bending, rocking, wagging, or twisting motions and are referred to as vibrational degrees of freedom. A single atom has zero vibrational degrees of freedom, a linear molecule has $3N-5$ vibrational degrees of freedom, and a nonlinear molecule has $3N-6$ vibrational degrees of freedom. The vibrational degrees of freedom are normal modes and contribute to the partition function through their vibrational frequency.

Table 1.1 Translational, rotational, and vibrational degrees of freedom for chemical species composed of one, two, or three atoms.

Chemical Species	Example	Degrees of Freedom
1 atom		Trans: x, y, z
2 atoms		Trans: x, y, z Rot: x, y Vib: stretch
3 atoms linear		Trans: x, y, z Rot: x, y Vib: x-axis bend, y-axis bend, symmetric stretch, antisymmetric stretch
3 atoms nonlinear		Trans: x, y, z Rot: x, y, z Vib: bend, symmetric stretch, antisymmetric stretch

A chemical species adsorbed on a surface still has $3N$ degrees of freedom, but now a bond exists between the adsorbate and the surface, limiting the motion of the adsorbate. The simplest way to model an adsorbate is to assume that it is stuck in a potential energy well on the surface and replace the translational and rotational modes with vibrational modes corresponding to frustrated translations and rotations. This model of only considering vibrational modes for adsorbates is referred to as the 2D ideal lattice gas model or the harmonic oscillator approximation. The harmonic oscillator approximation is commonly used with density functional theory calculations to determine the partition function, and ultimately the entropy, from the $3N$ vibrational frequencies of the adsorbate.

Although the harmonic oscillator approximation is simple and (in theory) easy to use, it still has problems. One challenge is that density functional theory overestimates the vibrational frequencies that model the frustrated translational and rotational frequencies, which in turn underestimates the entropy [7, 8]. Another

problem is that it is challenging using density functional theory to get the lowest vibrational frequencies, which are the frequencies corresponding to the translational and rotational modes. Minor movements of the adsorbate, which have almost no effect on the energy of the system, can have a big effect on the lowest frequencies by giving different frequency values or giving imaginary frequencies. Imaginary frequencies, which indicate that the adsorbate is not in its true energy minimum state, cannot be used in the harmonic oscillator approximation and determining an absolute minima without imaginary frequencies can be challenging. The smallest frequencies also contribute the most to the entropy, so small fluctuations in these frequencies can lead to large differences in the entropy.

The harmonic oscillator approximation is applicable in the low temperature limit when the adsorbate does not have enough energy to get out of the potential energy well in which it sits on the surface. In this case, the adsorbate does not have enough energy to translate or rotate and can only vibrate. The other extreme is the high temperature limit in which the adsorbate has sufficient energy to escape the potential energy well on the surface. In this case the adsorbate can easily translate and rotate on the surface, and the three modes of motion parallel to the surface (two for linear adsorbates and single atoms) are modeled as free translators and (if applicable) a free rotor. This model is called the 2D ideal gas model or the free translator model.

We have developed a model, called the hindered translator, which bridges the gap between the harmonic oscillator approximation and the free translator model. The hindered translator considers motion parallel to the surface as hindered translations and hindered rotations instead of vibrations, as in the harmonic oscillator approximation, or as free translator and free rotors, as in the free translator model. This model is developed and discussed in Chapter 3 and then is benchmarked and implemented as computer code for easy access by other researchers in Chapter 4.

Corrosion Resistant Metals

One example of thermodynamics and kinetics that has practical applications is the breakdown of a chemical species on a metal surface to atomic carbon or atomic oxygen, which can react with the metal and cause corrosion. An example of this is

corrosion by the working fluid in a power plant on the metal structural material that make up a power plant. The working fluid in a power plant is typically steam because water is abundantly available, it is environmentally benign, and it is for the most part chemically inert, aside from corrosion. An alternative to steam as the working fluid in a power plant is to use supercritical CO₂ as the working fluid. Compared to conventional steam power production cycles, supercritical CO₂ cycles offer an improved plant efficiency due to less compressive work because of higher CO₂ densities, lower cost, reduced emissions, fewer and smaller energy conversion components, and a simpler cycle layout [9, 10].

One challenge with implementing supercritical CO₂ into power plants is the identification and development of metals for structural support that will not corrode in supercritical CO₂ environments. There are many commercially available nickel-based alloys that are being tested for this application [10-15], and the effect of each alloying element on the breakdown of CO₂ dissociation products is investigated in Chapter 5. The power plants operate at a high temperature of 650-800°C, so the surface reactions are considered to be in a thermodynamic regime and not a kinetic regime.

Lithium-Ion Battery Anodes

Another example of thermodynamics and kinetics with a practical application is the breakdown of electrolyte in a lithium-ion battery. Lithium-ion batteries are being designed with higher energy densities and longer lifetimes due to increasing demands from consumers. The current anode in a lithium-ion battery is graphite, however silicon is seen as a promising new anode material because it can store over ten times more lithium than graphite on a per mass basis, which increases the energy density of the battery.

Due to the high operating potentials of a battery, the organic electrolyte solvent, which conducts the lithium ions back and forth between the anode and cathode, breaks down at the anode surface and forms a so-called solid-electrolyte interphase. The solid-electrolyte interphase consumes lithium ions, resulting in a fewer number of lithium ions that are available to reach the anode to charge the battery. The solid-electrolyte interphase should also be ionically conductive so that

the Li^+ ions can easily diffuse through to reach the anode. This is not always the case, so different electrolyte additives are included in the electrolyte composition that break down differently to form a better solid-electrolyte interphase. Understanding how the solid-electrolyte interphase forms from the electrolyte breakdown is important for designing and selecting future electrolyte additives and is investigated in Chapter 6.

References

- [1] J.H. Sinfelt, Role of Surface Science in Catalysis, *Surface Science*, 500 (2002) 923-946.
- [2] The Nobel Prize in Chemistry 1912, Nobelprize.org, Nobel Media AB 2014, https://www.nobelprize.org/nobel_prizes/chemistry/laureates/1912/.
- [3] The Nobel Prize in Chemistry 1918, Nobelprize.org, Nobel Media AB 2014, https://www.nobelprize.org/nobel_prizes/chemistry/laureates/1918/.
- [4] The Nobel Prize in Chemistry 1932, Nobelprize.org, Nobel Media AB 2014, https://www.nobelprize.org/nobel_prizes/chemistry/laureates/1932/.
- [5] The Nobel Prize in Chemistry 2007, Nobelprize.org, Nobel Media AB 2014, https://www.nobelprize.org/nobel_prizes/chemistry/laureates/2007/.
- [6] D.A. McQuarrie, J.D. Simon, *Molecular Thermodynamics*, University Science Books 1999.
- [7] C.T. Campbell, J.R.V. Sellers, The Entropies of Adsorbed Molecules, *Journal of the American Chemical Society*, 134 (2012) 18109-18115.
- [8] C.T. Campbell, L. Arnadottir, J.R.V. Sellers, Kinetic Prefactors of Reactions on Solid Surfaces, *Zeitschrift Fur Physikalische Chemie-International Journal of Research in Physical Chemistry & Chemical Physics*, 227 (2013) 1435-1454.
- [9] M. Mecheri, Y. Le Moullec, Supercritical CO_2 Brayton Cycles for Coal-Fired Power Plants, *Energy*, 103 (2016) 758-771.
- [10] V. Firouzdor, K. Sridharan, G. Cao, M. Anderson, T.R. Allen, Corrosion of a Stainless Steel and Nickel-Based Alloys in High Temperature Supercritical Carbon Dioxide Environment, *Corrosion Science*, 69 (2013) 281-291.
- [11] R.G. Brese, J.R. Keiser, B.A. Pint, Effect of Thermal Cycling on Compatibility in CO_2 for Concentrated Solar Power Applications, *Oxidation of Metals*, 87 (2017) 631-642.
- [12] R.I. Olivares, W. Stein, T.D. Nguyen, D.J. Young, *Corrosion of Nickel-Base Alloys by Supercritical CO_2* , 2016.
- [13] R.I. Olivares, D.J. Young, P. Marvig, W. Stein, Alloys SS316 and Hastelloy-C276 in Supercritical CO_2 at High Temperature, *Oxidation of Metals*, 84 (2015) 585-606.

- [14] B.A. Pint, R.G. Brese, J.R. Keiser, Effect of Pressure on Supercritical CO₂ Compatibility of Structural Alloys at 750 Degrees C, *Materials and Corrosion*, 68 (2017) 151-158.
- [15] B.A. Pint, J.R. Keiser, Initial Assessment of Ni-Base Alloy Performance in 0.1 MPa and Supercritical CO₂, *Jom*, 67 (2015) 2615-2620.

CHAPTER 2
COMPUTATIONAL TECHNIQUES

Density Functional Theory

Density functional theory is a technique based on quantum mechanics that is used to understand the electronic structure of matter. The goal of density functional theory is to calculate the electron density that corresponds to the ground-state of a chemical system, from which a complete description of the chemical properties can be determined. Density functional theory calculations are often used to compliment experimental studies, to gain insights not accessible by experimental methods, when quantum mechanical-modeling is quicker and safer, or when an experimental apparatus is much more expensive than a computer. Density functional theory is a well-established computational technique, with many excellent and extensive reviews on the topic [1-7].

Quantum mechanical-modeling is based on the Schrödinger equation,

$$\hat{H}\psi = E\psi, \quad (2.1)$$

where \hat{H} is the Hamiltonian operator, E is the total ground-state energy of the system, and ψ is the wavefunction, written here as the time-independent wavefunction, which describes the position and state of the quantum system. The quantum system may be comprised of one particle, such as a particle in a box, or comprised of many particles, such as an atom containing a nucleus and electrons.

The time-independent Hamiltonian in a many-body system of electrons and nuclei is

$$\hat{H} = \underbrace{-\sum_i \frac{\hbar}{2m_e} \nabla_i^2}_{T_e} - \underbrace{\sum_I \frac{\hbar^2}{2M_I} \nabla_I^2}_{T_n} - \underbrace{\sum_{i,I} \frac{Z_I e^2}{|\mathbf{r}_i - \mathbf{R}_I|}}_{V_{en}} + \underbrace{\sum_{i>j} \frac{e^2}{|\mathbf{r}_i - \mathbf{r}_j|}}_{V_{ee}} + \underbrace{\sum_{I>J} \frac{Z_I Z_J e^2}{|\mathbf{R}_I - \mathbf{R}_J|}}_{V_{nn}}, \quad (2.2)$$

where i and j are indices for electrons, I and J are indices for nuclei, ∇^2 is the Laplacian, \hbar is the reduced Planck's constant, m_e is the mass of an electron, M_I is the mass of the I -th nucleus, Z_I is the charge of the I -th nucleus, \mathbf{r}_i is the position of the i -th electron, and \mathbf{R}_I is the position of the I -th nucleus. The Hamiltonian is composed of five terms: a kinetic energy term for the electrons (T_e), a kinetic energy term for

the nuclei (T_n), a potential energy term for the Coulombic interactions between electrons and nuclei (V_{en}), a potential energy term for the Coulombic interactions between electrons and electrons (V_{ee}), and a potential energy term for the Coulombic interactions between nuclei and nuclei (V_{nn}).

The adiabatic approximation, or the so-called Born-Oppenheimer approximation [8] simplifies the many-body Hamiltonian by uncoupling the electronic positions from the nuclear positions. This approximation stems from the fact that electrons are much less massive than nuclei and therefore it can be assumed that electrons respond essentially instantaneously to movement of the nuclei. The Born-Oppenheimer approximation neglects motion of the nuclei and treats them as fixed particles. This simplifies the problem by reducing the Hamiltonian from one with electrons and nuclei to one with only electrons in a field of fixed nuclei. Under this approximation, the T_n term goes to zero, the V_{nn} term becomes a constant, and the V_{en} term becomes dependent only on the position of the electrons in an external nuclei potential field. The electronic Hamiltonian, ignoring the constant V_{nn} term, is now

$$\hat{H}_{el} = \underbrace{-\sum_i \frac{\hbar}{2m_e} \nabla_i^2}_{T_e} - \underbrace{\sum_i V_{ext}(\mathbf{r}_i)}_{V_{en}} + \underbrace{\sum_{i>j} \frac{e^2}{|\mathbf{r}_i - \mathbf{r}_j|}}_{V_{ee}}, \quad (2.3)$$

where V_{ext} is the external nuclei potential field experienced by the electrons.

Density functional theory was born in 1964-1965 after two seminal papers by Hohenberg, Kohn, and Sham [9, 10] in an attempt to solve for the wavefunction. Hohenberg and Kohn [9] started by establishing two theorems upon which density functional theory is built. The first theorem states that the external potential, V_{ext} , is a unique functional of the electron density. The remaining T_e and V_{ee} terms in the Hamiltonian are the same for a given N -electron system, hence the Hamiltonian is completely defined by V_{ext} and the number of electrons, N . Therefore, the first theorem states that the full many-body ground state is a unique functional of the electron density. The second theorem states that the electron density that minimizes the total energy is the exact ground state density. What these theorems do not state though, is how to find the electron density.

Kohn and Sham [10] later formulated the Kohn-Sham equations to determine the electron density and ground state energy. Using the electron density simplifies the many-body problem from one with $3N$ variables, corresponding to the three directions of all N electrons, to a problem with 3 variables, corresponding to the three dimensions of the electron density. A representation of moving from the many-body perspective to the density functional theory perspective is shown in Figure 2.1.

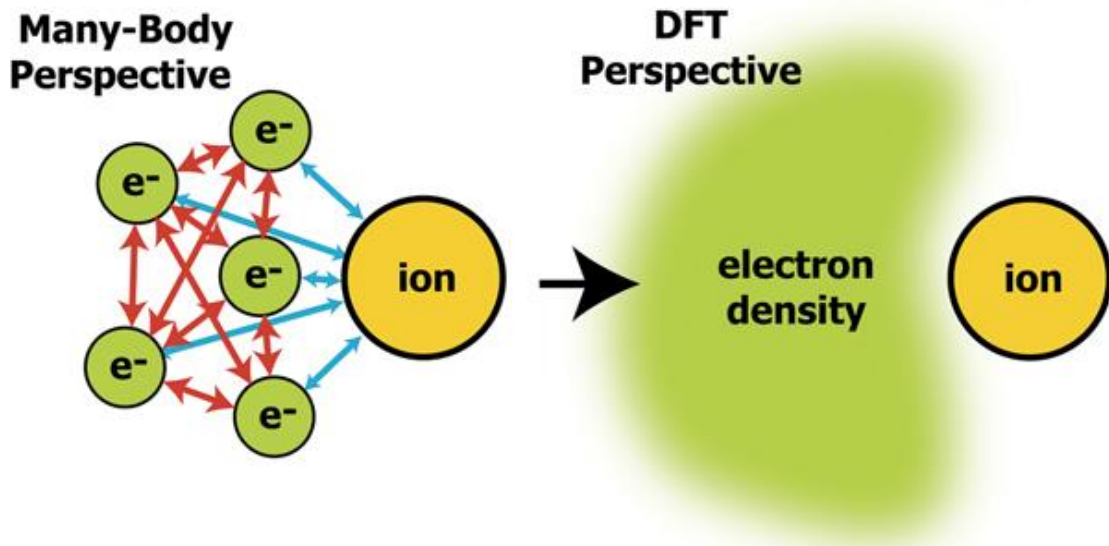


Figure 2.1 Progression from considering all electrons in the many-body Schrödinger equation to considering the electron density with the Kohn-Sham equations as is done with density functional theory (DFT). Figure reproduced with permission from ref [11].

The Kohn-Sham equation is

$$\left[\frac{-\hbar^2}{2m} \nabla^2 + V_{KS}(\mathbf{r}) \right] \psi_i(\mathbf{r}) = \epsilon_i \psi_i(\mathbf{r}) . \quad (2.4)$$

where V_{KS} is the Kohn-Sham potential, which equals

$$V_{KS}(\mathbf{r}) = V_{ext}(\mathbf{r}) + V_H(\mathbf{r}) + V_{XC}(\mathbf{r}) . \quad (2.5)$$

The first term of the Kohn-Sham potential represents the external nuclei potential field experienced by the electrons, the second term is the Hartree potential, defined as

$$V_H(\mathbf{r}) = \int d\mathbf{r}' \frac{n(\mathbf{r}')}{|\mathbf{r}-\mathbf{r}'|}, \quad (2.6)$$

and the last term is the exchange and correlation potential, defined as

$$V_{XC}(\mathbf{r}) = \frac{\partial E_{xc}[n(\mathbf{r})]}{\partial n(\mathbf{r})}. \quad (2.7)$$

The exchange and correlation potential is simply the derivative of the exchange-correlation energy, which contains all of the terms that have an unknown form.

The exact solution to the exchange and correlation energy is unknown, and therefore must be approximated. One approximation to solve for E_{XC} is the local density approximation, which treats the electron density locally as a uniform gas. In the local density approximation (LDA), the exchange-correlation energy is represented as

$$E_{XC}^{LDA} = \int \epsilon_{XC}(n(\mathbf{r}))n(\mathbf{r})d^3r, \quad (2.8)$$

where ϵ_{XC} is the exchange-correlation energy per electron of the homogeneous electron gas, which can be computed exactly. An extension of the local density approximation is the local spin-density approximation, which considers the different electron spin states. The local spin-density approximation (LSDA) is

$$E_{XC}^{LSDA} = \int \epsilon_{XC}(n_{\uparrow}(\mathbf{r}), n_{\downarrow}(\mathbf{r}))n(\mathbf{r})d^3r, \quad (2.9)$$

where the up and down arrows account for the up and down spins of the electrons.

An improved approximation to E_{XC} is the generalized gradient approximation [12, 13], which is similar to the local spin-density approximation but also considers the gradient of the electron density in the exchange-correlation energy per electron. In the generalized gradient approximation (GGA), the exchange-correlation energy is

$$E_{XC}^{GGA} = \int \epsilon_{XC}(n_{\uparrow}(\mathbf{r}), n_{\downarrow}(\mathbf{r}), \nabla n_{\uparrow}(\mathbf{r}), \nabla n_{\downarrow}(\mathbf{r}))n(\mathbf{r})d^3r. \quad (2.10)$$

where ∇n is the gradient of the electron density. Multiple generalized gradient approximations exist to estimate the exchange-correlation energy, with the two most popular being the PW91 functional by Perdew and Wang [14], and the PBE functional by Perdew, Burke, and Ernzerhof [15, 16].

After an appropriate exchange-correlation approximation is chosen, the Kohn-Sham equations can be solved to find the electron density and the energy of the system. The electron density is solved by iteratively guessing an electron density, calculating the Kohn-Sham potential, solving the Kohn-Sham equation, and calculating the electron density from the wavefunction as

$$n(\mathbf{r}) = 2 \sum_i |\psi_i(\mathbf{r})|^2. \quad (2.11)$$

This process is repeated until the electron density has converged, as depicted in Figure 2.2.

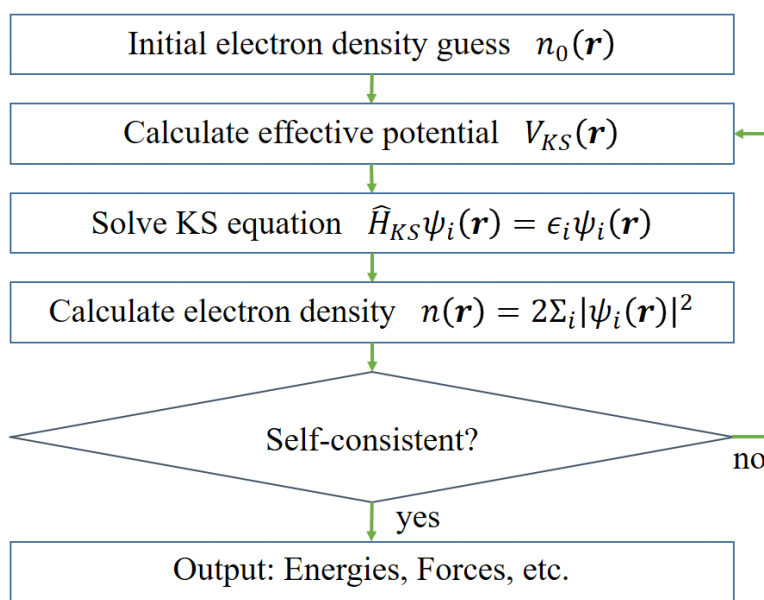


Figure 2.2 Schematic of the density functional theory process.

Kohn-Sham density functional theory is robust and can be applied to many problems such as determining molecular structure, adsorbate binding energies, and

vibrational frequencies. However, there are some limitations including modeling excited states, weakly bound adsorbates, and strongly correlated materials.

Van der Waals Corrections

One limitation of density functional theory is in the modeling of weakly bound adsorbates where van der Waals interactions are important. The exchange-correlation term in the Hamiltonian fails to account for non-local correlation effects, which become important for weakly bound adsorbates. Corrections to account for the long-range dispersion interactions can be added into the exchange-correlation term via empirical or theoretical methods.

There are many ways to incorporate van der Waals interactions including with non-local functionals, such as those by Langreth and Lundqvist [17, 18] that depend only on the distance between the two particles, however these models can have large errors. Van der Waals interactions can also be incorporated with interatomic dispersion corrections that depend on the inter-molecular separation and a material-dependent C_6 coefficient, such as the methods of Grimme [19-21], Tkatchenko and Scheffler [22], or Becke and Johnson [23, 24]. The C_6 coefficient is empirically derived in the method of Grimme and the method of Tkatchenko and Scheffler, but is completely non-empirical in the method of Becke and Johnson. The Grimme method is the most commonly used approach in catalysis calculations and although it is an empirical method, it gives accurate results and is extremely efficient.

Vienna Ab-initio Simulation Package

Vienna Ab-initio Simulation Package (VASP) is a computer program developed by Georg Kresse and coworkers [25-28] that can solve the Kohn-Sham equations within density functional theory. VASP is used herein because of its wide use in the field and because it uses a plane wave basis set. The plane wave basis set ensures periodicity of the simulation cell and allows for the modeling of surfaces with periodic boundary conditions such that an infinite slab may be created.

With a plane wave basis set, the pseudopotentials only represent the valence electron, and the core electrons need to be represented in a different way. The

interactions of the core electrons with the nuclei can be described using norm-conserving or ultrasoft pseudopotentials [29], or the projector augmented wave method [30, 31].

Nudged Elastic Band

Nudged elastic band is a technique pioneered by Hannes Jónsson and coworkers [32] to find the minimum energy path for a rearrangement of atoms from one stable configuration to another. The maximum potential energy in the minimum energy path is the transition state energy, or the potential energy barrier for the atomic rearrangement. The nudged elastic band method can be used for atomic and molecular diffusion processes, for changes in conformations of molecules, or to find the lowest energy path and energy barrier height for elementary steps in a chemical reaction.

The nudged elastic band method makes use of two boundary conditions, given by the initial and final configurations, and the force, which is calculated from the first derivative of the potential energy. Nudged elastic band is a chain-of-states method in which a sequence of images, or a chain of states, is generated between the initial and final states and the intermediate images are relaxed simultaneously. Between each image is a spring force that controls how far apart the middle images can move away from or toward each other in the direction parallel to the band. The force on each image is also calculated to find the real forces that act perpendicular to the band. The middle images move according to both the spring force and the force resulting from the potential energy surface. The middle images continue to move to find the minimum energy path until the force perpendicular to each image is below a certain threshold and all the images lie on the minimum energy path.

In addition, the climbing image nudged elastic band [33] may be invoked, which is used to place an image at the transition state, for instance to determine the transition state configuration. In the climbing image nudged elastic band, the image with the highest energy is pulled uphill to find the transition state and does not feel the force of the other springs in the band.

Vibrational Frequency Analysis

Vibrational frequency analysis is used to determine the vibrational frequencies of a chemical species, which are needed to determine the entropy, zero point energy, and kinetic prefactor of the species as well as to find a true minimum energy state or a transition state. The bonds within a chemical species may be represented as springs in which the atoms oscillate about their equilibrium positions with some characteristic frequency. The vibrational frequencies can be expressed as normal modes, in which “mode” refers to the simple harmonic motion which is sinusoidal in nature and “normal” means that the modes are orthogonal, or independent of each another.

The vibrational frequencies are calculated by sequentially displacing each atom in the x-, y-, and z-directions, determining the energy using density functional theory, calculating each force from the second derivative of the energy multiplied by the displacement, and then diagonalizing the Hessian matrix to find the eigenvalues. The Hessian matrix is a square matrix of second-order partial derivatives and is used to determine the curvature of the potential energy surface. The force on each atom and in each direction is calculated by matrix multiplication of the Hessian matrix with a vector of the displacements, given as

$$\begin{bmatrix} \frac{\partial^2 E}{\partial x_1 \partial x_1} & \frac{\partial^2 E}{\partial x_1 \partial x_2} & \dots & \frac{\partial^2 E}{\partial x_1 \partial x_{3N}} \\ \frac{\partial^2 E}{\partial x_2 \partial x_1} & \frac{\partial^2 E}{\partial x_2 \partial x_2} & \dots & \frac{\partial^2 E}{\partial x_2 \partial x_{3N}} \\ \vdots & \vdots & \ddots & \vdots \\ \frac{\partial^2 E}{\partial x_{3N} \partial x_1} & \frac{\partial^2 E}{\partial x_{3N} \partial x_2} & \dots & \frac{\partial^2 E}{\partial x_{3N} \partial x_{3N}} \end{bmatrix} \begin{bmatrix} \Delta x_1 \\ \Delta x_2 \\ \vdots \\ \Delta x_{3N} \end{bmatrix} = \begin{bmatrix} F_1 \\ F_2 \\ \vdots \\ F_{3N} \end{bmatrix}, \quad (2.12a)$$

or more compactly as

$$\mathbf{H} \cdot \mathbf{x} = \mathbf{F}, \quad (2.12b)$$

where \mathbf{H} is the Hessian matrix, \mathbf{x} is the displacement vector, and \mathbf{F} is the force vector. The size of the Hessian matrix is $3N \times 3N$ and the length of the displacement and force vectors is $3N$, where N is the number of vibrating atoms and $3N$ corresponds to the number of degrees of freedom.

Normal modes have their forces in line with the displacement, meaning that the force vector can be replaced with a scaling constant times the displacement vector, giving

$$\mathbf{H} \cdot \mathbf{x} = \lambda \mathbf{x} , \quad (2.13)$$

where λ is the scaling constant. Rearrangement gives

$$(\mathbf{H} - \lambda \mathbf{I}) \cdot \mathbf{x} = 0 , \quad (2.14)$$

where \mathbf{I} is the identity matrix. The determinant of the matrix $(\mathbf{H} - \lambda \mathbf{I})$ is equal to zero,

$$\det(\mathbf{H} - \lambda \mathbf{I}) = 0 , \quad (2.15)$$

and the values of λ , which are the eigenvalues, can be solved. The eigenvalues are the vibrational frequencies.

If an eigenvalue is negative, this corresponds to an imaginary frequency. A structure with n imaginary frequencies means that it is an n th order saddle point and there are n linearly independent directions in which the energy may be reduced. With zero imaginary frequencies, there are zero directions in which the energy may be reduced, thus the structure is in its true minimum energy state. Having one imaginary frequency means that there is one linearly independent direction in which the energy may be reduced and corresponds to the structure at a transition state.

When determining the vibrational frequencies of an adsorbate using density functional theory, all surface atoms are typically frozen so that they cannot vibrate and only the adsorbate atoms are displaced. This returns the vibrational frequencies of the adsorbate. Experimental alternatives for finding vibrational frequencies include infrared spectroscopy, Raman spectroscopy, sum frequency generation spectroscopy, and high resolution electron energy loss spectroscopy.

Density of States Analysis

Density of states analysis is used to determine the number of electronic states at a given energy level that electrons in a system are allowed to occupy. Density of states is used to gain insight into electronic structure properties of materials such as band gaps of semiconductors, the relative position of the highest occupied molecular orbital and lowest unoccupied molecular orbital of an adsorbate on a surface, or d-band centers of transition metals.

Calculating the band gap of an inorganic material is important for understanding its conductivity. The valence band in a density of states plot corresponds to the filled electronic states while the conduction band corresponds to the empty, excited electronic states. A large band gap between the valence and conduction bands indicates that the material is an insulator, a small band gap indicates a semiconductor, and no band gap indicates a conductor.

Molecular orbital theory states that molecular orbitals are formed by combining the atomic orbitals of the atoms in the molecule. The electrons from each atom fill the molecular orbitals and the two most important orbitals or states for molecular reactivity are the highest occupied molecular orbital (HOMO) and the lowest unoccupied molecular orbital (LUMO). The energies of all electronic states can be calculated from a density of states analysis and the energies of the HOMO and LUMO determined. The difference between the HOMO of one molecule and the LUMO of another can be used to predict the strength of the interaction, where a smaller energy difference indicates a stronger interaction. The HOMO-LUMO gap within a molecule represents the wavelength of light the compound can absorb or emit and is used to predict the color of the compound.

The d-band of a transition metal slab represents the number of electronic states that can be occupied by d-electrons at each energy level. The energy of the d-band center relates to the filling of the d-orbitals and is useful for understanding trends in adsorbate binding across different transition metal surfaces. According to Hammer and Nørskov's d-band model [34-36], the adsorption energy of an adsorbate scales with the d-band center of the surface. In general, a higher d-band center indicates a stronger bond between the adsorbate and the surface. This relationship has

been used to predict trends in catalysis and is an important tool in tuning catalyst properties for catalyst design and discovery of new catalyst [37-42].

Bader Charge Analysis

Bader charge analysis [43-46] is used to calculate the electronic charge on an atom, and is useful for examining charge transfer reactions or determining oxidation states. The charge on each atom is determined by examining the electronic charge density in the system. The electronic charge density centers about each nucleus, due to the core electrons in an atom. Moving out from the center of atom, the electronic charge density decreases until it nears another atom and the charge density starts to increase again, such that there is always an electronic charge minimum in the middle of two atoms. The electronic charge minima between atoms are convenient places to define the border of the atoms. Along the electronic charge minima, the atoms may be separated from each other so that each atom is enclosed in a Bader volume. The sum of the electronic charge within the Bader volume is the electronic charge corresponding to that atom.

References

- [1] M.C. Payne, M.P. Teter, D.C. Allan, T.A. Arias, J.D. Joannopoulos, Iterative Minimization Techniques for Ab Initio Total-Energy Calculations: Molecular Dynamics and Conjugate Gradients, *Reviews of Modern Physics*, 64 (1992) 1045-1097.
- [2] R. Car, Introduction to Density-Functional Theory and Ab-Initio Molecular Dynamics, *Quantitative Structure-Activity Relationships*, 21 (2002) 97-104.
- [3] P. Geerlings, F. De Proft, W. Langenaeker, Conceptual Density Functional Theory, *Chemical Reviews*, 103 (2003) 1793-1873.
- [4] J.P. Perdew, A. Ruzsinszky, J.M. Tao, V.N. Staroverov, G.E. Scuseria, G.I. Csonka, Prescription for the Design and Selection of Density Functional Approximations: More Constraint Satisfaction with Fewer Fits, *Journal of Chemical Physics*, 123 (2005).
- [5] J. Hafner, Ab-Initio Simulations of Materials using VASP: Density-Functional Theory and Beyond, *Journal of Computational Chemistry*, 29 (2008) 2044-2078.
- [6] J.P. Perdew, A. Ruzsinszky, Fourteen Easy Lessons in Density Functional Theory, *International Journal of Quantum Chemistry*, 110 (2010) 2801-2807.

- [7] A.D. Becke, Perspective: Fifty Years of Density-Functional Theory in Chemical Physics, *Journal of Chemical Physics*, 140 (2014).
- [8] M. Born, R. Oppenheimer, Zur Quantentheorie der Molekeln, *Annalen der Physik*, 389 (1927) 457-484.
- [9] P. Hohenberg, W. Kohn, Inhomogeneous Electron Gas, *Physical Review*, 136 (1964) B864-B871.
- [10] W. Kohn, L.J. Sham, Self-Consistent Equations Including Exchange and Correlation Effects, *Physical Review*, 140 (1965) A1133-A1138.
- [11] M.T. Lusk, A.E. Mattsson, High-Performance Computing for Materials Design to Advance Energy Science, *MRS Bulletin*, 36 (2011) 169-177.
- [12] J.P. Perdew, J.A. Chevary, S.H. Vosko, K.A. Jackson, M.R. Pederson, D.J. Singh, C. Fiolhais, Atoms, Molecules, Solids, and Surfaces - Applications of the Generalized Gradient Approximation for Exchange and Correlation, *Physical Review B*, 46 (1992) 6671-6687.
- [13] J.P. Perdew, J.A. Chevary, S.H. Vosko, K.A. Jackson, M.R. Pederson, D.J. Singh, C. Fiolhais, Erratum: Atoms, molecules, solids, and surfaces: Applications of the generalized gradient approximation for exchange and correlation, *Physical Review B*, 48 (1993) 4978-4978.
- [14] J.P. Perdew, Y. Wang, Accurate and Simple Analytic Representation of the Electron-Gas Correlation Energy, *Physical Review B*, 45 (1992) 13244-13249.
- [15] J.P. Perdew, K. Burke, M. Ernzerhof, Generalized Gradient Approximation Made Simple, *Physical Review Letters*, 77 (1996) 3865-3868.
- [16] J.P. Perdew, K. Burke, M. Ernzerhof, Errata: Generalized Gradient Approximation Made Simple, *Physical Review Letters*, 78 (1997) 1396-1396.
- [17] M. Dion, H. Rydberg, E. Schroder, D.C. Langreth, B.I. Lundqvist, Van der Waals Density Functional for General Geometries, *Physical Review Letters*, 92 (2004).
- [18] K. Lee, E.D. Murray, L.Z. Kong, B.I. Lundqvist, D.C. Langreth, Higher-Accuracy van der Waals Density Functional, *Physical Review B*, 82 (2010).
- [19] S. Grimme, Accurate Description of van der Waals Complexes by Density Functional Theory Including Empirical Corrections, *Journal of Computational Chemistry*, 25 (2004) 1463-1473.
- [20] S. Grimme, Semiempirical GGA-Type Density Functional Constructed with a Long-Range Dispersion Correction, *Journal of Computational Chemistry*, 27 (2006) 1787-1799.
- [21] S. Grimme, J. Antony, S. Ehrlich, H. Krieg, A Consistent and Accurate Ab Initio Parametrization of Density Functional Dispersion Correction (DFT-D) for the 94 Elements H-Pu, *Journal of Chemical Physics*, 132 (2010).

- [22] A. Tkatchenko, M. Scheffler, Accurate Molecular Van Der Waals Interactions from Ground-State Electron Density and Free-Atom Reference Data, *Physical Review Letters*, 102 (2009).
- [23] A.D. Becke, E.R. Johnson, A Density-Functional Model of the Dispersion Interaction, *Journal of Chemical Physics*, 123 (2005).
- [24] A.D. Becke, E.R. Johnson, Exchange-Hole Dipole Moment and the Dispersion Interaction, *Journal of Chemical Physics*, 122 (2005).
- [25] G. Kresse, J. Hafner, Ab Initio Molecular Dynamics for Liquid Metals, *Physical Review B*, 47 (1993) 558-561.
- [26] G. Kresse, J. Hafner, Ab Initio Molecular-Dynamics Simulation of the Liquid-Metal-Amorphous-Semiconductor Transition in Germanium, *Physical Review B*, 49 (1994) 14251-14269.
- [27] G. Kresse, J. Furthmuller, Efficiency of Ab-Initio Total Energy Calculations for Metals and Semiconductors Using a Plane-Wave Basis Set, *Computational Materials Science*, 6 (1996) 15-50.
- [28] G. Kresse, J. Furthmuller, Efficient Iterative Schemes for Ab Initio Total-Energy Calculations Using a Plane-Wave Basis Set, *Physical Review B*, 54 (1996) 11169-11186.
- [29] G. Kresse, J. Hafner, Norm-Conserving and Ultrasoft Pseudopotentials for First-Row and Transition Elements, *Journal of Physics-Condensed Matter*, 6 (1994) 8245-8257.
- [30] P.E. Blöchl, Projector Augmented-Wave Method, *Physical Review B*, 50 (1994) 17953-17979.
- [31] G. Kresse, D. Joubert, From Ultrasoft Pseudopotentials to the Projector Augmented-Wave Method, *Physical Review B*, 59 (1999) 1758-1775.
- [32] H. Jónsson, G. Mills, K.W. Jacobsen, Nudged Elastic Band Method for Finding Minimum Energy Paths of Transitions, in: B.J. Berne, G. Ciccotti, D.F. Coker (Eds.) *Classical and Quantum Dynamics in Condensed Phase Simulations*, World Scientific 1998, pp. 385-404.
- [33] G. Henkelman, B.P. Uberuaga, H. Jónsson, A Climbing Image Nudged Elastic Band Method for Finding Saddle Points and Minimum Energy Paths, *Journal of Chemical Physics*, 113 (2000) 9901-9904.
- [34] B. Hammer, J.K. Nørskov, Why Gold is the Noblest of All the Metals, *Nature*, 376 (1995) 238-240.
- [35] B. Hammer, J.K. Nørskov, Electronic Factors Determining the Reactivity of Metal Surfaces, *Surface Science*, 343 (1995) 211-220.
- [36] B. Hammer, J.K. Nørskov, Theoretical Surface Science and Catalysis - Calculations and Concepts, in: B.C. Gates, H. Knozinger (Eds.) *Advances in Catalysis, Vol 45: Impact of Surface Science on Catalysis* 2000, pp. 71-129.

- [37] A.J. Logsdail, L.O. Paz-Borbon, C.A. Downing, DFT-Computed Trends in the Properties of Bimetallic Precious Metal Nanoparticles with Core@Shell Segregation, *Journal of Physical Chemistry C*, 122 (2018) 5721-5730.
- [38] Z.Y. Chen, Y. Song, J.Y. Cai, X.S. Zheng, D.D. Han, Y.S. Wu, Y.P. Zang, S.W. Niu, Y. Liu, J.F. Zhu, X.J. Liu, G.M. Wang, Tailoring the d-Band Centers Enables Co₄N Nanosheets To Be Highly Active for Hydrogen Evolution Catalysis, *Angewandte Chemie-International Edition*, 57 (2018) 5076-5080.
- [39] A.J. Medford, A. Vojvodic, J.S. Hummelshoj, J. Voss, F. Abild-Pedersen, F. Studt, T. Bligaard, A. Nilsson, J.K. Norskov, From the Sabatier Principle to a Predictive Theory of Transition-Metal Heterogeneous Catalysis, *Journal of Catalysis*, 328 (2015) 36-42.
- [40] J.B. Wu, H. Yang, Platinum-Based Oxygen Reduction Electrocatalysts, *Accounts of Chemical Research*, 46 (2013) 1848-1857.
- [41] Z.Y. Duan, G.F. Wang, A First Principles Study of Oxygen Reduction Reaction on a Pt(111) Surface Modified by a Subsurface Transition Metal M (M = Ni, Co, or Fe), *Physical Chemistry Chemical Physics*, 13 (2011) 20178-20187.
- [42] P.A. Sheth, M. Neurock, C.M. Smith, First-Principles Analysis of the Effects of Alloying Pd with Ag for the Catalytic Hydrogenation of Acetylene-Ethylene Mixtures, *Journal of Physical Chemistry B*, 109 (2005) 12449-12466.
- [43] G. Henkelman, A. Arnaldsson, H. Jónsson, A Fast and Robust Algorithm for Bader Decomposition of Charge Density, *Computational Materials Science*, 36 (2006) 354-360.
- [44] E. Sanville, S.D. Kenny, R. Smith, G. Henkelman, Improved Grid-Based Algorithm for Bader Charge Allocation, *Journal of Computational Chemistry*, 28 (2007) 899-908.
- [45] W. Tang, E. Sanville, G. Henkelman, A Grid-Based Bader Analysis Algorithm Without Lattice Bias, *Journal of Physics-Condensed Matter*, 21 (2009).
- [46] M. Yu, D.R. Trinkle, Accurate and Efficient Algorithm for Bader Charge Integration, *Journal of Chemical Physics*, 134 (2011).

CHAPTER 3

HINDERED TRANSLATOR AND HINDERED ROTOR MODEL FOR
ADSORBATES: PARTITION FUNCTIONS AND ENTROPIES

Lynza H. Sprowl¹, Charles T. Campbell², Líney Árnadóttir^{1,*}

¹ School of Chemical, Biological and Environmental Engineering
Oregon State University, Corvallis, OR 97331, USA

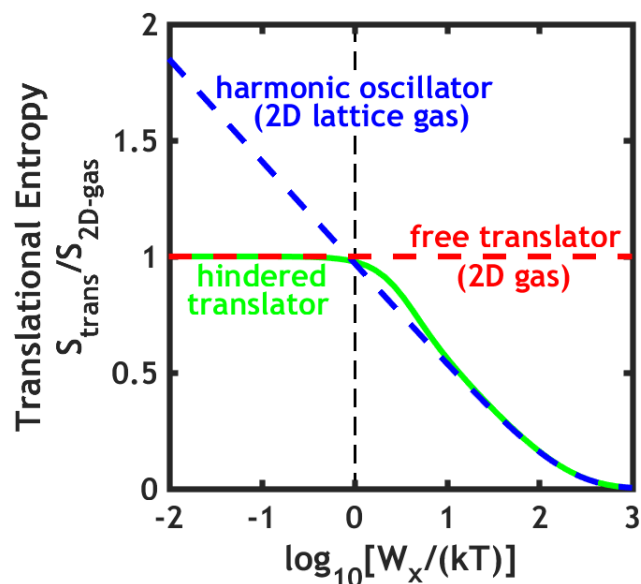
² Department of Chemistry, University of Washington, Seattle, WA 98195, USA

* Corresponding author

Reproduced in part from *J. Phys. Chem. C*, vol. 120, issue 18, pp. 9719-9731, 2016
with corrections from *J. Phys. Chem. C*, vol. 121, issue 17, pp. 9655-9655, 2017

© Copyright by the ASC, reproduced here with permission.
Further permissions related to the material excerpted should be directed to the ACS.

Abstract



With the recent explosion in computational catalysis and related microkinetic modeling, the need for a fast yet accurate way to predict equilibrium and rate constants for surface reactions has become more important. Here we present a fast and accurate new method to estimate the partition functions and entropies of adsorbates based on quantum mechanical estimates of the potential energy surface. As with previous approaches, it uses the harmonic oscillator (HO) approximation for most of the modes of motion of the adsorbate. However, it uses hindered translator and hindered rotor models for the three adsorbate modes associated with motions parallel to the surface, and evaluates these using an approach based on a method that has proven accurate in modeling the internal hindered rotations of gas molecules. The adsorbate entropies were calculated with this method for four adsorbates (methanol, propane, ethane, and methane) on Pt(111) using density functional theory (DFT) to evaluate the potential energy surface, and are shown to be in very good agreement with experiments, better than using only the HO approximation. The translational and rotational contributions to the entropy of a hindered translator / hindered rotor are very closely approximated by the corresponding harmonic oscillator entropy (within 0.46 R) when the barrier exceeds kT , and by the entropy of an ideal 2D monatomic

gas of the same mass and a free 1D rotor with the same moment of inertia, respectively, (within 0.12 R) when the barrier is less than kT . However, the harmonic oscillator / lattice gas model severely overestimates the entropy when kT exceeds the barrier.

Introduction

Adsorbed species on solid surfaces are involved in many reactions of great technological importance, especially in catalysis, electrocatalysis, separations, and fabrication of devices that require film growth (e.g., microelectronics and photovoltaics). As such, there has been tremendous effort worldwide to learn how to predict reaction rates and equilibrium constants for elementary reactions involving adsorbates. Theoretical calculations of rate constants and equilibrium constants for such reactions require knowing both the enthalpy and entropy of the adsorbed species and transition states. While much effort has been devoted to measuring and calculating the enthalpies of well-defined adsorbates [1, 2], few measurements of the entropies of adsorbates have been reported until Campbell and Sellers' 2012 paper [3] where they determined the entropies of a large number of adsorbed molecules. They combined those results with many previously measured entropies to show that the standard-state entropies of adsorbed molecules are generally $\sim 2/3$ of that for the same molecule in the gas phase at 1 bar and the same temperature [3]. They noted that these entropies are larger than most theoretical predictions, which assume a lattice-gas model and use the harmonic oscillator approximation to estimate partition functions [3]. They attributed this difference to a failure of that approximation, which we explore in detail here.

Here, we derive a new theoretical method to estimate partition functions and entropies of adsorbed species based on the hindered translator and hindered rotor potential energy surfaces for motions parallel to the surface. We use this method, together with potential energy surfaces estimated from density functional theory (DFT), to compute the entropies of some typical adsorbate systems. We show that this approach is more accurate than the harmonic-oscillator ideal lattice gas approximation yet still quite easy to implement. We show that the difference between

these models arises for several reasons but, surprisingly, not mainly due to a failure of the harmonic-oscillator approximation per se. Indeed, the new model (which gets the frequencies for vibrations parallel to the surface in a different way than the usual DFT calculations) gives a translational contribution to the hindered translator entropy that equals (within 0.46 R) the entropy of the 2D harmonic oscillator (i.e., ideal lattice gas) model when kT is less than the diffusion barrier and that equals (within 0.12 R) the translational entropy for an ideal 2D monatomic gas when kT exceeds that barrier (where the lattice gas approximation severely overestimates the entropy). The cutoff between these two behaviors is surprisingly sharp, so that adsorbates can be treated with one simple model or the other across the whole temperature range. A similar result is found for hindered rotations. This new model (and these very simple but accurate approximations to it) should be useful to future researchers in surface chemistry since it provides more accurate predictions of standard-state entropies and partition functions and thus more accurate equilibrium constants and rate constants for surface reactions than provided by the standard harmonic oscillator approximation.

Previously, surface chemists had usually thought of adsorbate entropies in terms of the two limiting cases that have been discussed in statistical thermodynamics texts: the 2D lattice gas model and the 2D ideal gas model [4]. In calculating rate constants for surface reactions based on quantum mechanical calculations of adsorbed reactant and transition state energies (mainly by density functional theory, DFT), surface chemists almost exclusively rely on harmonic transition state theory approaches, which assume that each adsorbate is a localized oscillator with only vibrational modes [5-10]. In analyzing experimental measurements of adsorbate entropies, it was postulated that this approach underestimates the experimental entropies because adsorbates have translations and rotations parallel to the surface which are more labile. The new method presented here accurately considers the nature of the potential energy surface for these motions, which have small but significant barriers to motion parallel to the surface, with translational barriers repeating every lattice constant (or a simple constant times it), and rotational barrier periodicity determined by the surface symmetry, as shown for example in Figure 3.1.

In principle, one must solve the Schrödinger equation for this potential's quantum-mechanically allowed energy levels and then sum over these states to get the partition function, q .

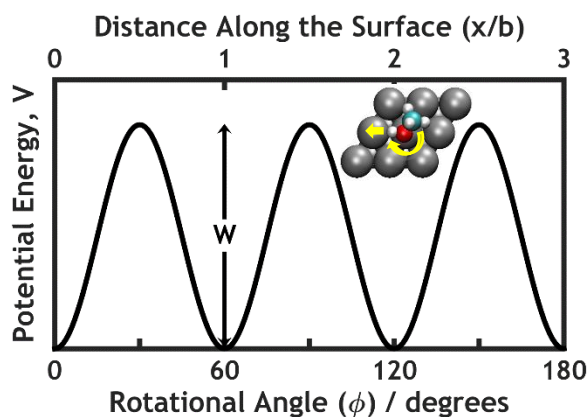


Figure 3.1 Example potential energy surface for adsorbate motions parallel to the surface. Translation (top axis), where b is the nearest-neighbor distance between surface atoms, and rotation (bottom axis) for a surface with 3-fold symmetry.

To simplify this, we utilized an approximation similar to that originally developed by Pitzer and Gwinn [11] for estimating partition functions of hindered internal rotations within gas molecules and later improved by Goddard's group and proven to give high accuracy [12]. To our knowledge, neither of these approximations have been applied to hindered rotations of adsorbates parallel to surfaces, and we do that here for the first time. The method of Pitzer and Gwinn [11] was also extended to hindered translations by Hill [4]. Here we improve that approximation for hindered translations in a way analogous to how Goddard's group [12] improved the approximation of Pitzer and Gwinn [11] for hindered rotations. We apply both these improved approximations to motions of adsorbates parallel to surfaces to estimate adsorbate entropies.

To implement these approximations for specific cases, to test their general accuracy, and to assess qualitative trends in their results, we utilize DFT with periodic boundary conditions and the climbing image nudged elastic band method (CI-NEB) [13-15] to estimate rotational and translational barrier heights and their periodicities. The standard-state molar entropies for adsorbed methane, ethane, propane, and

methanol on Pt(111) are estimated in this way and found to agree very well with experimental values (1.0, 1.3, 0.5, and 1.7 R, respectively, less than the experimental values, which average 14 R). Other model systems with a wider range of physical properties (i.e., mass, lattice constant, moment of inertia, rotation barrier periodicity) are also studied, to study how they affect entropies of adsorbates. The results show that the 2D ideal lattice gas / harmonic oscillator model accurately predicts standard-state adsorbate entropies calculated with this improved model (within 0.23 R in every mode) when kT is less than the barriers to diffusion and rotation parallel to the surface and that the 2D ideal gas model accurately predicts these (to within 0.06 R per mode) when kT exceeds that barrier, provided that the vibrational frequencies for these modes are determined by fitting these barriers to a sine wave potential energy (as opposed to the usual DFT normal-mode analysis of the adsorbate's minimum-energy structure). However, the harmonic oscillator / lattice gas model severely overestimates the entropy when kT exceeds the barrier.

We discuss here only “ideal” adsorbates that have no adsorbate-adsorbate lateral interactions. It is well-known that such interactions can have huge effects on reaction energies and activation energies. These enthalpic effects often cause much bigger changes in equilibrium constants and rate constants than the entropic effects we discuss here, and so they cannot be neglected. Statistical mechanical treatments that include adsorbate-adsorbate interactions have been discussed in the literature, usually within the lattice gas / harmonic oscillator approximation [16-20]. Excluded volume is highly important and is naturally included in ideal 2D lattice gas models [21] and has been included in ideal 2D gas models as well [22].

Theory

Ideal 2D Hindered Translator: Partition Function

The hindered translator method, adapted from Hill [4], is used to calculate the partition function for a 2D hindered translator, q_{xy} . The adsorbates are considered to be ideal in that any adsorbate-adsorbate interactions are neglected. The partition function for z-motion, q_z , is assumed to be a harmonic oscillator (HO), contributing a factor q_z to the partition function given by the standard expression for a single HO

vibrational mode of frequency ν_z [4]. This formulation is derived for dilute systems in which $N < M$ where N is the number of adsorbed species and M is the number of surface sites. Hill's approach is summarized below, but the notation has been changed to be consistent with Goddard's [12] hindered rotor notation.

In Hill's treatment the potential energy function for the hindered xy -motion is written as

$$V(x, y) = V_0 + \frac{W_x}{2} \left(1 - \cos \frac{2\pi x}{b}\right) + \frac{W_y}{2} \left(1 - \cos \frac{2\pi y}{b}\right), \quad (3.1)$$

where V_0 is the potential energy at the minima, W_x and W_y are the translational energy barrier heights, and b is the nearest-neighbor distance between surface atoms, assumed to be the same in both directions. For simplicity, the barrier is also assumed to be the same in both x and y directions, so $W_x = W_y$ here, though these assumptions are easy to change in the end result. At low temperatures, the adsorbate experiences localized adsorption and vibrates about the minima with a frequency (where the force constant is obtained from the second derivative of the potential versus distance at the minimum) equal to

$$\nu_x = \nu_y = \left(\frac{W_x}{2mb^2}\right)^{1/2}, \quad (3.2)$$

where m is its mass. At high temperatures, the adsorbate instead experiences free translation. At intermediate temperatures there is a transition from one extreme kind of adsorption to the other. During this transition, the xy -partition function can be written as

$$q_{xy} = q_{classical} \cdot \frac{q_{HO}}{q_{HO-classical}}, \quad (3.3)$$

in which $q_{classical}$ is the classical partition function, q_{HO} is the quantum harmonic oscillator partition function, and $q_{HO-classical}$ is the classical harmonic oscillator partition function. The classical partition function is

$$q_{classical} = M(\pi r_x T_x) \exp\left[-\frac{r_x}{T_x}\right] I_0^2\left[\frac{r_x}{2T_x}\right], \quad (3.4)$$

where M is the number of surface sites, r_x is the ratio of the energy barrier height to the vibrational frequency times Planck's constant, $r_x = W_x/h\nu_x$, and the dimensionless temperature T_x is $T_x = kT/h\nu_x$. I_0 is the zero-order modified Bessel function of the first kind. The quantum partition function for a single harmonic oscillator oscillating independently in two identical directions is

$$q_{HO} = \left(\frac{\exp\left[-\frac{1}{2T_x}\right]}{1 - \exp\left[-\frac{1}{T_x}\right]} \right)^2, \quad (3.5)$$

which at high temperature gives the classical limit

$$q_{HO-classical} = T_x^2. \quad (3.6)$$

Substitution of Equations 3.4-3.6 into Equation 3.3 gives the same final result as Hill [4]

$$q_{xy} = \frac{M\left(\frac{\pi r_x}{T_x}\right) \exp\left[-\frac{r_x}{T_x}\right] \exp\left[-\frac{1}{T_x}\right] I_0^2\left[\frac{r_x}{2T_x}\right]}{\left(1 - \exp\left[-\frac{1}{T_x}\right]\right)^2}. \quad (3.7)$$

The M here could be replaced by $M = \mathcal{A}/b^2$ (area/(nearest neighbor distance)²) for a surface with 4-fold symmetry (like FCC(100) faces) or by $M = \mathcal{A}/\left(\frac{\sqrt{3}}{2}b^2\right)$ for a surface with 3-fold symmetry (like FCC(111)), thus showing that q_{xy} is proportional to surface area, \mathcal{A} , just as for an ideal 2D gas.

This partition function is accurate at higher temperatures but gives an incorrect zero-point energy contribution at lower temperatures, as pointed out by McClurg, Flagan and Goddard [12] for the nearly identical expression for hindered rotors. In the similar treatment of hindered rotors by McClurg et al. [12] (see above), they adopted the Padé approximant for ΔE^{zp} to account for the over-estimation of the

zero-point energy in the harmonic oscillator function. Using a similar approach for the translator here gives

$$q_{trans} = q_{xy} \exp \left[2 \frac{\Delta E^{zp}}{kT} \right], \quad (3.8)$$

where

$$\Delta E^{zp} = \frac{h\nu_x}{2+16r_x}. \quad (3.9)$$

The factor of two in Equation 3.8 comes from the two degrees of freedom, x and y , which we assume here to have identical potential energy versus distance. Substituting for T_x , this simplifies to

$$q_{trans} = q_{xy} \exp \left[\frac{2}{(2+16r_x)T_x} \right] = \frac{M \left(\frac{\pi r_x}{T_x} \right) \exp \left[-\frac{r_x}{T_x} \right] \exp \left[-\frac{1}{T_x} \right] \left| \frac{r_x}{2T_x} \right|^2 \exp \left[\frac{2}{(2+16r_x)T_x} \right]}{\left(1 - \exp \left[-\frac{1}{T_x} \right] \right)^2} \exp \left[\frac{2}{(2+16r_x)T_x} \right]. \quad (3.10)$$

Defining an interpolation function f_{trans} as the ratio of the translational partition function to its (quantum) harmonic oscillator partition function, analogous to the hindered rotor interpolation function of McClurg et al. for internal rotations in molecules [12], gives

$$f_{trans} = \frac{q_{trans}/M}{q_{HO}}. \quad (3.11)$$

Here, q_{trans} is divided by M in this definition of f_{trans} since q_{trans} refers to the whole surface with M sites whereas q_{HO} is defined here for a single harmonic oscillator site. This interpolation function can be seen by dividing Equations 3.10 and 3.5 above to equal

$$f_{trans} = P_{trans} \exp \left[\frac{2}{(2+16r_x)T_x} \right], \quad (3.12)$$

where

$$P_{trans} = \frac{q_{xy}}{M q_{HO}} = \frac{\pi r_x}{T_x} \exp\left[-\frac{r_x}{T_x}\right] I_0^2\left[\frac{r_x}{2T_x}\right]. \quad (3.13)$$

Figure 3.2 shows a plot of f_{trans} and P_{trans} , which is the hindered translator partition function normalized by $M q_{HO}$ versus temperature for different r_x values, with and without this zero-point energy correction. This only makes much difference at low temperatures.

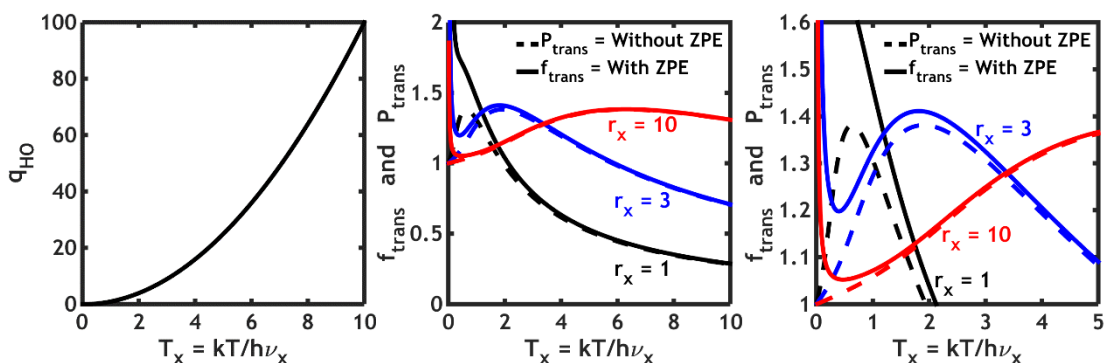


Figure 3.2 Quantum harmonic oscillator and hindered translator partition functions. Left: The quantum harmonic oscillator partition function for two identical HO modes, x and y , from Equation 3.5. Center: The hindered translator partition functions with and without the ZPE correction of Equation 3.8 normalized to $M q_{HO}$, i.e., $f_{trans} = q_{trans}/(M q_{HO})$ and $P_{trans} = q_{xy}/(M q_{HO})$, plotted versus temperature for three different r_x ($r_x = 1, 3, 10$). Right: An expanded plot of the lower temperature range. The ZPE correction factor only affects the values at low temperatures.

Hindered Rotor: Partition Function

Here we consider only the hindered rotation of the whole adsorbate about an axis perpendicular to the surface. (On a rough or faceted surface, this could be the *local* surface normal.) The treatment of a hindered rotation is adopted from McClurg et al. [12] where the potential energy function for hindered rotation is

$$V(\phi) = \frac{W_r}{2} (1 - \cos n\phi), \quad (3.14)$$

where W_r is the energy barrier height for rotation and n is the number of equivalent minima in a full rotation. At low temperatures the harmonic oscillator frequency is

$$\nu_r = \frac{\omega}{2\pi} = \frac{1}{2\pi} \left(\frac{n^2 W_r}{2I} \right)^{1/2}, \quad (3.15)$$

where I is the reduced moment of inertia given by

$$I = \sum_i m_i d_i^2, \quad (3.16)$$

where m_i is the mass of each adsorbate atom and d_i is the distance in the xy plane from the center of each adsorbate atom to the axis about which the adsorbate is being rotated. Unlike in gas-phase rotation, this axis of rotation may not necessarily pass through the center of mass of the adsorbate, since it might, for example, be attached most strongly to the surface through a bond nearer to one end of the adsorbate, and rotate about that bond. Similarly to the hindered translator, the ratio of the energy barrier height to the harmonic oscillator frequency times Planck's constant, r_r , is defined as $r_r = W_r/h\nu_r$ and the dimensionless temperature, T_r , is $T_r = kT/h\nu_r$.

The quantum harmonic oscillator partition function in this case is

$$q_{HO} = \frac{\exp\left[-\frac{1}{2T_r}\right]}{1 - \exp\left[-\frac{1}{T_r}\right]}, \quad (3.17)$$

which is identical in form to Equation 3.5 above for translators, except that Equation 3.5 is for two such modes, so it is squared there. Defining an interpolation function f_{rot} following McClurg et al. [12], just as for hindered translations above, gives

$$f_{rot} = \frac{q_{rot}}{q_{HO}}, \quad (3.18)$$

where McClurg et al. [12] showed that

$$f_{rot} = P_{rot} \exp \left[\frac{\Delta E^{zp}}{kT} \right] = P_{rot} \exp \left[\frac{1}{(2+16r_r)T_r} \right], \quad (3.19)$$

wherein they adopted the Padé approximant for ΔE^{zp} to account for the over-estimation of the zero-point energy in the harmonic oscillator function. P_{rot} is the earlier approximation of q_{rot}/q_{HO} introduced by Pitzer and Gwinn [11] that did not include this correction and is given by [12]

$$P_{rot} = \left(\frac{\pi r_r}{T_r} \right)^{1/2} \exp \left[-\frac{r_r}{2T_r} \right] I_0 \left[\frac{r_r}{2T_r} \right]. \quad (3.20)$$

The full rotational partition function is then

$$q_{rot} = f_{rot} \times q_{HO} = \frac{\left(\frac{\pi r_r}{T_r} \right)^{1/2} \exp \left[-\frac{r_r}{2T_r} \right] \exp \left[-\frac{1}{2T_r} \right] I_0 \left[\frac{r_r}{2T_r} \right]}{\left(1 - \exp \left[-\frac{1}{T_r} \right] \right)} \exp \left[\frac{1}{(2+16r_r)T_r} \right]. \quad (3.21)$$

This now looks very similar to the expression for the partition function for hindered translation, with $q_{rot}^2 = q_{trans}/M$, except for the subtle differences in the definitions of their parameters r_i and T_i . As seen by comparing Equations 3.19 and 3.20 with Equations 3.12 and 3.13, f_{trans} is just f_{rot}^2 , which is squared because there are two translational modes but only a single rotational mode.

We have assumed above that the rotor is *asymmetric*. For *symmetric* rotors, the expressions above for q_{rot} must be divided by the symmetry number (e.g., 2 for a linear alkane rotating about its center of mass) [23].

Thermodynamic Functions

We assume here that the densities of states for the solid's modes are not changed upon adsorption. The total partition function for the adsorbate is given by

$$q_{ad} = q_{trans} \cdot q_{rot} \cdot q_z \cdot q_{int-vib}, \quad (3.22)$$

where $q_{int-vib}$ is the partition function for all the internal vibrations of the adsorbate, including the vibration(s) of the whole adsorbate about the two rotational axes parallel to the surface (i.e., cartwheel-like rotations that become vibrations upon adsorption). (Linear adsorbates lying flat on the surface have only one such axis.) The number of such internal vibrational modes is three times the number of atoms in the molecule minus four (since there are two hindered translations, one hindered rotation parallel to the surface (i.e., helicopter-like rotation), and one vibration of the whole adsorbate perpendicular to the surface). Since the adsorbates are identical, non-interacting, and indistinguishable, they follow Boltzmann statistics. Therefore, the Helmholtz free energy A is given as

$$A = -NkT \ln \left[\frac{q_{ad} e}{N} \right] = -NkT \ln \left[\frac{(q_{ad}/\mathcal{A})e}{(N/\mathcal{A})} \right] = -NkT \ln \left[\frac{(q_{ad}/M)e}{(N/\mathcal{A})b^2} \right]. \quad (3.23)$$

Expanding q_{ad} above and separating terms gives that

$$A = A_{trans} + A_{rot} + A_z + A_{int-vib}, \quad (3.24)$$

where each contribution A_i for q_{rot} , q_z , and $q_{int-vib}$ is given by

$$A_i = -NkT \ln q_i, \quad (3.25)$$

except A_{trans} , which is instead

$$A_{trans} = -NkT \ln \left[\frac{(q_{trans}/\mathcal{A})e}{(N/\mathcal{A})} \right] = -NkT \ln \left[\frac{(q_{trans}/M)e}{(N/\mathcal{A})b^2} \right]. \quad (3.26)$$

In Equations 3.23 and 3.26 we assumed $\mathcal{A} = Mb^2$, which is only valid for a surface with 4-fold symmetry (like FCC(100) faces). For a surface with 3-fold symmetry (like FCC(111)), one must replace this with $\mathcal{A} = M \left(\frac{\sqrt{3}}{2} b^2 \right)$ instead. The same applies in Equations 3.29 and 3.38 below. This also applies to b^2 in Equation 3.2 for

the frequency, where now $\nu_x = \left(\frac{W_x}{2m(\sqrt{3}/2*b^2)}\right)^{1/2}$. This form is used in our calculations for Pt(111) described below. An equation similar to Equation 3.24 was presented by Kreuzer [17] but without the hindered translator / hindered rotor corrections discussed below.

If we set the zero-energy reference as the zero-point vibrational energy of the adsorbate, every vibrational mode of frequency ν_i contributes an amount to A of [23]

$$A_{HO,i} = NkT \left(\ln \left[1 - \exp \left[-\frac{h\nu_i}{kT} \right] \right] \right) = NkT \left(\ln \left[1 - \exp \left[-\frac{1}{T_i} \right] \right] \right), \quad (3.27)$$

where we define the dimensionless temperature, T_i , as $T_i = kT/h\nu_i$ (not to be confused with the so-called vibrational temperature, $h\nu_i/k$). Every hindered translational or hindered rotational mode i contributes this same amount plus an additional amount equal to [12]

$$\Delta A_i = -NkT \ln f_i = NkT \left(\frac{-1}{(2+16r_i)T_i} + \frac{r_i}{2T_i} - \ln \left[\left(\frac{\pi r_i}{T_i} \right)^{1/2} I_0 \left[\frac{r_i}{2T_i} \right] \right] \right). \quad (3.28)$$

Note that the 2D hindered translator must include two such contributions, for x and y motion, which are equal to each other since we assumed that W and b are identical in the x and y directions, such that $f_{trans} = f_x f_y = f_x^2$.

In addition, these two hindered translator modes, when grouped together, contribute an additional amount to A_{trans} and A equal to

$$A_1 = -NkT(1 - \ln[b^2(N/\mathcal{A})]) = NkT(\ln \theta - 1). \quad (3.29)$$

This arises from the factor $e/((N/\mathcal{A})b^2) = e/\theta$ in Equations 3.23 and 3.26, where $\theta = (N/\mathcal{A})/(M/\mathcal{A})$ is the fractional coverage. For standard-state free energy, one must use the standard-state surface concentration for N/\mathcal{A} here. (As discussed above, this equation is valid for a surface with 4-fold symmetry. For surfaces with 3-

fold or 6-fold symmetry, replace b^2 with $\frac{\sqrt{3}}{2}b^2$.) As shown elsewhere [21], A_1 has essentially the same quantitative value versus θ as the contribution of the configurational degeneracy (configurational entropy) to the free energy of an ideal 2D *lattice* gas except at high θ (>0.05), but it arises from fundamentally different reasons.

For standard-state thermodynamic values, we simply use the standard state concentration, $(N/\mathcal{A})^0$ for (N/\mathcal{A}) here. We have shown previously that the standard value $(N/\mathcal{A})^0$ is most convenient when taken as [21]

$$\left(\frac{N}{\mathcal{A}}\right)^0 = e^{1/3} \left(\frac{N_A}{V_{\text{gas}}^0}\right)^{2/3} = 1.40 \left(\frac{N_A}{V_{\text{gas}}^0}\right)^{2/3}, \quad (3.30)$$

where (N_A/V^0) is the standard-state concentration of the 3D ideal gas, which is defined as its concentration at the standard pressure of 1 bar and T . This is given by the ideal gas law as 1 bar/(kT), which at 298 K is one mole per 24.8 L. This sets the standard-state surface concentration as $1.17 \times 10^{13} \text{ cm}^{-2}$ at 298 K.

Substituting the ideal gas law expressions for $\left(\frac{N_A}{V_{\text{gas}}^0}\right) = \left(\frac{N_A \text{ 1 bar}}{RT}\right)$ gives

$$\left(\frac{N}{\mathcal{A}}\right)^0 = 1.40 \left(\frac{N_A \text{ 1 bar}}{RT}\right)^{2/3}. \quad (3.31)$$

We proved [21] that choosing this standard concentration is equivalent to choosing a standard state such that the translational contribution to the standard molar entropy is 2/3 of that for the 3D ideal gas. This is a convenient and intuitive choice since it has 2/3 the number of translational degrees of freedom. We also proved [21] that, to similarly ensure that the translational contribution to the standard molar entropy of an adsorbate treated as an ideal 1D gas is 1/3 of that for the 3D ideal gas, its standard-state concentration must be $e^{2/3}$ times the 1/3 power of the standard-state concentration of a 3D ideal gas. These choices have an intuitive advantage when estimating standard reaction entropies and activation entropies when calculating equilibrium constants and rate constants for surface reactions [21].

The internal energy E is given in Boltzmann statistics by [4, 23]

$$E = NkT^2 \left(\frac{d \ln q_{ad}}{dT} \right)_{\mathcal{A}}. \quad (3.32)$$

Similarly, every HO vibrational mode contributes an amount to E (relative to its zero-point energy as the zero reference energy) of [23]

$$E_{HO,i} = Nh\nu_i \left(\frac{1}{\exp[h\nu_i/kT]-1} \right) = NkT \left(\frac{1/T_i}{\exp[1/T_i]-1} \right). \quad (3.33)$$

Every hindered translational and hindered rotational mode contributes this plus an additional amount to the internal energy equal to

$$\Delta E_i = NkT^2 \left(\frac{d \ln f_i}{dT} \right)_{\mathcal{A}} = NkT \left(-\frac{1}{2} - \frac{1}{(2+16r_i)T_i} + \frac{r_i}{2T_i} \left(1 - \frac{I_1 \left[\frac{r_i}{2T_i} \right]}{I_0 \left[\frac{r_i}{2T_i} \right]} \right) \right). \quad (3.34)$$

This is identical to the result for the contribution of f_{rot} to E as given by McClurg, Flagan and Goddard [12], except they had a sign error on the term $(1 - I_1[r_i/2T_i]/I_0[r_i/2T_i])$. Again for the 2D hindered translator, there are two such contributions, equal to each other since we assume that W and b are identical in x and y here.

The entropy is then given by [4]

$$S = \frac{E-A}{T}. \quad (3.35)$$

Every vibrational mode of frequency ν_i thus contributes an amount to S equal to [23]

$$S_{HO,i} = Nk \left(\frac{h\nu_i/kT}{\exp[h\nu_i/kT]-1} - \ln \left[1 - \exp \left[-\frac{h\nu_i}{kT} \right] \right] \right) = Nk \left(\frac{1/T_i}{\exp[1/T_i]-1} - \ln \left[1 - \exp \left[-\frac{1}{T_i} \right] \right] \right). \quad (3.36)$$

Every hindered translational or hindered rotational mode i contributes this same amount plus an additional amount equal to [12]

$$\Delta S_i = \frac{\Delta E_i - \Delta A_i}{T} = Nk \left(-\frac{1}{2} - \frac{r_i}{2T_i} \frac{I_1 \left[\frac{r_i}{2T_i} \right]}{I_0 \left[\frac{r_i}{2T_i} \right]} + \ln \left[\left(\frac{\pi r_i}{T_i} \right)^{1/2} I_0 \left[\frac{r_i}{2T_i} \right] \right] \right). \quad (3.37)$$

Finally, the two translational modes taken together contribute an additional, concentration-related amount to the entropy (arising from A_l) equal to [21]

$$S_1 = -Nk(\ln[b^2(N/\mathcal{A})] - 1) = -Nk(\ln \theta - 1). \quad (3.28)$$

For standard-state entropies, one must use the standard-state surface concentration for N/\mathcal{A} here. (This equation is valid for a surface with 4-fold symmetry. For surfaces with 3-fold or 6-fold symmetry, replace b^2 with $\frac{\sqrt{3}}{2}b^2$.) As noted by [21], S_l has essentially the same value as the configurational entropy of an ideal 2D lattice gas except at high θ (>0.05), but it arises from fundamentally different reasons. When an adsorbate is treated as an ideal 2D gas, it has the same concentration-dependent contribution S_l as in Equation 3.38, and the remaining, concentration-independent part of its entropy is given by $S - S_1 = R \ln[(qe/\mathcal{A})/(M/\mathcal{A})]$, where M/\mathcal{A} is the saturation concentration used to define its relative coverage, $\theta = (N/\mathcal{A})/(M/\mathcal{A})$ [21]. For ideal 2D monatomic gases, this gives $S - S_1 = R \ln[(2\pi mkTe / h^2)/(M / \mathcal{A})]$.

We verified that these equations above give the same entropy as that for an ideal 2D gas for the case of a monatomic gas in the limit of extremely small diffusion barrier, W .

Computational Methods

The electronic structure calculations for each adsorbed species on Pt(111) and the energy barriers for their rotation and translation were calculated utilizing density functional theory (DFT) via the Vienna Ab-initio Simulation Package (VASP) [24-

27]. The projector augmented wave (PAW) method [28, 29] was used to represent the core electrons. The exchange correlation potential and energy were described by the generalized gradient approximation (GGA) as defined by the Perdew-Burke-Ernzerhof (PBE) functional [30, 31]. Calculations that included van der Waals (vdW) forces used the D3 method of Grimme [32].

The supercell was a 3x3x3 Pt(111) slab with 20 Å of vacuum space and periodic boundary conditions. Initially only the bottom layer of Pt was held fixed while the top two layers were allowed to relax, simulating a surface. Then all Pt atoms were held fixed and one molecule was allowed to adsorb on the Pt surface, giving a coverage of $\theta = 1/9$ monolayer. Relaxing the top two layers of the surface decreases the adsorption energy of methanol on the Pt slab by 5×10^{-3} eV with vdW and by 4×10^{-4} eV without vdW and increases the barrier heights for translations by 0.01 and 0.02 eV with and without vdW, respectively. The rotational barriers were not affected significantly by the relaxation of the surface, but these barriers were already very small. These are very small relative differences in the barrier heights (e.g., <5% for diffusion using vdW), so we neglected relaxation for the barrier height calculations reported here. The adsorbed molecules included methanol, methane, ethane, and propane. The two lowest-energy structures for adsorbed propane have different adsorbed configurations, one with its secondary (C_2) carbon atom closest to a Pt atom and another with its primary (C_1) carbon atoms closer to Pt atoms. The energy difference between the two adsorbed configurations of propane was only 0.02 eV with vdW and 0.01 eV without vdW, so both were included. The lowest energy adsorption site for all molecules calculated was with either a C or O atom sitting very near the atop site of a metal atom, such that there are six essentially equal barriers to rotation parallel to the surface (i.e., one every 60°).

The kinetic energy cutoff for the Kohn-Sham orbitals was 410 eV and 400 eV for calculations with and without vdW interactions, respectively. Increasing the cutoff energies to 500 eV only changes the adsorption energy of methanol by 6×10^{-4} eV with vdW and 1×10^{-3} eV without vdW. Plane-wave calculations were employed using the Monkhorst-Pack method [33] with 5x5x1 special k points. Increasing the number of k points to 7x7x1 changes the adsorption energy by 0.03 eV and 0.01 eV with and

without vdW, respectively. All simulations were relaxed until the forces were below 0.02 eV/\AA .

The minimum energy path (MEP) and transition states for translation and rotation of each adsorbate were calculated by the CI-NEB method [13, 14]. Seven images were calculated between all initial and final states. Translations were calculated as the translations from atop site to an adjacent atop site, and rotations were simulated as a 120° rotation around the z-axis through the adsorption site. Initial and saddle point configurations for all calculations with vdW are provided in the Supporting Information. In some cases, the minimum energy path for rotation has the adsorbate rotating about one Pt atom and not about the adsorbate's center of mass. For this reason, the distance term in the reduced moment of inertia, Equation 3.16, is calculated as the distance in the xy plane from each adsorbate atom to the center of the Pt atom about which the adsorbate rotates. The calculated lattice constants for Pt were 3.92 \AA and 3.97 \AA with and without including the vdW correction, respectively, compared to 3.92 \AA determined experimentally [34].

Vibrational frequencies were determined from the eigenvalues of the Hessian matrix for the minima energy configuration of each adsorbate on the surface. Two displacements were used for each direction and atom with a step size of 0.01 \AA for all atoms in the adsorbate, while the surface atoms were held fixed.

This new approach for calculating partition functions and entropies for adsorbates within the ideal hindered translator / hindered rotor model will be implemented into the thermochemistry module of ASE [35] as well as into CatMAP [36].

Results and Discussion

Comparison of Predicted Entropies of Small Adsorbates on Pt(111) to Experiments

To test the accuracy of the method, we model here several molecular adsorbates (methane, ethane, propane, and methanol) on the Pt(111) surface, systems for which the experimental standard-state entropy has been reported [3, 37]. All adsorbates studied adsorb on atop sites, so each adsorbate has six equivalent minima in a full rotation (i.e., $n = 6$). Translational energy barrier heights and rotational

energy barrier heights were determined by DFT calculations using the climbing image nudged elastic band (CI-NEB) method and are listed in Tables 3.1 and 3.2. These barrier heights were then used together with the site periodicities to fit the potential energy versus coordinate to cosine waves (i.e., Equations 3.1 or 3.14), from which we calculated the corresponding translational and rotational frequencies using Equations 3.2 and 3.15 and the ratios of the energy barrier height to the vibrational frequency, r_x and r_r . This approach has been used previously to better estimate the frequencies for hindered translations of adsorbates [5, 7]. For the systems studied here, these frequencies were generally lower than those that came directly from the normal-mode analysis, with an average ratio of 0.70 ± 0.41 for calculations with vdW corrections. These barriers and their ratios to $h\nu_i$ are also listed in Tables 3.1 and 3.2. The translational ratios $r_x = W_x/h\nu_x$ vary from $r_x = 2 - 28$, while the ratios for rotations range from $r_r = 0 - 10$. The ratios of W_x and W_r to the adsorption energy averaged 0.09 and 0.008, respectively, for DFT using vdW corrections, with standard deviations slightly larger than these averages.

Table 3.1 Summary of hindered translator data for several adsorbates on Pt(111). Translational energy barriers (W_x), adsorbate masses (m), vibrational frequencies (ν_x), the r_x ratios ($r_x = W_x/(h\nu_x)$), and adsorption energy (E_{ads}) are included.

Adsorbate	vdW included?	W_x (eV)	m (amu)	ν_x (s^{-1})	r_x	E_{ads} (eV)
Methanol	Yes	0.294	32	2.58×10^{12}	27.5	-0.728
Methanol	No	0.218	32	2.20×10^{12}	24.0	-0.306
Propane (C₂)	Yes	0.091	44	1.23×10^{12}	18.0	-0.656
Propane (C₂)	No	0.041	44	8.12×10^{11}	12.2	-0.062
Propane (C₁)	Yes	0.066	44	1.05×10^{12}	15.3	-0.637
Propane (C₁)	No	0.023	44	6.13×10^{11}	9.2	-0.054
Ethane	Yes	0.049	30	1.09×10^{12}	10.9	-0.458
Ethane	No	0.020	30	6.81×10^{11}	7.0	-0.045
Methane	Yes	0.006	16	5.36×10^{11}	2.9	-0.270
Methane	No	0.005	16	4.50×10^{11}	2.5	-0.037

Table 3.2 Summary of hindered rotor data for several adsorbates on Pt(111). Rotational energy barriers (W_r), adsorbate reduced moments of inertia (I), vibrational frequencies (ν_r), and the r_r ratios ($r_r = W_r / (h \nu_r)$) are included.

Adsorbate	vdW included?	W_r (eV)	I (amu*Å ²)	ν_r (s ⁻¹)	r_r
Methanol	Yes	0.002	22.3	6.94×10^{11}	0.85
Methanol	No	0.001	21.1	5.29×10^{11}	0.61
Propane (C₂)	Yes	0.011	104.1	6.86×10^{11}	3.9
Propane (C₂)	No	0.002	69.0	3.33×10^{11}	1.3
Propane (C₁)	Yes	0.046	165.9	1.10×10^{12}	10.0
Propane (C₁)	No	0.022	162.0	7.66×10^{11}	6.8
Ethane	Yes	0.018	73.4	1.03×10^{12}	4.2
Ethane	No	0.0006	37.8	2.63×10^{11}	0.55
Methane	Yes	0.0008	8.77	6.26×10^{11}	0.30
Methane	No	0.0001	3.35	3.99×10^{11}	0.07

The energy versus coordinate for all adsorbates' hindered translations and rotations is shown in Figure 3.3, with geometries at the initial state and transition state presented in the Supporting Information. Their corresponding contributions to the adsorbate's total standard molar entropy are shown versus temperature in Figure 3.4, along with the contributions from the $3n-3$ vibrations, which include all internal vibrations and the z -vibration of the whole adsorbate. We have assumed here that the three lowest vibrational frequencies which come directly out of the DFT normal-mode calculations correspond to the two hindered translations and the hindered rotation. We verified that this is qualitatively correct for the case of adsorbed methanol by visualizing its three lowest-frequency normal-mode motions (calculated including vdW), although it was also clear that these modes include some other minor contributing coordinates. Thus, the frequencies used for the frequencies for the remaining $3n-3$ vibrations were taken from the remainder of those calculated frequencies, and these lowest three frequencies were discarded (i.e., replaced with hindered translation and hindered rotation partition functions).

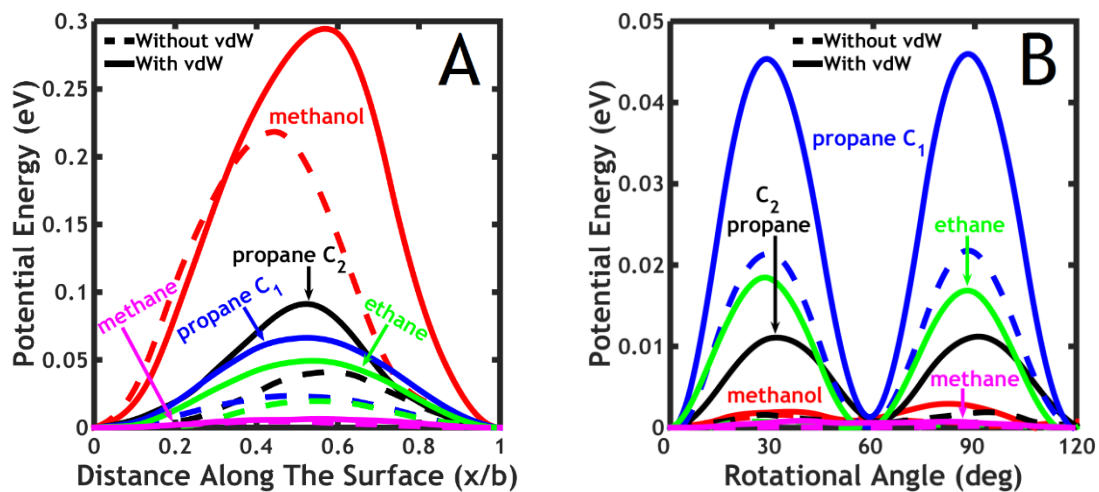


Figure 3.3 Calculated energy barrier versus coordinate of different adsorbates on Pt(111) for (A) hindered translations and (B) hindered rotations.

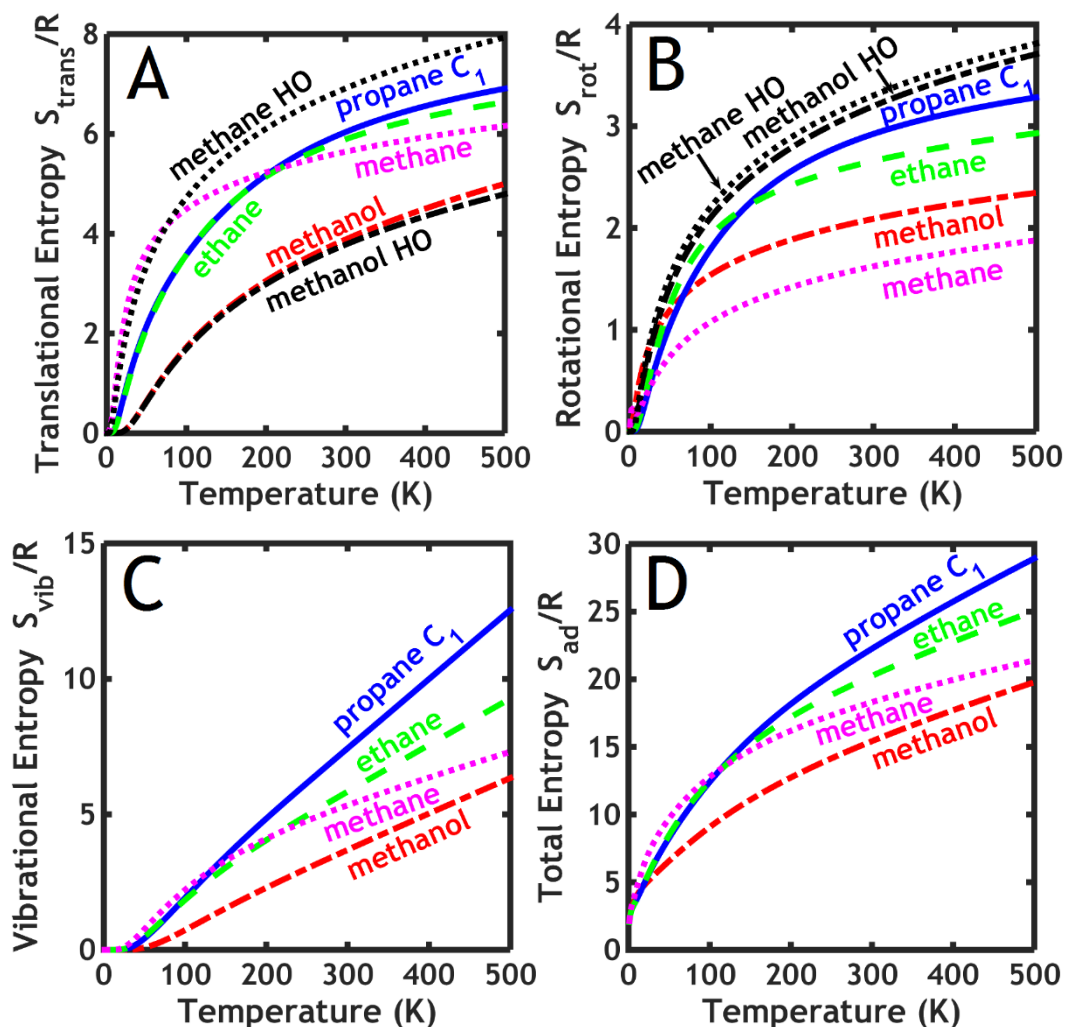


Figure 3.4 Entropy contributions as a function of temperature for (A) two hindered translations (not including the concentration-related part, S_I , see Table 3.3), (B) the hindered rotation, (C) the $3n-3$ vibrations (which include all internal vibrations and the z -vibration of the whole adsorbate), and (D) the total entropy. All curves are computed using DFT with vdW corrections included. Shown for comparison in A and B are the predictions of the harmonic oscillator approximation for methane and methanol (curves labeled “HO”).

Also shown in Figure 3.4 are the predictions of the HO approximation for the entropy contributions from xy motions (A) and rotation (B) parallel to the surface for adsorbed methane and methanol. As seen, the HO approximation severely overestimates the rotational entropy at high temperatures for both these adsorbates and the translational entropy at high temperature for methane. This can be understood with the equipartition theorem: The molar heat capacity of a harmonic oscillator is R in the high-temperature limit, but it is only $1/2 R$ for a free translator or free rotor. As

shown below, the entropy of the hindered translator and hindered rotor reach the free translator (ideal 2D gas) and free rotor limits as soon as kT exceeds the barrier height, W . Since kT never exceeds the translational barrier for methanol on this plot, this problem is not seen for methanol in Figure 3.4A. For this same reason (i.e., kT never exceeds the barrier by much), the HO approximation does better for the other adsorbates below 500 K in both translational and rotational entropy (not shown). Less severe is the underestimation of the HO approximation at intermediate and low temperatures (i.e., when kT is $\sim 10\%$ of the barrier), but it works well at very low temperatures. This is discussed in more detail below.

The standard-state entropies of the adsorbed species are compared to experimental values in Table 3.3 and Figure 3.5. The experimental entropies were reported only at one temperature for each adsorbate on Pt(111), which corresponds to the peak maximum in the experimentally reported temperature-programmed desorption (TPD) spectrum [37], so the calculated entropies are also at that temperature for each adsorbate, as listed in Table 3.3. These values all correspond to the standard-state adsorbate concentration which sets the entropy of an ideal 2D monatomic gas equal to $2/3$ the standard state entropy of the corresponding ideal 3D gas, i.e., approximately 1% of a monolayer [21]. Although not so clearly stated there, this was the standard state used for the experimental entropies [3, 37] that are listed in Table 3.3.

Table 3.3 Separation of the entropy contributions to the standard-state molar entropy of the probe adsorbates on Pt(111). At the temperature of the peak maximum for temperature programmed desorption, T_{max} , the concentration-related entropy (S_I), translational entropy (S_{trans} - S_I , from hindered translator (HT) and harmonic oscillator (HO)), rotational entropy (S_{rot} , from hindered rotor (HR) and harmonic oscillator (HO)), vibrational entropy (S_{vib} , from 3n-3 other normal modes), total molar entropy (S_{ad} , from hindered translator / hindered rotor model (HT/HR) and experiments), and standard-state concentrations are shown. The hindered translational and rotational entropies both include the zero-point energy corrections of Equations 3.8 and 3.19.

	Methanol		Propane (C ₂)		Propane (C ₁)		Ethane		Methane	
T_{max} (K)	210		139		139		106		63	
vdW?	yes	no	yes	no	yes	no	yes	no	yes	no
W_x/ (kT_{max})	16.3	12.1	7.62	3.42	5.53	1.95	5.40	2.15	1.17	0.844
W_r/ (kT_{max})	0.135	0.074	0.930	0.145	3.81	1.80	1.94	0.065	0.144	0.022
S_I/R	5.6	5.6	5.3	5.3	5.3	5.3	5.2	5.1	4.8	4.8
HT S_{trans}/R - S_I/R	3.2	3.5	3.9	5.0	4.3	5.5	3.7	4.8	3.9	4.0
HO S_{trans}/R - S_I/R	3.1	3.4	3.7	4.5	4.0	5.1	3.4	4.4	3.8	4.2
HR S_{rot}/R	1.9	1.9	1.7	1.6	2.2	2.5	2.0	1.8	0.9	0.4
HO S_{rot}/R	2.8	3.1	2.4	3.2	2.0	2.3	1.8	3.1	1.8	2.2
S_{vib}/R	2.4	2.6	3.0	3.9	3.1	4.5	2.0	3.0	1.2	1.2
HT/HR S_{ad}/R	13.1	13.6	14.0	15.8	15.0	17.9	12.9	14.7	10.8	10.4
Exp S_{ad}/R	14.7		15.5		15.5		14.2		11.7	
Std- State Conc [21] (N/A)⁰ (m⁻²)	1.48x10 ¹⁷		1.95x10 ¹⁷		1.95x10 ¹⁷		2.33x10 ¹⁷		3.30x10 ¹⁷	

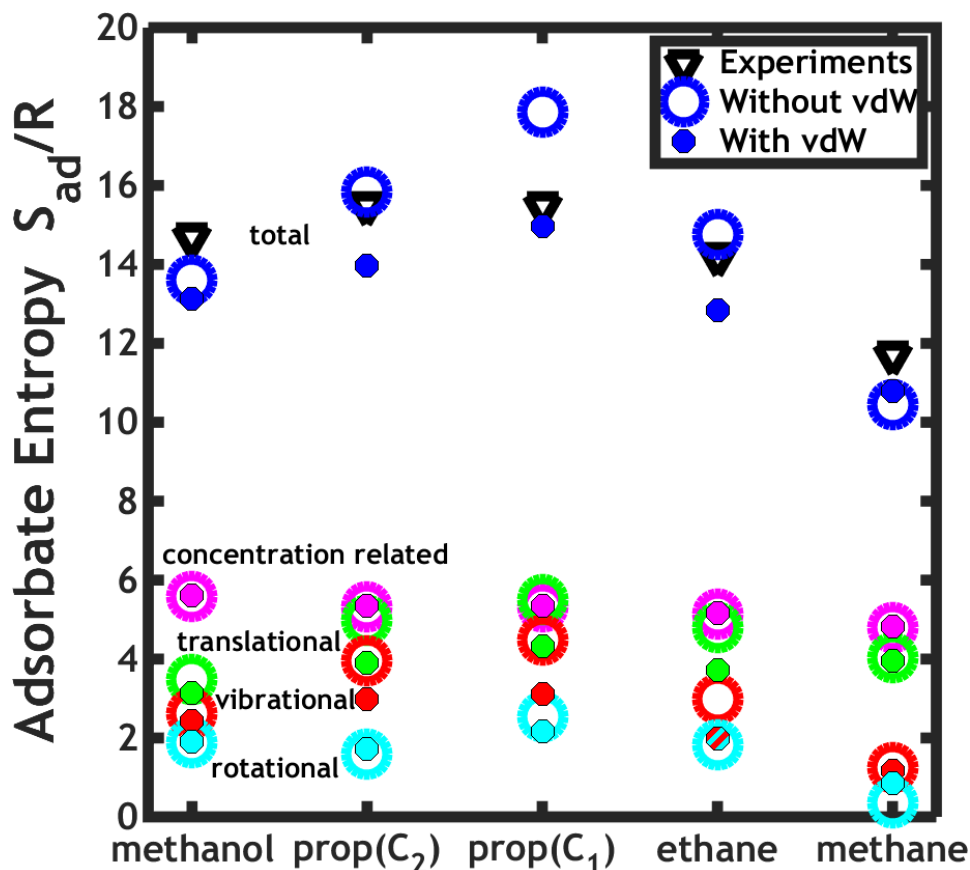


Figure 3.5 Plot of standard-state entropies determined for different adsorbates on Pt(111). Experimental standard-state entropies from [3, 37] are compared to those determined by the hindered translator and hindered rotor method, with various contributions to the total entropy also shown, with and without vdW corrections shown as dots and circles, respectively. The temperature is at the experimental peak maximum for temperature programmed desorption, which is 210 K for methanol, 139 K for propane, 106 K for ethane, and 63 K for methane.

The agreement between experiment and theory is excellent for the case where the energies were determined using DFT with vdW corrections, giving an average absolute value of the error of only 1.1 R, or 8 % for the four adsorbates (using the model for propane where it rotates about C_1). This increases to 1.3 R or 9 % when using DFT without vdW corrections. The entropies were up to 3 R larger for calculations without vdW corrections compared to those with vdW corrections. This was almost entirely due to the larger translational entropies, which is due to the smaller translational barriers, W_x , for DFT without vdW, which in turn is associated with the smaller heats of adsorption without vdW corrections. There is no significant

difference between the calculated entropies for the two different models used for propane rotation (i.e., about an end carbon atom (C_1) or central carbon atom (C_2)).

Standard-state adsorbate entropies (for both the stable adsorbed species and their transition states) calculated with this approach can be used together with transition-state theory to calculate rate constants and their pre-exponential factors for elementary reaction steps involving adsorbates [37]. The high accuracy of this approach for estimating adsorbate entropies implies that the pre-exponential factors determined using entropies estimated in this way should be quite accurate.

The various contributions to the standard-state entropy for each species are also presented in Table 3.3 and Figure 3.5. The dominant contributions are the concentration-related term (S_I) and the two hindered translations.

The S_I value of 4.8 to 5.6 R here depends strongly on the choice of standard-state concentration, which we chose here as recommended in [21] such that the standard-state entropy of an ideal 2D monatomic gas (i.e., in the limiting case of unhindered translation where the barrier drops to zero) equals 2/3 of the entropy of the corresponding ideal 3D gas of the same mass at its standard-state (i.e., at 1 bar pressure) [21]. This standard state corresponds to approximately 1% of the maximum coverage. This S_I contribution would drop to 1.7 R if a standard-state coverage of 1/2 the saturation coverage were chosen instead [21]. We chose the prior definition here to be consistent with the papers that reported the experimental entropies used here [3, 37], although that choice was only implied but never directly stated in those papers. It is also a value which gives a concentration-related contribution to the entropy (S_I) which is identical to the configurational entropy of an ideal lattice gas at the same standard-state surface concentration. We must admit that this difference of 3.1 to 3.9 R that arises from this (hidden) difference in standard-state concentrations was a large contributor to our earlier perception that the 2D lattice gas / harmonic oscillator model seriously underestimates adsorbate entropies [21].

The difference between the hindered translator / hindered rotor entropy and that estimated within the 2D lattice gas HO approximation is given by Equation 3.37 and shown in Table 3.3 at these experimental conditions. As seen in Table 3.3, the errors in the translational entropies using the HO / 2D lattice gas approximation are

rather small, averaging only 0.2 R per mode (x or y) for the four adsorbates using DFT with vdW corrections. The error in the HO approximation compared to the hindered rotor model is larger, often overestimating the entropy by over 1 R but still by less than 2 R. Thus, the HO approximation (i.e., using Equation 3.36 but omitting Equation 3.37) is moderately accurate at the temperatures of the experiments (but it severely overestimates entropies at higher temperatures – see below and Figure 3.4 A and B above). A more important effect at the experimental temperatures is the use of frequencies in Equation 3.36 that fit the energy minima and maxima to a cosine wave, as we have done here, instead of using the three lowest frequencies that come directly from the same DFT calculations, which are systematically higher. That latter approach leads to molar entropies that are lower by 1.5 R on average for the four adsorbates of Figure 3.5.

The entropies of these same three alkanes adsorbed on zeolite H-CHA at 303 to 313 K were estimated by Sauer's group with an approach that also goes beyond the harmonic oscillator approximation by including anharmonic effects and were found to agree well with experiments [38]. We used our new approach reported above to estimate the entropies of these alkanes on Pt(111) (with barriers estimated including vdW) but at the higher temperatures used in that paper. This provides a crude way to estimate the entropies of these adsorbates on that zeolite without doing DFT to get barrier heights on the zeolite, i.e., by assuming that the barriers for translation and rotation are the same as on Pt(111). In spite of this assumption, the entropies were found to be very close to those reported using Sauer's approach: 14.8 R vs. 14.8 R for methane, 16.9 R vs 18.7 R for ethane, 19.0 R vs 21.6 R for propane(C1), and 17.8 R vs. 16.9 R for propane(C2). These calculations were done at $\theta=0.5$ for direct comparison to the coverage used in Sauer's calculations. (Note that this is much higher than the coverage in Table 3.3 and thus gives entropies that are 3.7 R lower than the coverage of Table 3.3.) The approach used here is easier to implement than that developed by Sauer et al. [38].

Dependence of Adsorbate Entropy on System Parameters

To understand the qualitative dependences of the entropy upon the system parameters for the new hindered translator and hindered rotor models presented here, we calculated the translational and rotational contributions to the entropy of adsorbates for a wide variety of adsorbate parameters. Figure 3.6A shows how the translational contribution to the entropy for ethane on Pt(111) depends upon $W_x/(kT)$, the translational barrier normalized to kT , where $T = 106$ K, the experimental T_{max} for ethane on Pt(111). This is the curve labeled “ $mb^2 \times 1$ ”. It is calculated using only Equations 3.36 and 3.37 and does not include the concentration-dependent part, S_I , from Equation 3.38, so we will call it $S_{trans}-S_I$. As seen, this entropy is nearly constant when $W_x/(kT)$ is below 1 and then decreases with increasing $W_x/(kT)$, asymptotically approaching zero for large $W_x/(kT)$. The parameters m and b are always grouped together as mb^2 in the equations that determine S for the hindered translator. For a given value of $W_x/(kT)$, the translational entropy also increases with mb^2 (the adsorbate’s mass times the area per site) as shown. The general shape of $S_{trans}-S_I$ versus $W_x/(kT)$ is independent of mb^2 : $S_{trans}-S_I$ always increases with decreasing W_x from zero at high W_x , but then when $W_x/(kT)$ approaches 1 (indicated by the dashed vertical line), it levels off rapidly. When $W_x/(kT)$ drops below 1, it remains essentially constant at the value for an ideal 2D monatomic gas of the same mass ($S_{trans} - S_I = R \ln[(qe/\mathcal{A})/(M/\mathcal{A})] = R \ln[(qe/\mathcal{A})b^2] = R \ln[(2\pi mkTe/h^2)b^2]$, see above). As expected, this low- W_x limit increases by $R \ln 10 = 2.3 R$ and $R \ln 100 = 4.6 R$, respectively, when mb^2 is increased by 10- and 100-fold, respectively.

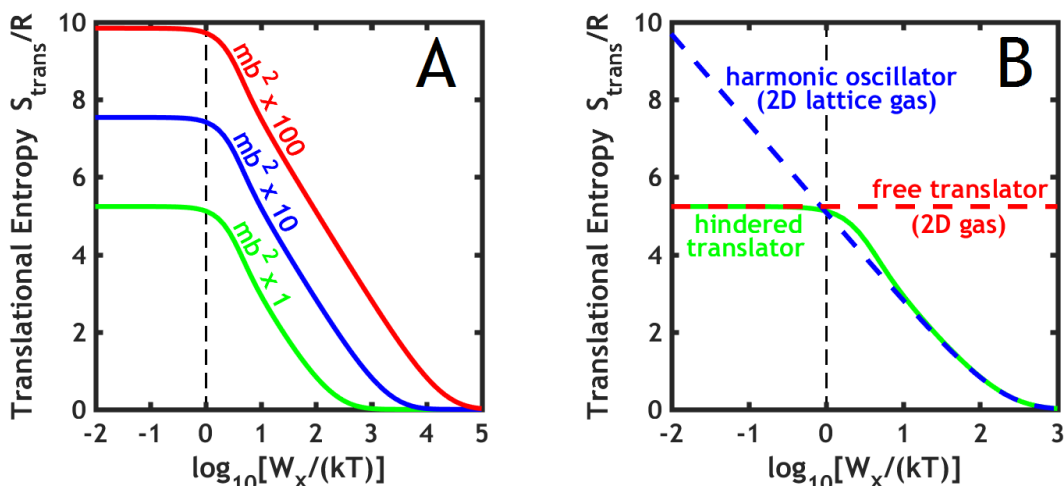


Figure 3.6 Effect of system parameters on the translational contribution to the entropy as determined from a hindered translator and compared with a harmonic oscillator and a free translator. (A) Effect of the translational barrier height, W_x , on the translational contribution to the molar entropy ($S_{trans}-S_I$) at $T = 106$ K estimated using the hindered translator model for ethane on Pt(111) (where $mb^2 = 2.30 \text{ amu}\cdot\text{nm}^2 = 3.82\times 10^{-45} \text{ kg}\cdot\text{m}^2$, labeled “ $mb^2 \times 1$ ” here) and for adsorbate systems with values of mb^2 (mass times area per site) that are 10-fold and 100-fold larger than this. For ethane on Pt(111), the barrier estimated using DFT with vdW corrections is $W_x = 7.90\times 10^{-21} \text{ J}$ or 4.76 kJ/mol ($W_x/k = 572 \text{ K}$), giving $\nu_x = 1.09\times 10^{12} \text{ s}^{-1}$ ($h\nu_x/k = 52.4 \text{ K}$). (B) The translational contribution to the molar entropy ($S_{trans}-S_I$) of ethane on Pt(111) at $T = 106$ K versus $W_x/(kT)$ estimated from the hindered translator model, compared with that from the corresponding 2D harmonic oscillator model. The flat region on the left gives the same limiting entropy (at low $W_x/(kT)$) as the corresponding ideal 2D monatomic gas. (The concentration-dependent contribution, S_I , is not included in either curve.).

Figure 3.6B compares the effect of barrier height on this same hindered translator entropy to that estimated by the 2D harmonic-oscillator (HO) approximation using the same frequency, ν_x from Equation 3.2 for both x and y modes, for ethane on Pt(111). When $W_x/(kT)$ exceeds 10, the HO approximation is almost the same as the true hindered translator entropy. When $W_x/(kT)$ is between 1 and 10, the HO approximation underestimates the hindered translator entropy but only by small amounts ($<0.5 R$, with a maximum difference of 0.46 R occurring when $W_x/(kT) = e = 2.7$). When $W_x/(kT)$ drops far below 1, the HO approximation greatly overestimates the hindered translator entropy, which levels out as noted above. It is clear from Figure 3.6 that, to a good approximation, the translational contribution to the hindered translator entropy equals that given by the 2D HO approximation (to within 0.46 R) when $W_x/(kT) \geq 1$ and that for an ideal 2D monatomic gas (to within

0.12 R) when $W_v/(kT) < 1$. The cutoff between these two behaviors is surprisingly sharp. The locations and magnitudes of these maximum errors do not depend on mb^2 (not shown). It is also clear that the HO approximation severely overestimates the entropy of the hindered translator when kT exceeds the barrier. This was explained above, where the same effect was seen in Figure 3.4A.

Figure 3.7A shows how the rotational entropy for ethane on Pt(111) depends upon $W_v/(kT)$, the rotational barrier normalized to kT , where $T = 106$ K, the experimental T_{max} for ethane on Pt(111). This is the curve labeled “ $I/n^2 \times 1$ ”. This entropy is nearly constant when $W_v/(kT)$ is below 1 and then decreases with increasing $W_v/(kT)$ and asymptotically approaches zero for large $W_v/(kT)$. As shown above, the parameters I and n are always grouped together as I/n^2 in the equations that determine S for the hindered rotor. For a given value of $W_v/(kT)$, the rotational entropy also increases with I/n^2 (the adsorbate’s reduced moment of inertia divided by the square of the number of energy barriers per rotation) as shown. The general shape of S_{rot} versus $W_v/(kT)$ is independent of I/n^2 , and when $W_v/(kT)$ drops below 1 (indicated by the dashed vertical line) it becomes essentially constant at the value for a free 1D rotor of the same moment of inertia, which is given by: $S_{rot} = R \ln[(qe)^{1/2}] = R \ln[((2\pi)^3(I/n^2)kTe/h^2)^{1/2}]$ [39]. As expected, in this low-barrier limit, S_{rot} increases by $R \ln 10^{1/2} = 1.15$ R and $R \ln 100^{1/2} = 2.30$ R when I/n^2 is increased by 10- and 100-fold, respectively.

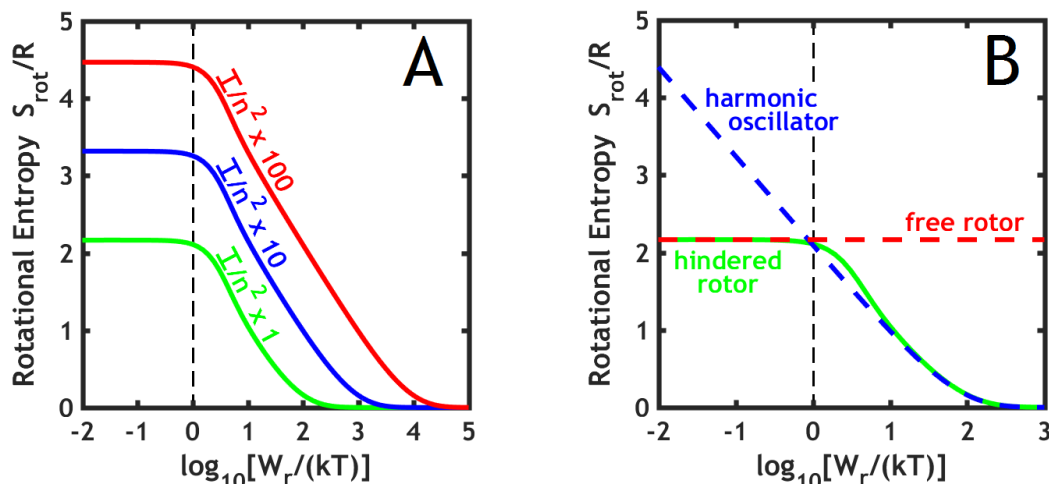


Figure 3.7 Effect of system parameters on the rotational contribution to the entropy as determined from a hindered rotor and compared with a harmonic oscillator and a free rotor. (A) Effect of the rotational barrier height, W_r , on the rotational contribution to the molar entropy at $T = 106$ K estimated using the hindered rotor model for ethane on Pt(111) (where I/n^2 is $0.0204 \text{ amu}\cdot\text{nm}^2 = 3.39 \times 10^{-47} \text{ kg}\cdot\text{m}^2$, labeled “ $I/n^2 \times 1$ ” here) and for adsorbate systems with values of I/n^2 (reduced moment of inertia divided by the square of the number of energy barriers per rotation) that are 10-fold and 100-fold larger than this. For ethane on Pt(111), the barrier here was estimated using DFT with vdW corrections and is $W_r = 2.83 \times 10^{-21} \text{ J}$ or 1.71 kJ/mol ($W_r/k = 205 \text{ K}$), giving $\nu_r = 1.03 \times 10^{12} \text{ s}^{-1}$ ($h\nu_r/k = 49.4 \text{ K}$). (B) The rotational contribution to the molar entropy for ethane on Pt(111) at $T = 106$ K versus $W_r/(kT)$ estimated from the hindered rotor model, compared with that from the corresponding harmonic oscillator model. The flat region on the left gives the same limiting entropy (at low $W_r/(kT)$) as the corresponding free 1D rotor.

Figure 3.7B compares the effect of barrier height on this same hindered rotor entropy to that estimated with the HO approximation using the same frequency, ν_r from Equation 3.15, for ethane on Pt(111). When $W_r/(kT)$ exceeds 10, the HO approximation is almost the same as the true hindered rotor entropy. When $W_r/(kT)$ is between 1 and 10, the HO approximation underestimates the hindered rotor entropy, but only by small amounts ($< 0.23 R$). When $W_r/(kT)$ drops far below 1, the HO approximation greatly overestimates the hindered rotor entropy. It is clear from Figure 3.7B that, to a good approximation, the hindered rotor entropy equals that from the HO approximation (to within $0.23 R$) when $W_r/(kT) \geq 1$ and equals that for a free 1D rotor entropy (within $0.06 R$) when $W_r/(kT) < 1$. Again, the cutoff between these two behaviors is surprisingly sharp. The locations and magnitudes of these maximum errors do not depend on I/n^2 (not shown). It is also clear that the HO

approximation severely overestimates the entropy of the hindered rotor when kT exceeds the barrier. This was explained above, where the same effect was seen in Figure 3.4B.

Although the comparisons to experimental entropies in Figure 3.5 were done for small molecules adsorbed on the Pt(111) surface, this model is also expected to be applicable for molecular fragments and other molecules and for other surfaces, provided they have potential energy surfaces similar to Figure 3.1.

For practical calculations of surface reaction rates, one could assume that W_x is $\sim 10\%$ of the adsorption energy (see above). Based on this estimate, if $W_x/(kT)$ is < 0.4 , it is probably safe to work with this estimate since it gives the entropy of the ideal 2D gas limit even if incorrect by a factor of 3. If $W_x/(kT) > 0.4$, W_x probably should be calculated more carefully, at least for transition states and adsorbed intermediates that have a significant degree of rate control. Similarly, one could assume that W_r is $\sim 1\%$ of the adsorption energy (see above). Based on this estimate, if $W_r/(kT)$ is < 0.4 , it is probably safe to work with this estimate since it gives the entropy of a free rotor even if this barrier estimate is incorrect by a factor of 3.

Conclusions

An easy to implement and accurate method to determine entropies of adsorbed molecules and molecular fragments was developed that models motions of the adsorbate parallel to the surface as two hindered translators and a hindered rotor. Our approach only requires the energy barrier heights for translations and rotation of the adsorbate for these modes, as well as the surface symmetry and nearest-neighbor site distance. The method is validated by proving that it has the proper high-temperature and low-temperature limits (i.e., the ideal 2D gas and ideal 2D lattice gas, respectively) and, for intermediate temperatures, by comparison of its predictions with experimental values for four adsorbed molecules on Pt(111). All barriers were calculated using DFT, both with and without vdW correction, and the frequencies were determined by fitting the DFT minima and maxima to a cosine wave. The entropies determined by this method using DFT with vdW corrections are in very good agreement with the experimental entropies.

The translational and rotational contributions to the entropy of a hindered translator / hindered rotor calculated with this new method are, in general, very closely approximated (to within $<0.25R$ error per mode) by the corresponding harmonic oscillator (i.e., lattice gas) entropy (calculated using v_x and v_r , respectively) when kT is less than the barrier. When kT exceeds the barrier, the hindered translator / hindered rotor model is closely approximated (to within $0.1 R$) by the entropy of an ideal 2D monatomic gas of the same mass and a free 1D rotor with the same moment of inertia, respectively. There exists a very sharp cutoff between the temperature ranges of applicability of these simple two approximations (see Figures 3.6 and 3.7). The harmonic oscillator / lattice gas model severely overestimates the entropy when kT exceeds the barrier by much.

These calculated adsorbate entropies, combined with transition-state theory, can be used to calculate rate constants and prefactors for elementary reaction steps to build microkinetic models.

Acknowledgements

Acknowledgment is made to the donors of the American Chemical Society Petroleum Research Fund for support of this research. We thank Lars Grabow, Jason Weaver, and Daniel Auerbach for very helpful discussions and careful reading of the manuscript.

References

- [1] C.T. Campbell, O. Lytken, Experimental Measurements of the Energetics of Surface Reactions, *Surface Science*, 603 (2009) 1365-1372.
- [2] W.A. Brown, R. Kose, D.A. King, Femtomole Adsorption Calorimetry on Single-Crystal Surfaces, *Chem. Rev.*, 98 (1998) 797-831.
- [3] C.T. Campbell, J.R.V. Sellers, The Entropies of Adsorbed Molecules, *Journal of the American Chemical Society*, 134 (2012) 18109-18115.
- [4] T.L. Hill, *An Introduction to Statistical Thermodynamics*, Addison-Wesley, Reading, MA, 1960.
- [5] J.A. Dumesic, G.W. Huber, M. Boudart, Microkinetics, in: H.K. G. Ertl, F. Schüth and J. Weitkamp (Ed.) *Handbook of Heterogeneous Catalysis*, 2nd Ed., Wiley-VCH Verlag GmbH, Weinheim, Germany, 2008, pp. 1445-1462.

- [6] K. Reuter, D. Frenkel, M. Scheffler, The Steady State of Heterogeneous Catalysis, Studied by First-Principles Statistical Mechanics, *Phys. Rev. Lett.*, 93 (2004) Art. #116105.
- [7] A.A. Gokhale, S. Kandoi, J.P. Greeley, M. Mavrikakis, J.A. Dumesic, Molecular-Level Descriptions of Surface Chemistry in Kinetic Models using Density Functional Theory, *Chemical Engineering Science*, 59 (2004) 4679-4691.
- [8] K. Honkala, A. Hellman, I.N. Remediakis, A. Logadottir, A. Carlsson, S. Dahl, C.H. Christensen, J.K. Norskov, Ammonia Synthesis from First-Principles Calculations, *Science*, 307 (2005) 555-558.
- [9] K. Reuter, M. Scheffler, First-Principles Kinetic Monte Carlo Simulations for Heterogeneous Catalysis: Application to the CO Oxidation at RuO₂(110), *Physical Review B*, 73 (2006).
- [10] A.A. Gokhale, J.A. Dumesic, M. Mavrikakis, On the Mechanism of Low-Temperature Water Gas Shift Reaction on Copper, *Journal of the American Chemical Society*, 130 (2008) 1402-1414.
- [11] K.S. Pitzer, W.D. Gwinn, Energy Levels and Thermodynamic Functions for Molecules with Internal Rotation I. Rigid Frame with Attached Tops, *Journal of Chemical Physics*, 10 (1942) 428-440.
- [12] R.B. McClurg, R.C. Flagan, W.A. Goddard, The Hindered Rotor Density-of-States Interpolation Function, *Journal of Chemical Physics*, 106 (1997) 6675-6680.
- [13] G. Henkelman, B.P. Uberuaga, H. Jónsson, A Climbing Image Nudged Elastic Band Method for Finding Saddle Points and Minimum Energy Paths, *Journal of Chemical Physics*, 113 (2000) 9901-9904.
- [14] G. Henkelman, H. Jónsson, Improved Tangent Estimate in the Nudged Elastic Band Method for Finding Minimum Energy Paths and Saddle Points, *Journal of Chemical Physics*, 113 (2000) 9978-9985.
- [15] H. Jónsson, G. Mills, K.W. Jacobsen, *Classical and Quantum Dynamics in Condensed Phase Simulations*, World Scientific, Singapore, 1998.
- [16] S.H. Payne, J.S. McEwen, H.J. Kreuzer, D. Menzel, Lateral Interactions and Nonequilibrium in Adsorption and Desorption. Part 2. A Kinetic Lattice Gas Model for (2x2)-(3O+NO)/Ru(001), *Surface Science*, 600 (2006) 4660-4669.
- [17] H.J. Kreuzer, Thermal Desorption Kinetics, *Langmuir*, 8 (1992) 774-781.
- [18] S.H. Payne, J.S. McEwen, H.J. Kreuzer, D. Menzel, Adsorption and Desorption of CO on Ru(0001): A Comprehensive Analysis, *Surface Science*, 594 (2005) 240-262.
- [19] L.D. Peterson, S.D. Kevan, Lattice-Gas Virial Coefficients from Isothermal Desorption Measurements: CO on Cu(001) and Cu(011), *Physical Review Letters*, 65 (1990) 2563-2566.

- [20] K.J. Wu, S.D. Kevan, Isothermal Coverage Dependent Measurements of NH₃ and ND₃ Desorption from Cu(001), *Journal of Chemical Physics*, 95 (1991) 5355-5363.
- [21] C.T. Campbell, L.H. Sprowl, L. Arnadottir, Equilibrium Constants and Rate Constants for Adsorbates: Two-Dimensional (2D) Ideal Gas, 2D Ideal Lattice Gas, and Ideal Hindered Translator Models, *Journal of Physical Chemistry C*, 120 (2016) 10283-10297.
- [22] D.J. Donaldson, M. Ammann, T. Bartels-Rausch, U. Poeschl, Standard States and Thermochemical Kinetics in Heterogeneous Atmospheric Chemistry, *Journal of Physical Chemistry A*, 116 (2012) 6312-6316.
- [23] D.A. McQuarrie, *Statistical Mechanics*, University Science Books, Sausalito, 2000.
- [24] G. Kresse, J. Hafner, Ab initio Molecular Dynamics for Liquid Metals, *Physical Review B*, 47 (1993) 558–561.
- [25] G. Kresse, J. Hafner, Ab initio Molecular-Dynamics Simulation of the Liquid-Metal-Amorphous-Semiconductor Transition in Germanium, *Physical Review B*, 49 (1994) 14251–14269.
- [26] G. Kresse, J. Furthmuller, Efficiency of Ab-Initio Total Energy Calculations for Metals and Semiconductors Using a Plane-Wave Basis Set, *Computational Materials Science*, 6 (1996) 15-50.
- [27] G. Kresse, J. Furthmuller, Efficient Iterative Schemes for Ab Initio Total-Energy Calculations Using a Plane-Wave Basis Set, *Physical Review B*, 54 (1996) 11169-11186.
- [28] G. Kresse, D. Joubert, From Ultrasoft Pseudopotentials to the Projector Augmented-Wave Method, *Physical Review B*, 59 (1999) 1758-1775.
- [29] P.E. Blöchl, Projector Augmented-Wave Method, *Physical Review B*, 50 (1994) 17953-17979.
- [30] J.P. Perdew, K. Burke, M. Ernzerhof, Generalized Gradient Approximation Made Simple, *Physical Review Letters*, 77 (1996) 3865-3868.
- [31] J.P. Perdew, K. Burke, M. Ernzerhof, Generalized Gradient Approximation Made Simple (vol 77, pg 3865, 1996), *Physical Review Letters*, 78 (1997) 1396-1396.
- [32] S. Grimme, J. Antony, S. Ehrlich, H. Krieg, A Consistent and Accurate Ab initio Parametrization of Density Functional Dispersion Correction (DFT-D) for the 94 Elements H-Pu, *Journal of Chemical Physics*, 132 (2010).
- [33] H.J. Monkhorst, J.D. Pack, Special Points for Brillouin-Zone Integrations, *Physics Review B*, 13 (1976) 5188-5192.
- [34] N.W. Ashcroft, N.D. Mermin, *Solid State Physics*, Holt, Rinehart and Winston, N. Y., 1976.

- [35] S.R. Bahn, K.W. Jacobsen, An Object-Oriented Scripting Interface to a Legacy Electronic Structure Code, *Computing in Science & Engineering*, 4 (2002) 56-66.
- [36] A.J. Medford, C. Shi, M.J. Hoffmann, A.C. Lausche, S.R. Fitzgibbon, T. Bligaard, J.K. Norskov, CatMAP: A Software Package for Descriptor-Based Microkinetic Mapping of Catalytic Trends, *Catalysis Letters*, 145 (2015) 794-807.
- [37] C.T. Campbell, L. Árnadóttir, J.R.V. Sellers, Kinetic Prefactors of Reactions on Solid Surfaces, *Zeitschrift Fur Physikalische Chemie-International Journal of Research in Physical Chemistry & Chemical Physics*, 227 (2013) 1435-1454.
- [38] G. Piccini, M. Alessio, J. Sauer, Y. Zhi, Y. Liu, R. Kolvenbach, A. Jentys, J.A. Lercher, Accurate Adsorption Thermodynamics of Small Alkanes in Zeolites. Ab initio Theory and Experiment for H-Chabazite, *Journal of Physical Chemistry C*, 119 (2015) 6128-6137.
- [39] D.G. Truhlar, A Simple Approximation for the Vibrational Partition Function of a Hindered Internal Rotation, *Journal of Computational Chemistry*, 12 (1991) 266-270.

Supporting Information

Table 3.S1 Binding energies, in eV, of the initial state, translational transition state, and rotational transition state on a Pt(111) surface.

	Methanol		Propane (C ₂)		Propane (C ₁)		Ethane		Methane	
	yes	no	yes	no	yes	no	yes	no	yes	no
vdW included	yes	no	yes	no	yes	no	yes	no	yes	no
Initial State	-0.73	-0.31	-0.66	-0.06	-0.64	-0.05	-0.46	-0.05	-0.27	-0.04
Trans TS	-0.43	-0.09	-0.56	-0.02	-0.57	-0.03	-0.41	-0.03	-0.26	-0.03
Rot TS	-0.73	-0.30	-0.64	-0.06	-0.59	-0.03	-0.44	-0.04	-0.27	-0.04

Table 3.S2 Distances, in Ångstroms, between O and C atoms and the Pt(111) surface for the initial state, translational transition state, and rotational transition state configurations. Propane (C₂) has its central (C₂) carbon atom closest to the surface, while propane (C₁) has its terminal (C₁) carbon atoms closer to the surface.

		Methanol		Propane (C ₂)		Propane (C ₁)		Ethane		Methane	
		yes	no	yes	no	yes	no	yes	no	yes	no
Initial State	O	2.24	2.29								
	C1	3.03	3.13	3.35	3.87	3.23	3.60	3.19	3.52	3.32	3.80
	C2			3.13	3.35	3.36	3.88	3.36	4.06		
	C3			3.33	3.88	3.30	3.65				
Trans TS	O	2.76	2.87								
	C1	3.42	3.67	3.45	4.00	3.36	3.70	3.35	3.64	3.38	3.86
	C2			3.24	3.52	3.48	4.00	3.50	4.21		
	C3			3.55	4.06	3.43	3.84				
Rot TS	O	2.26	2.29								
	C1	3.05	3.13	3.35	3.87	3.24	3.60	3.20	3.52	3.32	3.80
	C2			3.13	3.35	3.43	3.89	3.36	4.06		
	C3			3.33	3.88	3.40	3.66				

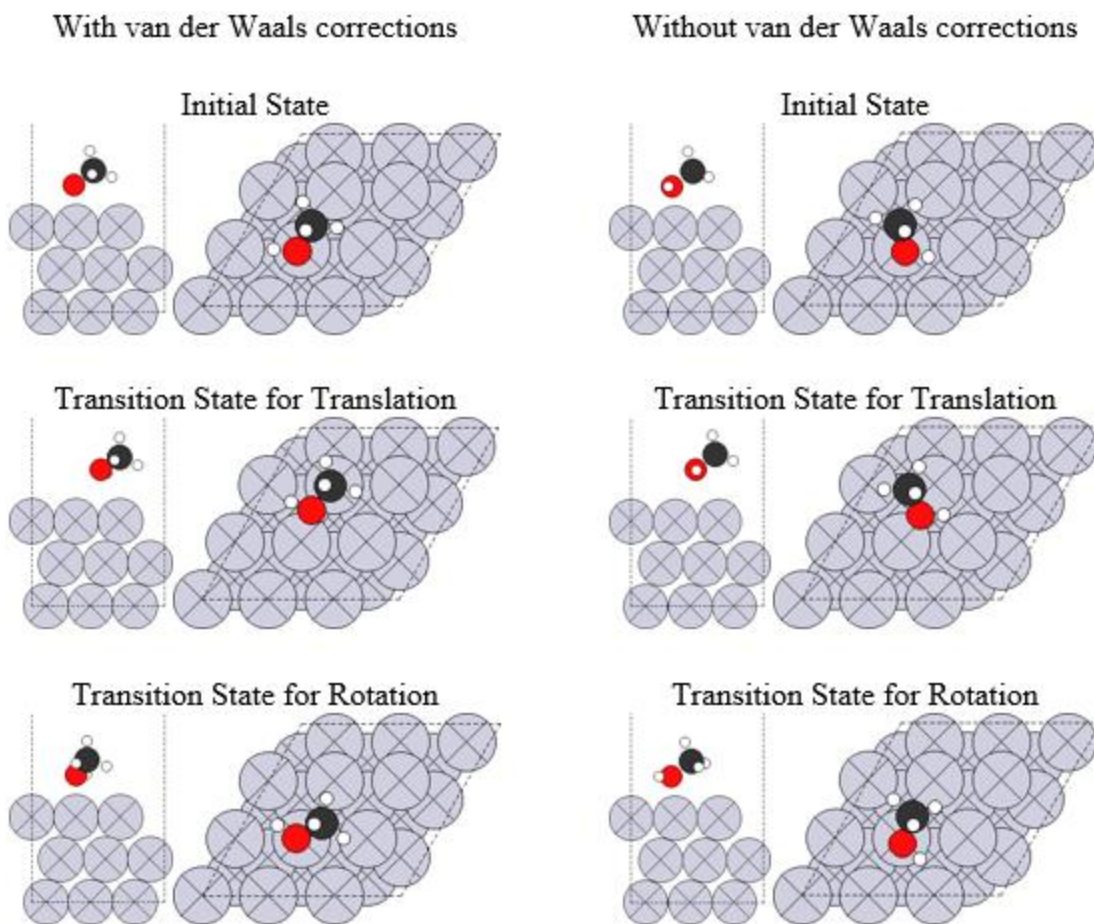


Figure 3.S1 Initial state and transition state binding configurations for methanol on Pt(111) with and without van der Waals corrections.

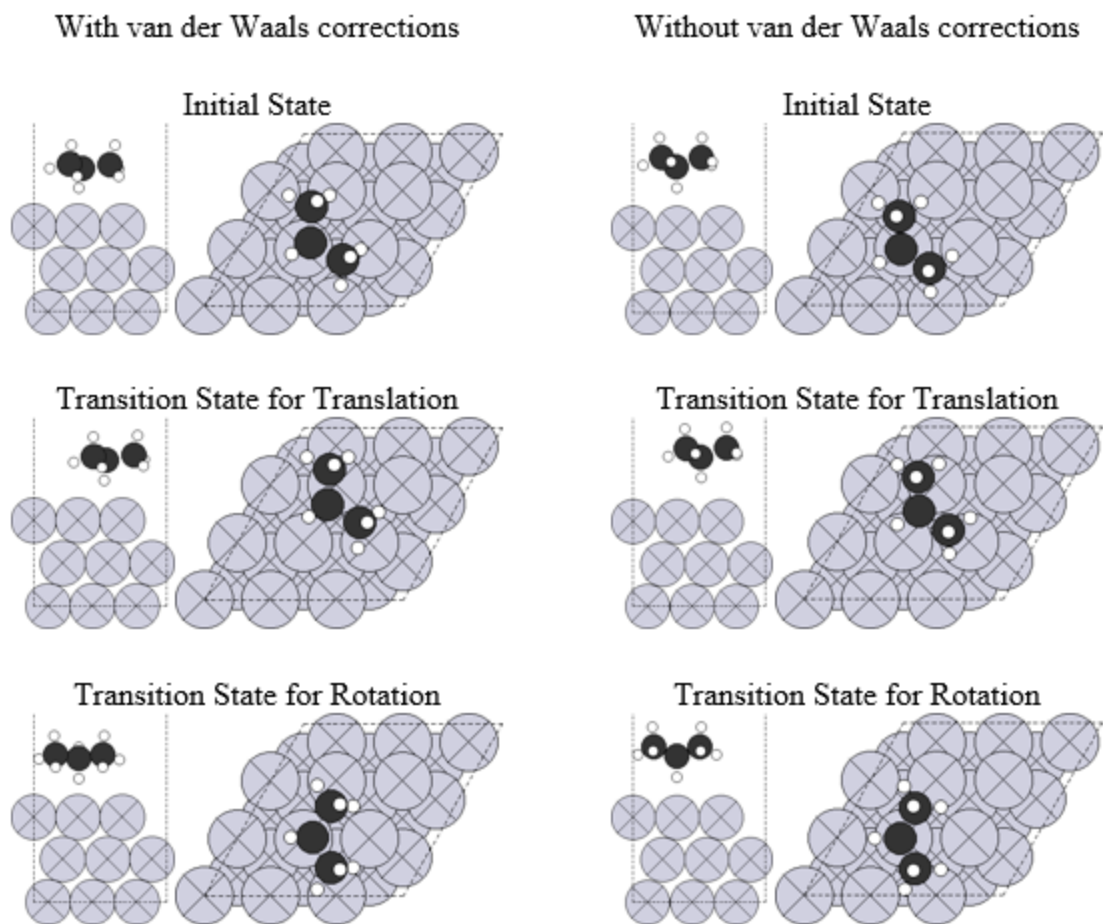


Figure 3.S2 Initial state and transition state binding configurations for propane (C₂) on Pt(111) with and without van der Waals corrections.

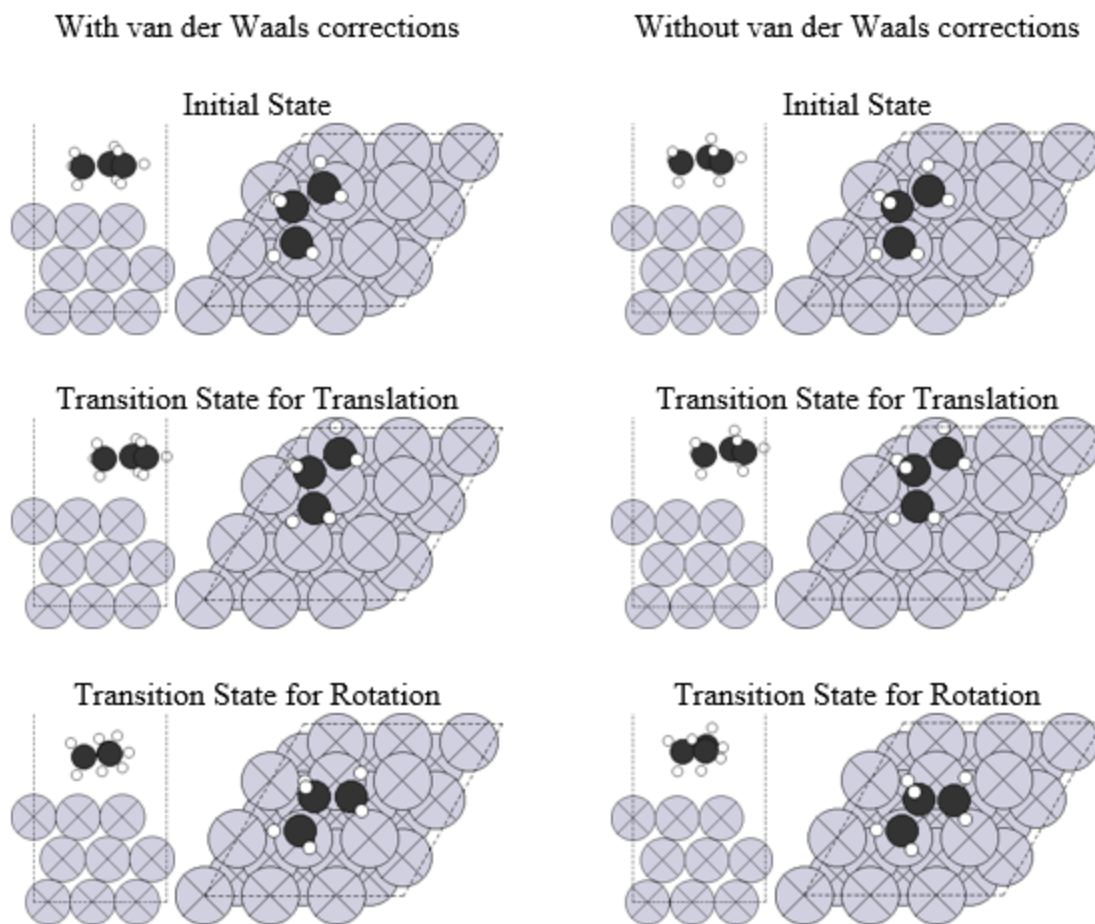


Figure 3.S3 Initial state and transition state binding configurations for propane (C1) on Pt(111) with and without van der Waals corrections.

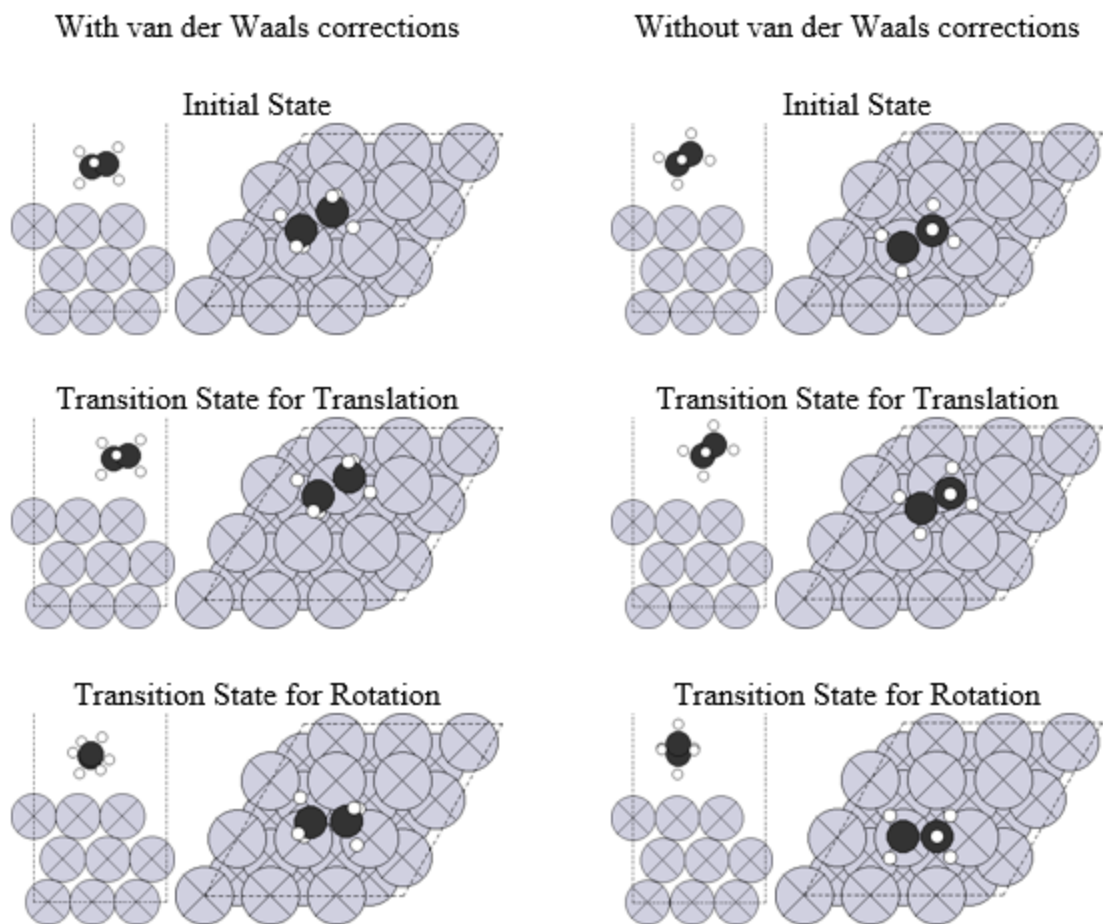


Figure 3.S4 Initial state and transition state binding configurations for ethane on Pt(111) with and without van der Waals corrections.

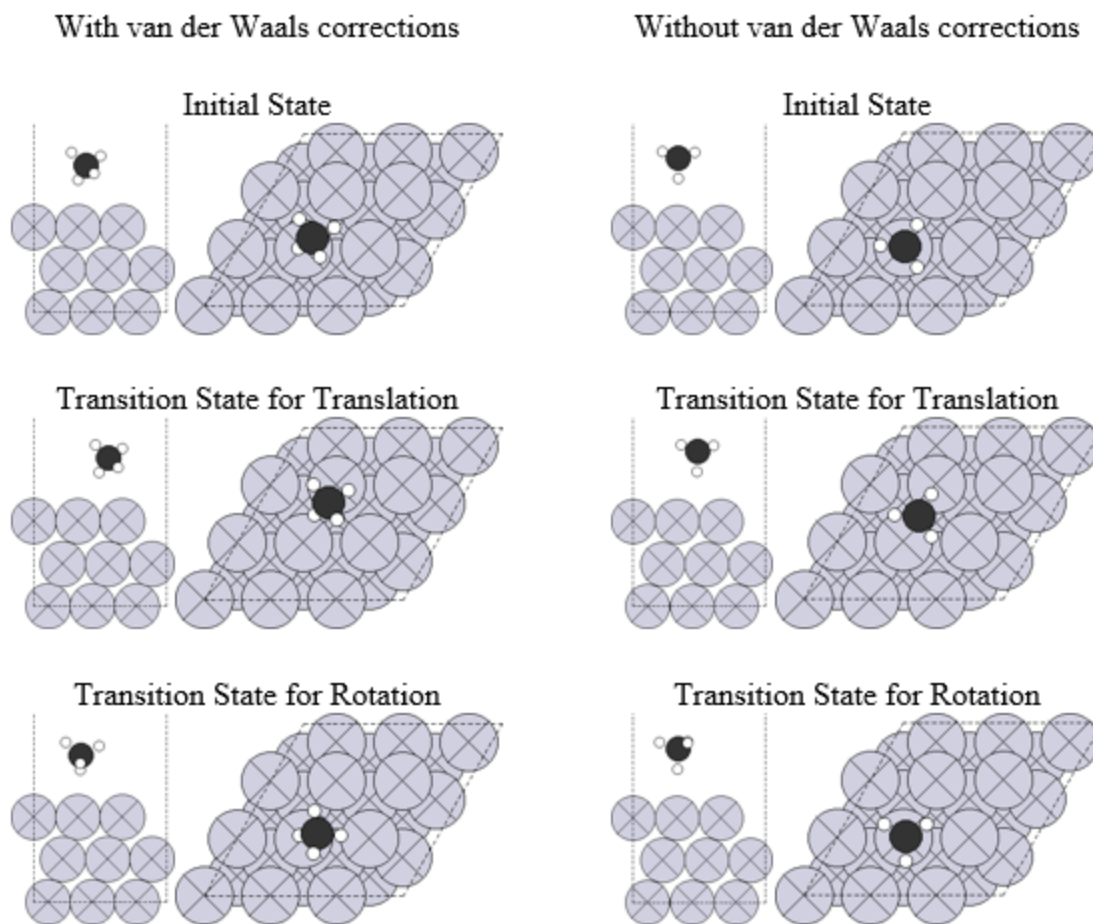


Figure 3.S5 Initial state and transition state binding configurations for methane on Pt(111) with and without van der Waals corrections.

CHAPTER 4

APPLICATIONS OF THE HINDERED TRANSLATOR AND HINDERED ROTOR MODEL

Introduction

Determination of accurate adsorbate entropies is becoming increasingly important for understanding reaction kinetics and thermodynamics. The entropy of gas phase species and adsorbed species is required to predict the results of a chemical process from a microkinetic model [1] or maximum rate analysis [2]. The entropies of adsorbed species can be estimated as fractions of its gas phase entropy, as has been shown by Campbell and coworkers [3, 4]. However, more direct approaches to determine adsorbate entropies for computational studies exist such as the 2D ideal lattice gas model (also known as the harmonic oscillator approximation) and the 2D ideal gas model (also known as the free translator / free rotor model).

The harmonic oscillator approximation is commonly used to determine the adsorbate entropy from its vibrational frequencies using density functional theory [5, 6]. The hindered translator / hindered rotor model was developed to mitigate the shortcomings of the harmonic oscillator approximation and to bridge the gap between the harmonic oscillator approximation and the free translator / free rotor model. At the low temperature limit, the harmonic oscillator approximation is valid, as it assumes the adsorbate to be stuck in a potential energy well with only vibrational modes. At the high temperature limit, the free translator / free rotor model is valid, as it assumes no energy barrier to translation or rotation such that the adsorbate can translate and rotate freely. The hindered translator / hindered rotor model smoothly transitions between the two limits and may be valid over a wide temperature range.

In our previous paper [7], we introduced the hindered translator / hindered rotor model for adsorbates and tested the model by calculating the entropy of methanol, propane, ethane, and methane bound to a Pt(111) surface. Further progress has been made by Bajpai et al. [8] to benchmark the hindered translator model by calculating free energies and entropies for H, C, N, O, and S on Pt(100) and Au(100) surfaces. The hindered translator model has also been extended to microkinetic modeling by Jørgensen and Grönbeck [9], who determined the effect of different entropy models on the catalytic activity of CO oxidation on Pt(111). The work to benchmark and understand the hindered translator / hindered rotor model is reviewed herein.

The hindered translator / hindered rotor model may be used by researchers via the equations presented in our previous paper [7], or additionally the model can be accessed via two commonly used python packages, Atomic Simulation Environment (ASE) [10, 11] and Catalysis Microkinetic Analysis Package (CatMAP) [12]. ASE is used to set up, manipulate, run, visualize, and analyze atomic simulations. The thermochemistry module in ASE can be used during post-processing to calculate the internal energy, entropy, and free energy of adsorbates using either the harmonic adsorbate model or the hindered adsorbate model. CatMAP is used to automatically create microkinetic models for use in catalyst screening. The thermodynamics module in CatMAP is used to describe the free energy of every species in the microkinetic model, in which the adsorbates may be approximated as a harmonic adsorbate or a hindered adsorbate. The ASE and CatMAP documentation and code are presented at the end of this chapter.

Discussion

The harmonic oscillator approximation, hindered translator model, and free translator model differ in how they approximate the potential energy surface, as seen in Figure 4.1. The harmonic oscillator approximation assumes that the potential energy is modeled as a parabolic potential such that the adsorbate is stuck in a potential energy well with only vibrational degrees of freedom. The other limit is the free translator, which assumes a flat potential with zero energy such that the adsorbate is able to translate and rotate freely on the surface.

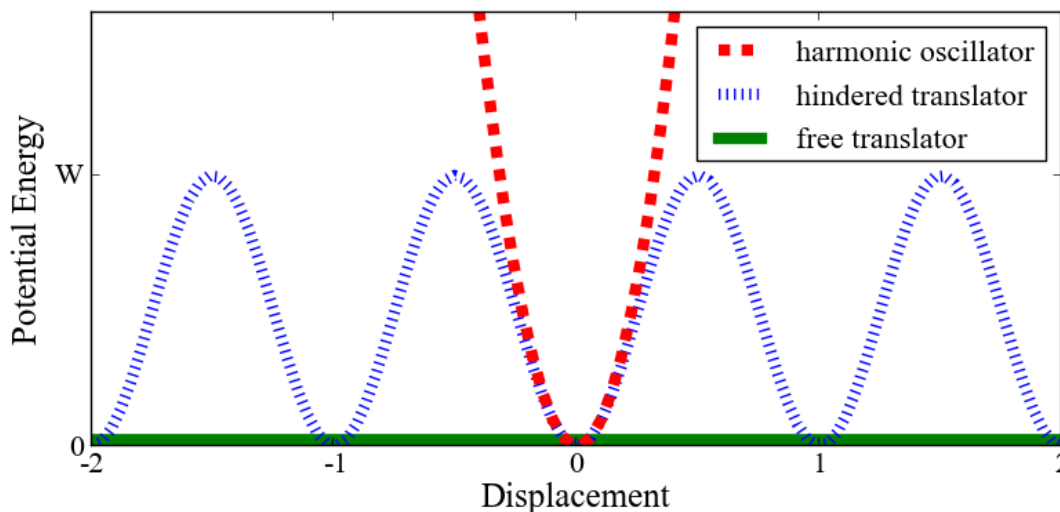


Figure 4.1 The one-dimensional potential energy surface as approximated by the harmonic oscillator, hindered translator, and free translator models. A displacement of one unit in the hindered translator model corresponds to a translation to a neighboring energy equivalent site or a rotation to an energy equivalent configuration, with an energy barrier W for adsorbate translation or rotation.

The hindered translator (or rotor) model goes between the harmonic oscillator and free translator (or rotor) models and assumes a sinusoidal potential, shown in Figure 4.1, such that the adsorbate must overcome an energy barrier in order to translate (or rotate) on the surface. In the hindered translator (or rotor) sinusoidal potential, the peak-to-peak amplitude is given by the energy barrier for translation, W_x or W_y , (or rotation, W_r). The wavelength in the sinusoidal potential is defined by the symmetry of the energy landscape and is given by the distance on the surface an adsorbate translates until it reaches an energy equivalent minima or the degree of rotation an adsorbate rotates until it reaches an energy equivalent minima.

A chemical species may contain translational, rotational, or vibrational degrees of freedom, with each mode having a contribution to the partition function. The contribution of each adsorbate mode as given by the harmonic oscillator (HO) model is

$$q_i^{HO} = \frac{\exp\left[\frac{-hv}{2kT}\right]}{1 - \exp\left[\frac{-hv}{kT}\right]}, \quad (4.1)$$

where h is Planck's constant, ν is the HO frequency, k is the Boltzmann constant, and T is the temperature. At one extreme, the harmonic oscillator approximation only assumes vibrational motion, while at the other extreme the free translator model assumes the adsorbate is free to translate on the surface. The free translator model considers the two modes of motion parallel to the surface to be translational modes, with the remaining modes considered to be vibrational modes that are modeled as harmonic oscillators. The partition function for the free translator (FT) in the two translational modes parallel to the surface is

$$q_{xy}^{FT} = A \frac{2\pi mkT}{h^2}, \quad (4.2)$$

where A is the area and m is the adsorbate mass.

The hindered translator / hindered rotor model assumes that motion parallel to the surface is hindered by some energy barrier, instead of being confined to only vibrate as in the harmonic oscillator approximation or being freely available to move as in the free translator model. The partition function for the hindered translator model for the two translational modes parallel to the surface is

$$q_{xy}^{HT} = M \left(\frac{\pi r_x}{T_x} \right) \exp \left[-\frac{r_x}{T_x} \right] \frac{\exp \left[\frac{-1}{T_x} \right]}{\left(1 - \exp \left[\frac{-1}{T_x} \right] \right)^2} I_0^2 \left[\frac{r_x}{2T_x} \right] \exp \left[\frac{2}{(2+16r_x)T_x} \right], \quad (4.3)$$

where M is the number of surface sites, r_x is the ratio of the energy barrier to the frequency $r_x = W_x/(h\nu)$, T_x is the ratio of the temperature to the frequency $T_x = kT/(h\nu)$ and I_0 is the zero-order modified Bessel function of the first kind. The partition function in Equation 4.3 assumes that the energy barriers in the x- and y-directions are the same, i.e., $W_x = W_y$. The two translational frequencies are also the same and are defined as $\nu = \sqrt{W_x/(2mb^2)}$ where m is the adsorbate mass and b is the distance between energy equivalent minima. If the x- and y- directions are not energetically equal, the partition function can easily be divided into the individual components as $q_{xy} = q_x q_y$.

Just as the translational motion parallel to the surface is modeled with the hindered translator model, the rotational motion parallel to the surface is modeled with the hindered rotor model. The rotation parallel to the surface is the helicopter-like rotation, or rotation about the z-axis perpendicular to the surface. This is not to be confused with perpendicular, cartwheel-like rotations about the x- and y-axes, as incorrectly stated by Conti and Cecchini [13]. All remaining modes of motion are considered to be vibrational and are modeled with the harmonic oscillator approximation. The partition function for the hindered rotor is

$$q_r^{HR} = \left(\frac{\pi r_r}{T_r}\right)^{1/2} \exp\left[-\frac{r_r}{2T_r}\right] \frac{\exp\left[\frac{-1}{2T_r}\right]}{\left(1 - \exp\left[\frac{-1}{T_r}\right]\right)} I_0\left[\frac{r_r}{2T_r}\right] \exp\left[\frac{1}{(2+16r_r)T_r}\right], \quad (4.4)$$

where r_r is the ratio of the energy barrier to the frequency $r_r = W_r/(h\nu)$, T_r is the ratio of the temperature to the frequency $T_r = kT/(h\nu)$, and the frequency is defined as $\nu = (1/(2\pi))\sqrt{n^2 W_r/(2I)}$, where n is the number of equivalent minima in a full rotation and I is the reduced moment of inertia of the adsorbate about the axis of rotation. Monatomic adsorbates and linear adsorbates bound with their molecular axis perpendicular to the surface do not have rotational motion parallel to the surface and thus would not use the hindered rotor model.

The potential energy surface may also be sampled explicitly instead of assuming that the potential energy surface is parabolic, sinusoidal, or flat as in the harmonic oscillator approximation, hindered translator model, or free translator model, respectively. The partition function for semiclassical potential energy sampling (PES-sc) along the translational modes parallel to the surface is

$$q_{xy}^{PES-sc} = \frac{2\pi mkT}{h^2} \iint \exp\left[\frac{-V(x,y)}{kT}\right] dx dy, \quad (4.5)$$

where $V(x,y)$ is the potential energy surface in the xy plane. Semiclassical potential energy sampling fails at the limit of low temperature because it does not take into account the zero point energy. At low temperatures, quantum potential energy

sampling (PES-q) must be done by numerically solving the Schrödinger equation to get the accessible energy states, E_i , which go into calculating the partition function as

$$q_{xy}^{PES-q} = \sum_{i=1} \exp \left[-\frac{E_i}{kT} \right], \quad (4.6)$$

In our previous paper [7], we calculated the entropy of methanol, propane, ethane, and methane on Pt(111) using the hindered translator and hindered rotor model and compared to experiments. The density functional theory calculations with van der Waals corrections compare to experiments nicely with entropies, in units of the gas constant R, for methanol (HT: 13.1, exp: 14.7), propane bound through its end carbon (HT: 15.0, exp: 15.5), ethane (HT: 12.9, exp: 14.2), and methane (HT: 10.8, exp: 11.7). The entropies determined with the hindered translator and hindered rotor model are better than those determined using the harmonic oscillator approximation and compare very well to experiments, with differences of about 1 R or 0.1 meV/K.

Bajpai et al. [8] determined free energies and entropies for H, C, N, O, and S on Au(100) and Pt(100) and compared the values from the hindered translator (HT) model, harmonic oscillator (HO) approximation, and free translator (FT) model to values from the potential energy sampling (PES) method. They first calculated the potential energy surfaces and found that they divided into three groups: one group with the adsorbate at hollow sites and translational barriers larger than 0.45 eV (C/Au, N/Au, S/Au, C/Pt, and S/Pt), a second group with the adsorbate at hollow sites but translational barriers smaller than 0.15 eV (O/Au and N/Pt), and a third group with the adsorbates bound at bridge sites (H/Pt, H/Au, and O/Pt). The monatomic species have only a vibrational mode in the direction perpendicular to the surface, which is always represented as a harmonic oscillator, and two translational modes parallel to the surface, which are represented by the different models for comparison.

For all potential energy surfaces studied by Bajpai et al. [8], the HT model gave free energies that were below the HO and PES models and above the FT model as well as entropies that were all above the HO and PES models but below the FT model, suggesting that the HT model skews towards the FT model. For the group one species in hollow sites with higher translational barriers, the PES model is fit almost

exactly by the HO model with the HT model giving slightly lower (~ 100 meV at 1200 K) free energies and slightly higher (~ 0.1 meV/K at 1200 K) entropies. Bajpai et al. [8] attributed the difference between the HT and PES models to the failure in the sinusoidal potential of the hindered translator model to capture the curvature of the potential energy surface. Bajpai et al. [8] also found that free energies from the HT model match very well to the PES model for small frequencies and low energy barriers while the HO model matches very well to the PES model for larger frequencies and higher energy barriers. This suggests that it is not ideal to mix the two models.

The group two species in hollow sites with low translational barriers have potential energy surfaces that are composed of a double walled potential in which there is an energy barrier to transition from a global minima hollow site to a local minima bridge site. There are now two choices for the parameter b in the HT model: the standard choice for b representing the distance between energy equivalent minima, or an adjusted b representing the distance between the energy barriers around the hollow site global minimum. Bajpai et al. [8] determined that the HT model with the adjusted b parameter fits the PES model very well, with free energies at 1200 K that are only about 40 meV lower than the PES model and entropies that are about 0.01 meV/K higher than the PES model. The HT model with the unadjusted b parameter and the HO model have similar differences to the PES model of about 150 meV for free energies and 0.1 meV/K for entropies at 1200 K, although the differences are in opposite directions for the two models. Bajpai et al. [8] also found that lower frequencies compare better to the PES model with the unadjusted HT model and higher frequencies compare better to the PES model with the adjusted HT model. This drove them to determine an optimal ratio between the unadjusted b parameter and the adjusted b parameter, given as a sigmoidal function for b/b_{adjusted} vs $\ln(W/(kT))$, that could be used to improve the fit of the HT model for various barrier heights and frequencies.

The third group with adsorbates at bridge sites, has an asymmetric potential energy landscape for the two directions parallel to the surface. In this case there are two ways to parameterize the HT model: one in which the adsorbate is forced to stay

in the perpendicular x- and y-directions and the other in which the adsorbate may move along its lowest energy path to reach the next energy minima in the x- and y-directions. Bajpai et al. [8] found that the parameterization of the HT model in the two different ways gives similar free energies and entropies, with the perpendicular HT model performing slightly better than the minimum-energy HT model when compared to the PES model. In some instances, the perpendicular HT model performs better than the HO model and gives the same free energy and entropy as the PES model, while in another instance the perpendicular HT and HO models performs similarly but differs in the opposite direction from the PES model by about 50 meV for the free energy and about 0.03 meV/K for the entropy.

As an extension to calculating the adsorbate entropy, Jørgensen and Grönbeck [9] explored the influence of using different translational entropy models on the catalytic activity of CO oxidation on Pt(111) by comparing the harmonic oscillator (HO) approximation, hindered translator (HT) model, free translator (FT), potential energy sampling (PES) model, and experimental results. They changed the partition function model for the adsorbate, but treated all transition state partition functions with only the harmonic oscillator approximation. As discussed by Bajpai et al. [8], the mixing of different partition function models is not ideal because errors can be compounded. However, when there are no alternatives to calculating the transition state entropy, this must be done.

The HT entropies for adsorbed CO and O on Pt(111) are determined by Jørgensen and Grönbeck [9] to be above the HO and PES entropies and below the FT entropies, similar to the calculations by Bajpai et al. [8]. The PES model is fit best by the HT model for CO with a difference of only about 0.04 meV/K at 1000 K, while the PES model is fit slightly better by the HO model than the HT model for O and has an entropy difference of about 0.1 meV/K between the HT and PES models at 1000 K.

The CO oxidation prefactors calculated by Jørgensen and Grönbeck [9], shown in Table 4.1, are orders of magnitude different for the different models, with the HO model giving the highest prefactors, the FT model giving the lowest prefactors, and the PES and HT prefactors in the middle. For CO desorption, the HT

models fits the PES prefactor the best, but the HO model fits the experimental prefactor the best, showing some discrepancy between the PES model and the experiment. The experimental O₂ desorption prefactor is represented best by the HT model, which performs better than the PES model. For CO oxidation, the HT model is the only model that gives a prefactor close to that given by the PES model. The HO model gives a CO oxidation prefactor two orders of magnitude larger and the FT model gives it two orders of magnitude smaller than that given by the PES model.

Table 4.1 Prefactors for the CO oxidation reaction mechanism on Pt(111) using the harmonic oscillator (HO), hindered translator (HT), free translator (FT), and potential energy sampling (PES) models compared to experiments. The prefactor for CO adsorption is $1.6 \times 10^3 \text{ Pa}^{-1} \text{ s}^{-1}$ and for O₂ adsorption is $1.6 \times 10^2 \text{ Pa}^{-1} \text{ s}^{-1}$.

	CO desorption (s ⁻¹)	O ₂ desorption (s ⁻¹)	CO oxidation (s ⁻¹)
HO	3.4×10^{15}	8.5×10^{15}	5.1×10^{12}
HT	2.3×10^{14}	3.5×10^{14}	6.3×10^{10}
FT	1.4×10^{14}	1.1×10^{12}	2.2×10^8
PES	4.2×10^{14}	1.3×10^{15}	3.3×10^{10}
experiments [14]	4×10^{15}	6.9×10^{13}	-----

Jørgensen and Grönbeck [9] also calculated the turnover frequency with the different models and found them to be highest for the HO model, lowest for the FT model, and in the middle for the PES and HT models, which match very closely. The temperature at which CO oxidation is initiated, or the light-off temperature, at different pressures calculated by the HT model match the PES model, within 6 K, and experiments, within 45 K, over a broad range of pressures. The coverage of CO and O on the surface are similar when represented by the HT and PES models, but the HT model tends to skew slightly towards the FT model.

Conclusions

The hindered translator and hindered rotor model has been shown to give entropies that match experimental results better than harmonic oscillator entropies for close-shelled molecules on Pt(111). The hindered translator model has also been shown to be better than the harmonic oscillator approximation when the potential energy well is flatter, such as for bridge adsorbed monatomic species and monatomic

adsorbates in hollow sites with low translational energy barriers, but worse when the potential energy well is steeper, such as monatomic adsorbates in hollow sites with high translational energy barriers. The choice of translational entropy model was shown to significantly affect the reaction kinetics by altering the turnover frequency, coverages, and light-off temperature and the hindered translator model was shown to perform very well when modeling CO oxidation on Pt(111). The hindered translator model skews towards the free translator model when calculating free energies, entropies, turnover frequencies, and coverages, as determined by comparison to the potential energy sampling method. While the initial results of using the hindered translator in a microkinetic analysis is promising, a larger reaction scheme with more varied types of adsorbates is needed.

Code for Atomic Simulation Environment

Atomic Simulation Environment (ASE) was initially created by Bahn and Jacobsen at the Technical University of Denmark [10] and has since been improved by many [11]. ASE contains a class called `HinderedThermo` that allows a user to calculate the thermodynamic quantities of their system. The code for ASE supports models for an ideal gas, a hindered translator / hindered rotor, a harmonic oscillator, and a crystalline solid. For the hindered translator / hindered rotor model, a user can get the internal energy, zero point energy, entropy, and Helmholtz free energy. Described here is the documentation, code, and an example for modeling a hindered adsorbate.

Documentation

The hindered translator / hindered rotor model bridges the gap between the 2D gas (i.e. free translator / free rotor) and the 2D lattice gas (i.e. harmonic oscillator). For an adsorbate containing N atoms, two degrees of freedom are treated as hindered translations in the two directions parallel to the surface, one degree of freedom is treated as a hindered rotation about the axis perpendicular to the surface, and the remaining $3N-3$ degrees of freedom are treated as vibrations. The `HinderedThermo` class supports the calculation of internal energy, entropy, free energy, and zero point

energy (included in the internal energy). All of the thermodynamic properties calculated here are at the standard state surface concentration (defined here such that a 2D ideal gas at that concentration has 2/3 the translational entropy of a 3D ideal gas at 1 bar pressure, so that $\theta^0 = 0.012$ at 298 K for a surface with 10^{15} sites/cm²). This class returns the Helmholtz free energy; if the user assumes that the pV term (in $G = U + pV - TS$) is zero then this free energy can also be interpreted as the Gibbs free energy. This class depends on the user defined translation barrier (`trans_barrier_energy`) and rotational barrier (`rot_barrier_energy`) for the adsorbate to move on the surface in order to calculate the translational and rotational degrees of freedom. To calculate the vibrational degrees of freedom, all $3N$ vibrational energies must be supplied in the `vib_energies` list and the $3N-3$ largest vibrational energies are used to calculate the vibrational contribution; this is a list as can be generated with the `.get_energies()` method of `ase.vibrations.Vibrations`. The class `HinderedThermo` has the interface described below.

Code

```
class HinderedThermo(ThermoChem):
    """Class for calculating thermodynamic properties in the
    hindered translator and hindered rotor model where all but
    three degrees of freedom are treated as harmonic
    vibrations, two are treated as hindered translations, and
    one is treated as a hindered rotation.

    Inputs:

    vib_energies : list
        a list of all the vibrational energies of the
        adsorbate (e.g., from
        ase.vibrations.Vibrations.get_energies). The number of
        energies should match the number of degrees of freedom
        of the adsorbate; i.e.,  $3*n$ , where  $n$  is the number of
        atoms. Note that this class does not check that the
        user has supplied the correct number of energies.
        Units of energies are eV.
    trans_barrier_energy : float
        the translational energy barrier in eV. This is the
        barrier for an adsorbate to diffuse on the surface.
    rot_barrier_energy : float
        the rotational energy barrier in eV. This is the
```

```

        barrier for an adsorbate to rotate about an axis
        perpendicular to the surface.
sitedensity : float
    density of surface sites in cm^-2
rotationalminima : integer
    the number of equivalent minima for an adsorbate's
    full rotation. For example, 6 for an adsorbate on an
    fcc(111) top site
potentialenergy : float
    the potential energy in eV (e.g., from
    atoms.get_potential_energy) (in potential energy is
    unspecified, then the methods of this class can be
    interpreted as the energy corrections)
mass : float
    the mass of the adsorbate in amu (if mass is
    unspecified, then it will be calculated from the atoms
    class)
inertia : float
    the reduced moment of inertia of the adsorbate in
    amu*Ang^-2 (if inertia is unspecified, then it will be
    calculated from the atoms class)
atoms : an ASE atoms object
    used to calculate rotational moments of inertia and
    molecular mass
symmetrynumber : integer
    symmetry number of the adsorbate. This is the number
    of symmetric arms of the adsorbate and depends upon
    how it is bound to the surface. For example, propane
    bound through its end carbon has a symmetry number of 1
    but propane bound through its middle carbon has a
    symmetry number of 2. (if symmetrynumber is
    unspecified, then the default is 1)
"""

def __init__(self, vib_energies, trans_barrier_energy,
             rot_barrier_energy, sitedensity, rotationalminima,
             potentialenergy=0, mass=None, inertia=None,
             atoms=None, symmetrynumber=1):
    self.vib_energies = sorted(
        vib_energies, reverse=True)[:3]
    self.trans_barrier_energy = trans_barrier_energy *
        units._e
    self.area = 1. / sitedensity / 100.0**2
    self.rotationalminima = rotationalminima
    self.potentialenergy = potentialenergy
    self.atoms = atoms
    self.symmetry = symmetrynumber

    if (mass or atoms) and (inertia or atoms):
        if mass:
            self.mass = mass * units._amu
        elif atoms:

```

```

        self.mass = (np.sum(atoms.get_masses()) *
                    units._amu)
    in inertia:
        self.inertia = (inertia * units._amu /
                       units.m**2)
    elif atoms:
        self.inertia = (
            atoms.get_moments_of_inertia()[2] *
            units._amu / units.m**2)
    else:
        raise RuntimeError('Either mass and inertia of '
                           'adsorbate must be specified or atoms '
                           'must be specified.')

    # Make sure no imaginary frequencies remain.
    if sum(np.iscomplex(self.vib_energies)):
        raise ValueError('Imaginary frequencies are '
                        'present.')
    else:
        self.vib_energies = np.real(self.vib_energies)
        # clear +0.j

    # Calculate hindered translational and hindered
    # rotational frequencies
    self.freq_t = np.sqrt(self.trans_barrier_energy / (2 *
                                                       self.mass * self.area))
    self.freq_r = 1. / (2 * np.pi) * np.sqrt(
        self.rotationalminima**2 / (2 * self.inertia))

def get_internal_energy(self, temperature, verbose=True):
    """Returns the internal energy (including the zero
    point energy), in eV, in the hindered translator and
    hindered rotor model at a specific temperature (K)."""

    from scipy.special import iv

    self.verbose = verbose
    write = self._vprint
    fmt = '%-15s%13.3f eV'
    write('Internal energy components at T = %.2f K:' %
          temperature)
    write('=' * 31)

    U = 0.

    write(fmt % ('E_pot', self.potentialenergy))
    U += self.potentialenergy

    # Translational Energy
    T_t = units._k * temperature / (units._hplanck *
                                     self.freq_t)
    R_t = self.trans_barrier_energy / (units._hplanck *

```

```

        self.freq_t)
dU_t = 2 * (-1. / 2 - 1. / T_t / (2 + 16 * R_t) +
           R_t / 2 / T_t - R_t / 2 / T_t *
           iv(1, R_t / 2 / T_t) / iv(0, R_t / 2 / T_t) +
           1. / T_t / (np.exp(1. / T_t) - 1))
dU_t *= units.kB * temperature
write(fmt % ('E_trans', dU_t))
U += dU_t

# Rotational Energy
T_r = units._k * temperature / (units._hplanck *
                                self.freq_r)
R_r = self.rot_barrier_energy / (units._hplanck *
                                self.freq_r)
dU_r = (-1. / 2 - 1. / T_r / (2 + 16 * R_r) + R_r /
        2 / T_r - R_r / 2 / T_r * iv(1, R_r / 2 /
        T_r) / iv(0, R_r / 2 / T_r) + 1. / T_r /
        (np.exp(1. / T_r) - 1))
dU_r *= units.kB * temperature
write(fmt % ('E_rot', dU_r))
U += dU_r

# Vibrational Energy
dU_v = self._vibrational_energy_contribution(
        temperature)
write(fmt % ('E_vib', dU_v))
U += dU_v

# Zero Point Energy
dU_zpe = self.get_zero_point_energy()
write(fmt % ('E_ZPE', dU_zpe))
U += dU_zpe

write('-' * 31)
write(fmt % ('U', U))
write('=' * 31)
return U

def get_zero_point_energy(self, verbose=True):
    """Returns the zero point energy, in eV, in the
    hindered translator and hindered rotor model"""

    zpe_t = 2 * (1. / 2 * self.freq_t * units._hplanck /
                units._e)
    zpe_r = (1. / 2 * self.freq_r * units._hplanck /
            units._e)
    zpe_v = self.get_ZPE_correction()
    zpe = zpe_t + zpe_r + zpe_v
    return zpe

def get_entropy(self, temperature, verbose=True):
    """Returns the entropy, in eV/K, in the hindered

```

```

translator and hindered rotor model at a specific
temperature (K)."""

from scipy.special import iv

self.verbose = verbose
write = self._vprint
fmt = '%-15s%13.7f eV/K%13.3f eV'
write('Entropy components at T = %.2f K:'
      %temperature)
write('=' * 49)
write('%15s%13s      %13s' % ('', 'S', 'T*S'))

S = 0.

# Translational Entropy
T_t = units._k * temperature / (units._hplanck *
                                self.freq_t)
R_t = self.trans_barrier_energy / (units._hplanck *
                                    self.freq_t)
S_t = 2 * (-1. / 2 + 1. / 2 * np.log(np.pi * R_t /
                                     T_t) - R_t / 2 / T_t * iv(1, R_t / 2 / T_t) /
          iv(0, R_t / 2 / T_t) + np.log(iv(0, R_t / 2 /
          T_t)) + 1. / T_t / (np.exp(-1. / T_t)))
S_t *= units.kB
write(fmt % ('S_trans', S_t, S_t * temperature))
S += S_t

# Rotational Energy
T_r = units._k * temperature / (units._hplanck *
                                self.freq_r)
R_r = self.rot_barrier_energy / (units._hplanck *
                                  self.freq_r)
S_r = (-1. / 2 + 1. / 2 * np.log(np.pi * R_r / T_r) -
       np.log(self.symmetry) -
       R_r / 2 / T_r * iv(1, R_r / 2 / T_r) /
       iv(0, R_r / 2 / T_r) + np.log(iv(0, R_r / 2 /
       T_r)) + 1. / T_r / (np.exp(-1. / T_r) - 1) -
       np.log(1 - np.exp(-1. / T_r)))
S_r *= units.kB
write(fmt % ('S_rot', S_r, S_r * temperature))
S += S_r

# Vibrational Energy
S_v = self._vibrational_entropy_contribution(
      temperature)
write(fmt % ('S_vib', S_v, S_v * temperature))
S += S_v

# Concentration Related Entropy
N_over_A = np.exp(1. / 3) * (10.0**5 / (units._k *
      temperature))**(2. / 3)

```

```

S_c = 1 - np.log(N_over_A) - np.log(self.area)
S_c *= units.kB
write(fmt % ('S_con', S_c, S_c * temperature))
S += S_c

write('-' * 49)
write(fmt % ('S', S, S * temperature))
write('=' * 49)
return S

def get_helmholts_energy(self, temperature, verbose=True):
    """Returns the Helmholtz free energy, in eV, in the
    hindered translator and hindered rotor model at a
    specific temperature (K)."""

    self.verbose = True
    write = self._vprint

    U = self.get_internal_energy(temperature,
                                  verbose=verbose)
    write('')
    S = self.get_entropy(temperature, verbose=verbose)
    F = U - temperature * S

    write('')
    write('Free energy components at T = %.2f K:'
          % temperature)
    write('=' * 23)
    fmt = '%5s%15.3f eV'
    write(fmt % ('U', U))
    write(fmt % ('-T*S', -temperature * S))
    write('-' * 23)
    write(fmt % ('F', F))
    write('=' * 23)
    return F

```

Example

The `HinderedThermo` class would generally be called after an energy optimization and a vibrational analysis. The user needs to supply certain parameters, such as the vibrational energies, translational energy barrier, rotational energy barrier, surface site density, number of equivalent minima in a full rotation, and the number of symmetric arms of the adsorbate as it rotates on the surface. The user also needs to supply either the mass of the adsorbate and the reduced moment of inertia of the adsorbate as it rotates on the surface or the user can supply the atoms object from

which the mass and an approximate reduced moment of inertia may be determined.

An example for ethane on a platinum (111) surface is:

```

from ase.thermochemistry import HinderedThermo
from numpy import array

vibs = array([3049.060670,
              3040.796863,
              3001.661338,
              2997.961647,
              2866.153162,
              2750.855460,
              1436.792655,
              1431.413595,
              1415.952186,
              1395.726300,
              1358.412432,
              1335.922737,
              1167.009954,
              1142.126116,
              1013.918680,
              803.400098,
              783.026031,
              310.448278,
              136.112935,
              112.939853,
              103.926392,
              77.262869,
              60.278004,
              25.825447])

vib_energies = vibs / 8065.54429 # convert to eV from cm^-1
trans_barrier_energy = 0.049313 # eV
rot_barrier_energy = 0.017675 # eV
sitedensity = 1.5e15 # cm^-2
rotationalminima = 6
symmetrynumber = 1
mass = 30.07 # amu
inertia = 73.149 # amu Ang^-2

thermo = HinderedThermo(
    vib_energies=vib_energies,
    trans_barrier_energy=trans_barrier_energy,
    rot_barrier_energy=rot_barrier_energy,
    sitedensity=sitedensity,
    rotationalminima=rotationalminima,
    symmetrynumber=symmetrynumber,
    mass=mass,
    inertia=inertia)

F = thermo.get_helmholtz_energy(temperature=298.15)

```

This will give the thermodynamic summary output:

Internal energy components at T = 298.15 K:

```

=====
E_pot           0.000 eV
E_trans        0.049 eV
E_rot          0.018 eV
E_vib          0.076 eV
E_ZPE          1.969 eV
-----
U               2.112 eV
=====

```

Entropy components at T = 298.15 K:

```

=====
                        S                T*S
S_trans           0.0005074 eV/K        0.151 eV
S_rot             0.0002287 eV/K        0.068 eV
S_vib            0.0005004 eV/K        0.149 eV
S_con            0.0005044 eV/K        0.150 eV
-----
S                 0.0017409 eV/K        0.519 eV
=====

```

Free energy components at T = 298.15 K:

```

=====
U               2.112 eV
-T*S           -0.519 eV
-----
F               1.593 eV
=====

```

Code for Catalysis Microkinetic Analysis Package

Catalysis Microkinetic Package (CatMAP) was created at Stanford University by AJ Medford and coworkers [12] as a way to automate solving a microkinetic model. The package calculates entropies from the partition function and uses the entropies to calculate rate constants or equilibrium constants. The thermodynamics module contains models for calculating the enthalpy and entropy for species such as a harmonic adsorbate or a hindered adsorbate. Both the harmonic adsorbate and the hindered adsorbate code in CatMAP utilize the ASE code to calculate the thermodynamic properties. The hindered adsorbate code can calculate the zero-point

energy, enthalpy, entropy, and free energy. The documentation and code to model a hindered adsorbate in CatMAP is shown here.

Documentation

`hindered_adsorbate` is a mode for correcting the energies of adsorbed species. It relies on ASE's thermochemistry package `HinderedThermo`, user-provided vibrational frequencies, and a dictionary of hindered adsorbate parameters,

`hindered_ads_params`, which stores [barrierT, barrierR, site_density, rotational_minima, mass, inertia, symmetry_number] values for each adsorbate species key. You can provide your own parameters by adding something like the following to your `.mkm` file:

```
hindered_ads_params = {
    'CH4_s':[0.006, 0.0008, 1.5e15, 6, None, None, 1],
    'C2H6_s':[0.049, 0.018, 1.5e15, 6, 30.07, 73.15, 1],
}
```

and so on for each adsorbed species in your system.

Code

```
def hindered_adsorbate(self):
    """Calculate the thermal correction to the free energy of
    an adsorbate in the hindered translator and hindered rotor
    model using the HinderedThermo class in
    ase thermochemistry along with the molecular structures in
    ase.data.molecules. Requires ase version 3.12.0 or
    greater.

    adsorbate_names = the chemical formulas of the adsorbates
    of interest.
    freq_dict = dictionary of vibrational frequencies for each
    adsorbate of interest. Vibrational frequencies should
    be in eV. The dictionary should be in the form
    freq_dict[ads_name] = [freq1, freq2, ...]
    hindered_ads_params = dictionary containing for each
    adsorbate:
    [0] = translational energy barrier in eV (barrier for
    the adsorbate to diffuse on the surface)
    [1] = rotational energy barrier in eV (barrier for the
    adsorbate to rotate about an axis perpendicular
    to the surface)
```

```

[2] = surface site density in cm^-2
[3] = number of equivalent minima in full adsorbate
      rotation
[4] = mass of the adsorbate in amu (can be unspecified
      by putting None, in which case mass will attempt
      to be calculated from the ase atoms class)
[5] = reduced moment of inertia of the adsorbate in
      Amu*Ang^-2 (can be unspecified by putting None,
      in which case inertia will attempt to be
      calculated from the ase atoms class)
[6] = symmetry number of the adsorbate (number of
      symmetric arms of the adsorbate which depends
      upon how it is bound to the surface. For
      example, propane bound through its end carbon
      has a symmetry number of 1 but propane bound
      through its middle carbon has a symmetry number
      of 2. For single atom adsorbates such as O* the
      symmetry number is 1.)
The dictionary should be of the form
hindered_ads_params[ads_name] = [barrierT, barrierR,
site_density, rotational_minima, mass, inertia,
symmetry_number]
atoms_dict = dictionary of ase atoms object to use for
calculating mass and rotational inertia. If none is
specified then the function will look in
ase.data.molecules. Can be omitted if both mass and
rotational inertia are specified in
hindered_ads_params.
"""

adsorbate_names = self.adsorbate_names +
                  self.transition_state_names
temperature = float(self.temperature)
freq_dict = self.frequency_dict
ads_params_dict = self.hindered_ads_params

thermo_dict = {}
if temperature == 0: temperature = 1e-99

ase_atoms_dict = {}
for ads in self.adsorbate:
    atom_name = ads.rsplit('_',1)[0]
    try:
        ase_atoms_dict[ads] = molecule(atom_name)
    except (NotImplementedError,KeyError)
        pass
ase_atoms_dict.update(self.atoms_dict)
self.atoms_dict = ase_atoms_dict
atoms_dict = self.atoms_dict

avg_TS = []

```

```

self._freq_cutoffs = {}

for ads in adsorbate_names:
    if '-' in ads and (freq_dict[ads] in [None, [], ()] or
        ads not in ads_param_dict):
        frequencies = freq_dict[ads]
    else:
        raise IndexError('Missing vibrational frequencies
            for '+ads')
    if self.max_entropy_per_mode:
        if temperature in self._freq_cutoffs:
            nu_min = self._freq_cutoffs[temperature]
        else:
            kB_multiplier = float(
                self.max_entropy_per_mode/self._kB)
            nu_min = self.get_frequency_cutoff(
                kB_multiplier, float(temperature))
            nu_min /= 1000.
            self._freq_cutoffs[temperature] = nu_min
        frequencies = [max(nu, nu_min) for nu in frequencies]

    #get all other parameters or throw error
    if ads in ads_params_dict:
        apars = ads_params_dict[ads]
    else:
        raise IndexError('Missing hindered_ads_params '
            'for '+ads)
    barrierT = apars[0]
    barrierR = apars[1]
    sitedensity = apars[2]
    rotationalminima = apars[3]
    mass = apars[4]
    inertia = apars[5]
    symmetrynumber = apars[6]
    try:
        atoms = atoms_dict[ads]
    except:
        atoms = {}
    if not ((mass and inertia) or atoms):
        if '-' in ads:
            avg_TS.append(ads)
            break
        else:
            raise IndexError('Missing either mass and '
                'inertia of '+ads+' or atoms object '
                'for '+ads)

    therm = HinderedThermo(
        frequencies, barrierT, barrierR, sitedensity,
        rotationalminima, mass=mass, inertia=inertia,
        atoms=atoms, symmetrynumber=symmetrynumber)

```

```

free_energy = therm.get_helmholtz_energy(
    temperature, verbose=False)
ZPE = therm.get_zero_point_energy(verbose=False)
dS = therm.get_entropy(temperature, verbose=False)
dH = therm.get_internal_energy(
    temperature, verbose=False) - ZPE
self._zpe_dict[ads] = ZPE
self._enthalpy_dict[ads] = dH
self._entropy_dict[ads] = dS
thermo_dict[ads] = free_energy #use thermodynamic
#state from ase.thermochemistry to calculate thermal
#corrections.

return thermo_dict

```

References

- [1] J.A. Dumesic, *The Microkinetics of Heterogeneous Catalysis*, American Chemical Society, Washington, DC, 1993.
- [2] A.H. Motagamwala, J.A. Dumesic, Analysis of reaction schemes using maximum rates of constituent steps, *Proceedings of the National Academy of Sciences of the United States of America*, 113 (2016) E2879-E2888.
- [3] C.T. Campbell, J.R.V. Sellers, The Entropies of Adsorbed Molecules, *Journal of the American Chemical Society*, 134 (2012) 18109-18115.
- [4] C.T. Campbell, L. Arnadottir, J.R.V. Sellers, Kinetic Prefactors of Reactions on Solid Surfaces, *Zeitschrift Fur Physikalische Chemie-International Journal of Research in Physical Chemistry & Chemical Physics*, 227 (2013) 1435-1454.
- [5] M. Jørgensen, H. Grönbeck, First-Principles Microkinetic Modeling of Methane Oxidation over Pd(100) and Pd(111), *ACS Catalysis*, 6 (2016) 6730-6738.
- [6] A. Budi, S.L.S. Stipp, M.P. Andersson, Calculation of Entropy of Adsorption for Small Molecules on Mineral Surfaces, *The Journal of Physical Chemistry C*, 122 (2018) 8236-8243.
- [7] L.H. Sprowl, C.T. Campbell, L. Arnadottir, Hindered Translator and Hindered Rotor Models for Adsorbates: Partition Functions and Entropies, *Journal of Physical Chemistry C*, 120 (2016) 9719-9731.
- [8] A. Bajpai, P. Mehta, K. Frey, A.M. Lehmer, W.F. Schneider, Benchmark First-Principles Calculations of Adsorbate Free Energies, *ACS Catalysis*, 8 (2018) 1945-1954.
- [9] M. Jørgensen, H. Grönbeck, Adsorbate Entropies with Complete Potential Energy Sampling in Microkinetic Modeling, *Journal of Physical Chemistry C*, 121 (2017) 7199-7207.

- [10] S.R. Bahn, K.W. Jacobsen, An Object-Oriented Scripting Interface to a Legacy Electronic Structure Code, *Computing in Science & Engineering*, 4 (2002) 56-66.
- [11] A.H. Larsen, J.J. Mortensen, J. Blomqvist, I.E. Castelli, R. Christensen, M. Dulak, J. Friis, M.N. Groves, B. Hammer, C. Hargus, E.D. Hermes, P.C. Jennings, P.B. Jensen, J. Kermode, J.R. Kitchin, E.L. Kolsbjerg, J. Kubal, K. Kaasbjerg, S. Lysgaard, J.B. Maronsson, T. Maxson, T. Olsen, L. Pastewka, A. Peterson, C. Rostgaard, J. Schiøtz, O. Schütt, M. Strange, K.S. Thygesen, T. Vegge, L. Vilhelmsen, M. Walter, Z.H. Zeng, K.W. Jacobsen, The Atomic Simulation Environment-A Python Library for Working with Atoms, *Journal of Physics-Condensed Matter*, 29 (2017).
- [12] A.J. Medford, C. Shi, M.J. Hoffmann, A.C. Lausche, S.R. Fitzgibbon, T. Bligaard, J.K. Nørskov, CatMAP: A Software Package for Descriptor-Based Microkinetic Mapping of Catalytic Trends, *Catalysis Letters*, 145 (2015) 794-807.
- [13] S. Conti, M. Cecchini, Modeling the adsorption equilibrium of small-molecule gases on graphene: effect of the volume to surface ratio, *Physical Chemistry Chemical Physics*, 20 (2018) 9770-9779.
- [14] C.T. Campbell, G. Ertl, H. Kuipers, J. Segner, A Molecular-Beam Investigation of the Interactions of CO with a Pt(111) Surface, *Surface Science*, 107 (1981) 207-219.

CHAPTER 5

FIRST-PRINCIPLES STUDY OF THE PRODUCTS OF CO₂
DISSOCIATION ON NICKEL-BASED ALLOYS: TRENDS IN
ENERGETICS WITH ALLOYING ELEMENT

Lynza H. Sprowl¹, Benjamin M. Adam^{2,3}, Julie D. Tucker², Líney Árnadóttir^{1,*}

¹ School of Chemical, Biological and Environmental Engineering
Oregon State University, Corvallis, OR 97331, USA

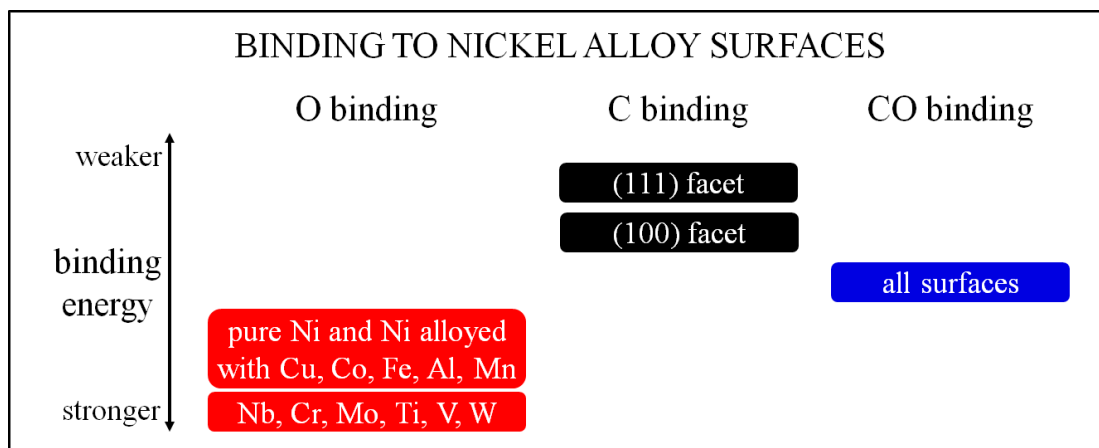
² School of Mechanical, Industrial and Manufacturing Engineering
Oregon State University, Corvallis, OR 97331, USA

³ Department of Mechanical and Materials Engineering
Portland State University, Portland, OR 97201, USA

* Corresponding author

Reproduced in part from a submission to *Surface Science*.

Abstract



Oxidation and corrosion of nickel and Ni-based alloys are a problem for many industrial applications, such as power plants that use supercritical CO₂ as the working fluid. In supercritical CO₂ environments, CO₂ dissociates on the surface forming adsorbed CO and O, which can oxidize the surface. The adsorbed CO can further breakdown via direct CO dissociation or via the Boudouard reaction to form adsorbed C, which can in turn carburize the surface. Understanding how the adsorbed species interact with different Ni-based alloys can help guide the design of future alloys. The interactions of adsorbed O, C, and CO on the (100) and (111) facets of pure Ni and Ni individually alloyed with Al, Co, Cr, Cu, Fe, Mn, Mo, Nb, Ti, V, and W are examined using density functional theory. We find that the binding of CO is energetically similar across all alloy surfaces and both facets, while O binding varies across the different alloy surfaces and C binding varies between the different facets. The binding of O is weaker on pure Ni and Ni alloyed with Cu, Co, Fe, Al, or Mn and stronger on Ni alloyed with Nb, Cr, Mo, Ti, V, or W, while the binding of C is weaker on the (111) facet than the (100) facet. The difference in the binding energies of the adsorbates across the different alloy surfaces is due mainly to the ensemble effect, rather than the ligand effect. The thermodynamics of CO breakdown are also studied and we find that the breakdown of CO via direct CO dissociation is endothermic on the (111) facet and exothermic on the (100) facet, with the alloy surfaces that bind O strongly having the most exothermic reaction energies. The breakdown of CO via the

Boudouard reaction has similar reaction energies across the different alloy surfaces of a single facet and is endothermic on both facets, with the (111) facet being most endothermic. This comprehensive study presents a summary of the current literature as well as a well-rounded view of the products of CO₂ breakdown on Ni surfaces alloyed with the most common alloying elements used in industrial applications.

Introduction

Nickel-based alloys are commonly used in industrial applications as structural materials and as heterogeneous catalysts. In catalysis, Ni-based alloys are common in applications such as the oxidation of hydrocarbon fuels in solid-oxide fuel cells (SOFC) [1-3] and in the catalytic dry reforming of CH₄ with CO₂ to make syngas [4, 5]. Ni-based alloys are also widely used as structural materials in industrial applications such as heat exchangers, pipework, combustion cans, and engine blades due to their corrosion-resistance, high-strength, and high-temperature properties [6, 7]. An emerging application for Ni-based alloys is in supercritical carbon dioxide (sCO₂) power production cycles. Compared to conventional steam power production cycles, sCO₂ cycles offer an improved plant efficiency due to less compressive work because of higher CO₂ densities. Other advantages of sCO₂ cycles include lower cost, reduced emissions, fewer and smaller energy conversion components, and a simpler cycle layout [8, 9]. A major limitation to implementing this step-changing technology is the identification and development of high-strength, corrosion-resistant materials for high temperature (650-800°C) power plant components. Herein, we use density functional theory to study the surface chemistry of a dozen Ni-based alloys that are promising materials for such power plants, and discover trends in the thermodynamic stabilities of the surface species, which give insights into how to improve the long-term stability of these materials.

There are many commercially available Ni-based alloys and superalloys that are currently being considered for sCO₂ applications such as 740H, 282, 230, 625, 214, 224, and C276 [9-14]. In these Ni-based alloys, the highest concentration alloying elements are Cr, Fe, Co, Mo, W, Al, Nb, Ti, Mn, Si, Cu, C, and V, which are taken as the starting point for the Ni-based alloy surfaces studied herein. All metallic

elements, which excludes Si and C, are included in this study giving twelve different alloy surfaces.

The initial step in the degradation of Ni-based alloys in sCO₂ conditions is expected to be through the dissociation of CO₂ to make adsorbed CO plus O (CO_{ads} + O_{ads}). Computational results [15] have found CO₂ to dissociate on Ni(100), while experimental results [16] have observed CO₂ to dissociate on Ni(100), but not on Ni(111). However, we find CO₂ dissociation to be quite exothermic on both facets with a reaction energy of -1.38 eV on Ni(100) and -1.07 eV on Ni(111), such that CO and/or O could diffuse to the (111) facet after dissociation on the (100) facet. This is followed by carbon deposition from CO_{ads} dissociation into C_{ads} + O_{ads} or from the Boudouard reaction where two CO_{ads} react to form C_{ads} + CO_{2,gas}. Deposition of O on the surface leads to oxidation of the surface and the formation of metal oxides while deposition of C on the surface leads to carburization of the surfaces and the formation of metal carbides, which change the chemistry of the surface and eventually the properties of the bulk metal.

We show that alloying Ni with other elements affects the CO breakdown reactions, just as it has been shown to affect other reactions such as water gas shift [17] and methane reforming [18]. Herein we study the adsorbed products of CO₂ dissociation (O_{ads}, C_{ads}, and CO_{ads}) and uncover how their stabilities depend on the nature of the alloying element used to make the Ni-based alloy. We also study the thermodynamics of the CO dissociation and Boudouard reactions to understand the most favorable CO breakdown pathways. The kinetics of the reactions are not studied because of the high power plant temperatures, which would cause the reactions to be under thermodynamic control instead of kinetic control, and because the reaction kinetics on the different alloy surfaces likely scale with the reaction thermodynamics, as given by the Brønsted-Evans-Polanyi relations that relate the activation energy barrier to the reaction energy for a given family of reactions [19-21].

The adsorption of O [22-25] and CO [25-30] has been studied extensively on the low-index facets of pure Ni surfaces. More recently, studies have included Ni-based alloys looking at the adsorption of O, C, and CO on the (111) facet [1-7, 31, 32], however the (100) facet [33, 34] is less studied. In order to develop new Ni-based

alloys, it is essential to understand the fundamental interactions of the corrosive species with the surface and the thermodynamics of the reactions that lead to the corrosive species. Herein we focus on the Ni(100) and Ni(111) facets with Al, Co, Cr, Cu, Fe, Mn, Mo, Nb, Ti, V, or W alloying elements and examine their interactions with adsorbed O, C, and CO. To better understand the direct interaction between the adsorbate and the alloying element, a low concentration alloy is modeled by replacing a single Ni surface atom with the alloying element, leading to a mole fraction of 1/9 in the surface layer but only 1/63 and 1/54 in the (100) and (111) simulation slabs, respectively. Binding energies and binding sites for all adsorbates, ligand and ensemble effects of the alloying atom, and CO dissociation and Boudouard reaction energies are determined on all facets and surfaces.

Methods

Computational Details

All results are calculated using density functional theory (DFT) via the Vienna Ab-initio Simulation Package (VASP) [35-38], with some of the calculations run on the Extreme Science and Engineering Discovery Environment (XSEDE) [39]. Electronic structures are calculated for the adsorption of one C, O, or CO adsorbate on the (100) and (111) facets of Ni-based alloys. A $p(3 \times 3)$ unit cell is used to represent the 12 Å thick surface slabs, containing 7 layers for the (100) facet and 6 layers for the (111) facet, with 20 Å of vacuum between slabs. The top 4 metal layers and the adsorbate are allowed to relax while the bottom 3 layers for the (100) facet and 2 layers for the (111) facet are held fixed. Atomic Simulation Environment (ASE) was used to create the initial simulation cells [40].

The exchange correlation potential and energy is described by the generalized gradient approximation (GGA) as defined by the Perdew-Burke-Ernzerhof (PBE) functional [41, 42], and the projector augmented wave (PAW) method is used to represent the core electrons [43, 44]. Spin polarization and magnetization effects are included. Plane-wave calculations are employed with a kinetic energy cutoff of 400 eV for the Kohn-Sham orbitals and the surface Brillouin zone is sampled using a Monkhorst-Pack grid with $5 \times 5 \times 1$ k points. Increasing the energy cutoff to 500 eV

changes the binding energies of O, C, and CO on Ni(100) by 3 meV, 10 meV, and 3 meV and on Ni(111) by 8 meV, 8 meV, and 1 meV, respectively. Increasing the number of k points to 7x7x1 changes the O, C, and CO binding energies on Ni(100) by 0.04 eV, 0.02 eV, and 0.002 eV and on Ni(111) by 0.03 eV, 0.02 eV, and 0.01 eV, respectively. All calculations for binding energies are relaxed until the forces are converged below 0.01 eV/Å. The calculated lattice constant for Ni is 3.52 Å, in agreement with the experimental value of 3.52 Å [45].

Density of states calculations are performed using 15x15x1 k points to sample the Brillouin zone. Increasing to 19x19x1 k points changes the d-band center of the pure Ni surface by 0.04 eV for the (100) facet and 0.03 eV for the (111) facet. The electron density is converged until the energy is below 10^{-6} eV for the clean surfaces. Only the top one surface layer is considered when calculating the d-band center of each Ni-based alloy surface. Bader charge calculations [46-49] are also performed on the clean alloy surfaces with 5x5x1 k points and an energy cutoff of 500 eV.

Surface Models

The 3x3 surfaces bind one adsorbed species, corresponding to a 1/9 monolayer adsorbate coverage. For the alloy surfaces, one of the Ni atoms in the top layer is exchanged for the alloying metal atom (Ti, V, Nb, Cr, Mo, W, Mn, Fe, Co, Cu, or Al), setting the alloy surface concentration at 1/9. Figure 5.1 shows the different adsorption sites on the alloyed (100) and (111) facets. There are three unique hollow sites, three unique top sites, and four unique bridge sites on the (100) facet and three unique hcp hollow sites, three unique fcc hollow sites, three unique top sites, and four unique bridge sites on the (111) facet. The numbers in Figure 5.1 represent the unique binding locations for each site and increase moving away from the alloying atom. Alloy-rich sites have the adsorbate adjacent to the alloying atom and include the top-1, hollow-1, hcp-1, fcc-1, and bridge-1 sites. Ni-rich sites correspond to sites in which the adsorbate is bound to only Ni atoms and include all remaining sites.

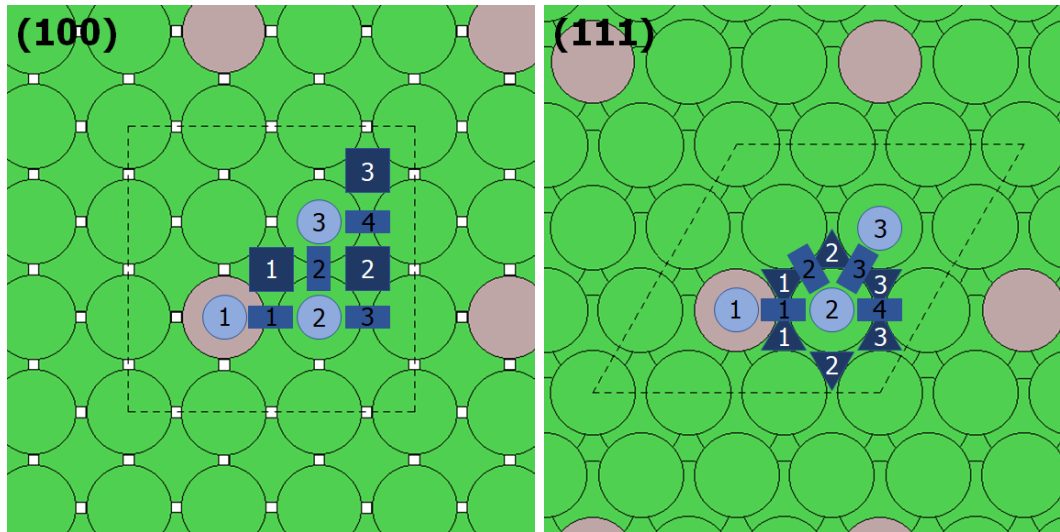


Figure 5.1 Unique binding sites on the (100) and (111) facets. Light blue circles represent top sites, medium blue rectangles represent bridge sites, dark blue squares represent (100) hollow sites, dark blue up-pointing triangles represent (111) hcp hollow sites, and dark blue down-pointing triangles represent (111) fcc hollow sites. The numbers increase moving away from the alloying atom and label the unique binding locations for each site.

Binding energies of O, C, and CO at each unique site are calculated to determine the most stable binding location for each adsorbate on every alloy surface. The binding energy is defined as

$$E_{\text{bind}} = E_{\text{surf+ads}} - E_{\text{surf}} - E_{\text{ref}} \quad (5.1)$$

where $E_{\text{surf+ads}}$ is the total energy of the surface and adsorbate system, E_{surf} is the energy of the clean surface, and E_{ref} is the adsorbate reference energy. The reference energy is the energy of $1/2 \text{ O}_2$ in vacuum, one graphite atom, or CO in vacuum for the O, C, or CO adsorbate, respectively. With this notation, a negative E_{bind} value indicates a release of energy upon adsorption and a positive E_{bind} value represents an increase in energy upon adsorption.

Binding energy differences are also reported for adsorbates on the different Ni-based alloy surfaces relative to the pure Ni surface when the adsorbate is in its most stable adsorption site on each surface. The difference in binding energy is calculated as

$$\Delta E_{\text{bind}} = E_{\text{bind}}^{\text{alloy}} - E_{\text{bind}}^{\text{Ni}} = E_{\text{surf+ads}}^{\text{alloy}} - E_{\text{surf}}^{\text{alloy}} - E_{\text{surf+ads}}^{\text{Ni}} + E_{\text{surf}}^{\text{Ni}} \quad (5.2)$$

where the superscripts indicate the alloy surface or the pure Ni surface. In this notation, a negative ΔE_{bind} value indicates that the adsorbate binds stronger to the alloy surface than the pure Ni surface and a positive ΔE_{bind} value signifies that the adsorbate binds weaker to the alloy surface than the pure Ni surface. The advantage of calculating the binding energy difference is that it is independent of the choice of reference species, which is useful when comparing to other literature values.

The binding energies of the reactants and the products in the CO dissociation reaction ($\text{CO} \rightarrow \text{C} + \text{O}$) and the Boudouard reaction ($2\text{CO} \rightarrow \text{C} + \text{CO}_2$) are calculated relative to CO in the gas phase. The binding energy of a single CO reactant follows Equation 5.1 and is calculated as

$$E_{\text{bind,CO}} = E_{\text{surf+CO}} - E_{\text{surf}} - E_{\text{CO}} \quad (5.3)$$

where E_{CO} is the energy of CO in vacuum. The binding energy of the products of CO dissociation, C+O, is calculated as

$$E_{\text{bind,C+O}} = E_{\text{surf+C}} + E_{\text{surf+O}} - 2E_{\text{surf}} - E_{\text{CO}} \quad (5.4)$$

making the overall CO dissociation reaction energy

$$E_{\text{rxn,COdiss}} = E_{\text{bind,C+O}} - E_{\text{bind,CO}} = E_{\text{surf+C}} + E_{\text{surf+O}} - E_{\text{surf+CO}} - E_{\text{surf}} \quad (5.5)$$

The binding energy of the Boudouard reaction products, C+CO₂, is calculated as

$$E_{\text{bind,C+CO}_2} = E_{\text{surf+C}} + E_{\text{CO}_2} - E_{\text{surf}} - 2E_{\text{CO}} \quad (5.6)$$

where E_{CO_2} is the energy of CO₂ in vacuum, making the overall Boudouard reaction energy

$$E_{\text{rxn,Boudouard}} = E_{\text{bind,C+CO}_2} - 2E_{\text{bind,CO}} = E_{\text{surf+C}} + E_{\text{CO}_2} + E_{\text{surf}} - 2E_{\text{surf+CO}} \quad (5.7)$$

A positive reaction energy, E_{rxn} , represents an endothermic reaction, with CO being the most energetically stable species, and a negative reaction energy represents an exothermic reaction, where $\text{C}+\text{O}$ for CO dissociation or $\text{C}+\text{CO}_2$ for the Boudouard reaction is energetically more favorable. Herein the adsorbates are assumed to be far apart and non-interacting.

Results and Discussion

The aim of this study is to understand the relative stabilities of CO_2 dissociation products on Ni-based alloy surfaces. The binding energies reported below reveal that the dissociation of CO_2 gas on these alloy surfaces to produce $\text{CO}_{\text{ads}} + \text{O}_{\text{ads}}$ is quite exothermic, with a reaction energy of -1.38 eV on Ni(100) and -1.07 eV on Ni(111). This is in good agreement with a previous study that found the reaction to be exothermic by -1.00 eV on Ni(100) and -1.33 eV on Ni(111) [50]. Herein we focus on the relative energies of the CO_2 dissociation products (CO_{ads} and O_{ads}) and further CO reaction products (C_{ads}) which can be produced by either CO dissociation, $\text{CO} \rightarrow \text{C} + \text{O}$, or the Boudouard reaction, $2\text{CO} \rightarrow \text{C} + \text{CO}_2$, and analyze how these energies depend on the nature of the alloying element.

Oxygen Binding

The binding of O is most stable at a hollow site (-3.20 eV) and less stable at a bridge site (-2.50 eV) or a top site (-1.30 eV) on the Ni(100) facet. On the Ni(111) facet, O binds slightly stronger at an fcc hollow site (-2.91 eV) than an hcp hollow site (-2.80 eV) and weaker at a top site (-1.06 eV). The O binding energy at a bridge site on the (111) facet could not be determined. This is in good agreement with previous DFT studies that also found the hollow site on Ni(100) and the fcc site on Ni(111) to be the most stable binding sites for O [25, 50-52]. Experimentally, O is also found to be most stable at a four-fold hollow site on Ni(100) with a binding energy of -2.85 eV and at three-fold hollow sites on Ni(111) with a binding energy of -2.28 eV [23]. This is in good agreement with the results presented here, however non-hybrid DFT functionals, such as PBE, are well known to overbind chemisorbed systems [53, 54], so slightly stronger calculated binding energies are not surprising.

Comparing the two facets, O adsorbs 0.29 eV stronger on the (100) facet than on the (111) facet, in agreement with previous DFT studies that found O adsorption is stronger on Ni(100) than Ni(111) by 0.28 eV [51], 0.31 eV [50, 52], 0.32 eV [25], or 0.44 eV [55].

Replacing a Ni surface atom with an alloying atom changes the properties of the surface and influences the way O interacts with the surface, as shown in Table 5.1 by different binding energies and binding sites for adsorbed O. A complete list of O binding energies for all surfaces at different sites can be found in Tables 5.S1 and 5.S2 in the Supporting Information. The most stable binding site for O adsorption is adjacent to the alloying atom at the hollow-1 site and fcc-1 site on the (100) and (111) facets, respectively, for all Ni-based alloy surfaces except when the alloying element is Cu, Mo, or W. On the Cu alloy surface, O binds stronger at a Ni-rich hollow site than the hollow site adjacent to the Cu atom by 0.13 eV on the (100) facet and by 0.34 eV on the (111) facet. On both facets of the Mo and W alloy surfaces, O binds strongest at the top-1 site right above the alloying atom. On the Mo alloy surface, O is more stable at the top-1 site by 0.26 eV and 0.15 eV than the hollow-1 site on the (100) facet and the fcc-1 site on the (111) facet, respectively, which are the second most stable sites. O is not stable at the hollow-1 site on the (100) facet of the W alloy surface so a comparison cannot be made, however on the (111) facet O binds 0.21 eV stronger to the top-1 site compared to the fcc-1 site. The energetic favorability of O at top-1 sites can be explained by the stronger oxophilic nature of Mo and W.

Table 5.1 Effects of substituting an alloying atom for a single Ni surface atom on oxygen adsorption. Binding energy (eV) referenced to 1/2 O₂ in vacuum, binding energy difference relative to pure Ni (eV), and binding site for O adsorption on the (100) and (111) facets of Ni-based alloys at 1/9 ML coverage. For site locations, refer to Figure 5.1.

Alloying Atom	(100) facet			(111) facet		
	E _{bind}	ΔE _{bind}	site	E _{bind}	ΔE _{bind}	site
Ni (no alloy)	-3.20	0.00	hol	-2.91	0.00	fcc
Cu	-3.20	0.00	hol-2	-2.94	-0.03	fcc-2
Co	-3.25	-0.05	hol-1	-2.98	-0.07	fcc-1
Fe	-3.31	-0.11	hol-1	-3.05	-0.14	fcc-1
Al	-3.33	-0.13	hol-1	-3.12	-0.21	fcc-1
Mn	-3.39	-0.19	hol-1	-3.19	-0.28	fcc-1
Nb	-3.78	-0.58	hol-1	-3.67	-0.76	fcc-1
Cr	-3.81	-0.61	hol-1	-3.75	-0.84	fcc-1
Ti	-3.94	-0.74	hol-1	-3.80	-0.89	fcc-1
V	-3.97	-0.77	hol-1	-3.89	-0.98	fcc-1
Mo	-4.08	-0.88	top-1	-3.89	-0.98	top-1
W	-4.27	-1.07	top-1	-4.01	-1.10	top-1

All the alloying elements strengthen the O-surface interactions on both the (100) and (111) facets, shown by the negative ΔE_{bind} values in Table 5.1, except Ni(100) alloyed with Cu in which the O binding energy is not affected. The range over which an alloying element affects the binding energy of O on the surface is broad, with the largest increase being 1.07 eV and 1.10 eV for Ni alloying with W on the (100) and (111) facets, respectively. The order in which the alloying element increases the binding strength of O on the Ni-based alloy surfaces is similar on both facets, increasing with the alloying atom as (Ni, Cu) < Co < (Fe, Al) < Mn << (Nb, Cr) < (Ti, V) < Mo < W on the (100) facet and as (Ni, Cu) < Co < Fe < Al < Mn << Nb < Cr < Ti < (Mo, V) < W on the (111) facet. The Ni-based alloy surfaces can be divided into two groups on each facets: those that bind O weaker (binding strength ≤ 3.39 eV including the pure Ni surface and Ni alloyed with Cu, Co, Fe, Al, or Mn) and those that bind O stronger (binding strength ≥ 3.67 eV including Ni alloyed with Nb, Cr, Ti, V, Mo, or W). This divide among transition metal alloying elements occurs between groups 6 and 7 in the periodic table in which alloying elements in groups ≤ 6 bind O strongly and alloying elements in groups ≥ 7 bind O weakly.

Table 5.2 summarizes previous studies of O adsorption on the (111) facet of Ni-based alloy surfaces, with two of the most comprehensive studies of O adsorption on different surface alloys performed by Alexandrov et al. [6] and An et al. [1]. On the (111) facet, Alexandrov et al. [6] found that O binding strength increases with the alloying atom as $\text{Cu} < \text{Ni} < \text{Fe} < \text{Al} < \text{Mn} < \text{Cr}$ at a 1/16 surface alloy concentration, while An et al. [1] found the O binding strength to increase with the alloying atom as $\text{Mo} < \text{Co} < \text{Fe} < \text{Ni} < \text{Cu}$ at a 1/4 surface alloy concentration and as $\text{Cu} < \text{Ni} < \text{Co} < \text{Fe} < \text{Mo}$ at a 2/4 surface alloy concentration. The discrepancies among these studies and our study lie in the use of different O binding sites. Alexandrov et al. [6] used the equivalent of an fcc-1 site for all surfaces, An et al. [1] used the equivalent of an fcc-2 or hcp-2 site (they did not distinguish between the two) for their study at 1/4 alloy concentration and an fcc-1 or hcp-1 site for their study at 2/4 alloy concentration, while herein we use the most favorable O binding site for each surface. Comparing our results at the fcc-1 site or the fcc-2 site, with data in the Supporting Information, gives the exact same results as that of Alexandrov et al. [6] and An et al. [1]. While studies of the same adsorption site for different alloy surfaces give insight into the ligand effects, the most stable binding site needs to be used to determine differences in reaction energies on the different surfaces.

Table 5.2 Summary and comparison to previous studies of the change in binding energy, ΔE_{bind} , of atomic O on (111) Ni-based alloy surfaces compared to a pure Ni(111) bulk/surface. An[1] and Das[7] did not differentiate between fcc and hcp hollow sites, referred to as three-fold hollow (3fh) sites. The number in parentheses after the binding site indicates the number of alloying atoms at the adsorption site.

Alloy Atom	Surface Alloy Conc.	Second Layer Conc.	Bulk Alloy Conc.	Ads. Conc. (ML)	Binding Site	ΔE_{bind} (eV)	Reference
Cu	1/16	0/16	0/16	1/16	fcc (1Cu)	1.17	Alexandrov[6]
	6/8	2/8	4/8	1/8	fcc (2Cu)	0.49	Zhang[5]
	2/4	0/4	0/4	1/4	3fh (1Cu)	0.21	An[1]
	4/8	4/8	4/8	1/8	fcc (1Cu)	0.13	Zhang[5]
	2/4	2/4	2/4	1/4	3fh (1Cu)	-0.03	An[1]
	1/9	0/9	0/9	1/9	fcc (0Cu)	-0.03	this work
	1/4	0/4	0/4	1/4	fcc (0Cu)	-0.05	Wang[3]
	1/4	0/4	0/4	1/4	3fh (0Cu)	-0.11	An[1]
	1/4	1/4	1/4	1/4	3fh (0Cu)	-0.27	An[1]
Co	1/4	0/4	0/4	1/4	3fh (0Co)	0.04	An[1]
	1/9	0/9	0/9	1/9	fcc (1Co)	-0.07	this work
	2/4	0/4	0/4	1/4	3fh (1Co)	-0.10	An[1]
	4/8	4/8	4/8	1/8	hcp (2Co)	-0.23	Guo[4]
	6/8	2/8	4/8	1/8	hcp (3Co)	-0.36	Guo[4]
	8/8	0/8	4/8	1/8	hcp (3Co)	-1.10	Guo[4]
Fe	1/4	0/4	0/4	1/4	3fh (0Fe)	0.02	An[1]
	1/9	0/9	0/9	1/9	fcc (1Fe)	-0.14	this work
	1/16	0/16	0/16	1/16	fcc (1Fe)	-0.15	Alexandrov[6]
	2/4	0/4	0/4	1/4	3fh (1Fe)	-0.21	An[1]
	4/8	4/8	4/8	1/8	fcc (2Fe)	-0.54	Zhang[5]
	6/8	2/8	4/8	1/8	fcc (3Fe)	-0.75	Zhang[5]
Al	1/9	0/9	0/9	1/9	fcc (1Al)	-0.21	this work
	1/16	0/16	0/16	1/16	fcc (1Al)	-0.24	Alexandrov[6]
Mn	1/9	0/9	0/9	1/9	fcc (1Mn)	-0.28	this work
	1/16	0/16	0/16	1/16	fcc (1Mn)	-2.96	Alexandrov[6]
Nb	1/9	0/9	0/9	1/9	fcc (1Nb)	-0.76	this work
Cr	1/4	1/4	0/4	1/4	fcc (1Cr)	-0.61	Das[7]
	1/4	0/4	0/4	1/4	fcc (1Cr)	-0.75	Das[7]
	1/9	0/9	0/9	1/9	fcc (1Cr)	-0.84	this work
	2/4	0/4	0/4	1/4	3fh (2Cr)	-1.30	Das[7]
	1/16	0/16	0/16	1/16	fcc (1Cr)	-3.19	Alexandrov[6]
Ti	1/9	0/9	0/9	1/9	fcc (1Ti)	-0.89	this work
V	1/9	0/9	0/9	1/9	fcc (1V)	-0.98	this work
Mo	1/4	0/4	0/4	1/4	3fh (0Mo)	0.48	An[1]
	2/4	0/4	0/4	1/4	3fh (1Mo)	-0.35	An[1]
	1/9	0/9	0/9	1/9	top (1Mo)	-0.98	this work
W	1/9	0/9	0/9	1/9	top (1W)	-1.10	this work

As seen in Table 5.2, our findings are in good agreement with previous DFT studies at identical adsorption sites with the exception of Alexandrov et al. [6] when the alloying element is Mn or Cr. It is unclear why their results are significantly different than all other results, including the results presented here and the results by Das et al. [7] for Ni alloyed with Cr. As the concentration of the alloying element increases, the number of alloying atoms bound to O also increases, influencing the binding energy of O on the surface. An increase in the number of Cu atoms bound to O weakens the binding energy of O, while increasing the concentration of all remaining alloying elements strengthens the O binding energy.

The (100) facet of Ni-based alloys is less investigated, although a few studies have made a comparison to the (111) facet. Das et al. [7, 34] studied Ni alloyed with Cr and determined that O adsorbs stronger on the (100) facet than the (111) facet by 0.02 eV at a 1/4 surface alloy concentration and 0.04 eV at a 2/4 surface alloy concentration. These results indicate that O binds almost equally strong on the (100) and (111) facets of Ni alloyed with Cr, in good agreement with our findings. Wu et al. [33] studied Ni alloyed with Al at a 1/4 bulk alloy concentration, but different (100) and (111) surface alloy concentrations, and found that O adsorbs 0.125 eV stronger on the (100) facet than the (111) facet, in good agreement with our calculations where O adsorbs 0.21 eV stronger on the (100) facet than the (111) facet. The largest difference between binding energies on the two facets is 0.29 eV, on the pure Ni surface, while the smallest difference is 0.06 eV, when the alloying element is Cr.

Carbon Binding

The binding of C is only stable at a hollow site (-0.36 eV) on the (100) facet and has positive binding energies at a bridge site (1.84 eV) and a top site (3.37 eV) relative to a single graphite atom. All binding energies are positive on the (111) facet with a slightly more favorable interaction at an hcp hollow site (1.04 eV) than an fcc hollow site (1.09 eV) and a very unfavorable interaction at a top site (3.45 eV). The interaction energy of C at a bridge site on the (111) facet could not be calculated. Different reference species shift the binding energy of C; for example, using atomic C in gas phase as a reference species instead of graphite lowers the binding energy by

9.11 eV, which would make all the C binding energies herein negative. Many previous DFT studies of C binding on Ni alloy surfaces use atomic C in the gas phase as a reference species and get very negative binding energies for C on the (111) facet [1, 4, 5, 50-52, 55, 56], while a study using graphite as a reference species gets positive C binding energies on the (111) facet [32], similar to what is calculated here. Herein we use graphite as the reference species because it is a more realistic material than a gas phase C species. However, we mostly discuss the difference in binding energies rather than absolute binding energies in order to normalize the choice of reference species.

The most stable sites for C binding on Ni is at hollow sites, similar to O binding but with C at hcp hollow sites and O at fcc hollow sites on the (111) facet, although the energy difference between the two (111) hollow sites is small for both adsorbates. Previous DFT studies have also found that C is most stable at hollow sites on the (100) facet and hcp sites on the (111) facet of a pure Ni surface [50-52, 56]. C binds 1.40 eV stronger to the (100) facet than the (111) facet, which is in good agreement with previous DFT studies that have found C adsorption to be 1.05 eV [56], 1.44 eV [50, 52], 1.51 eV [51], and 1.57 eV [55] stronger on Ni(100) than Ni(111). Both O and C are more stable on the (100) facet than the (111) facet, but the increase in stability on the (100) facet is 5 times larger for C than O.

When the pure Ni surface is alloyed, the binding energy and the most stable binding sites of C on the surface can change, as shown in Table 5.3. A complete list of C binding energies for all surfaces at different sites can be found in Tables 5.S3 and 5.S4 in the Supporting Information. For all Ni-based alloy surfaces, C is most stable at hollow sites and hcp sites on the (100) and (111) facets, respectively, and in general the Ni-rich sites are more stable, in contrast to O adsorption. The binding of C on the (100) facet is most stable at the hollow-3 site for the majority of the surfaces, with the exceptions being the Cu alloy surface, where the hollow-2 site is 0.02 eV more stable than the hollow-3 site, and the Al alloy surface, where the hollow-2 and hollow-3 sites are equally stable. The hcp-2 site is the most stable site on all (111) surfaces, except when the alloying element is Co or Cr in which the hcp-1 site is more stable by 0.03 eV and 0.02 eV, respectively.

Table 5.3 Effects of substituting an alloying atom for a single Ni surface atom on carbon adsorption. Binding energy (eV) referenced to a single graphite atom, binding energy difference relative to pure Ni (eV), and binding site for C adsorption on the (100) and (111) facets of Ni-based alloys at 1/9 ML coverage. For site locations, refer to Figure 5.1. The binding energy of C on Ni(100) alloyed with Al is equally stable at hollow-2 and hollow-3 sites.

Alloying Atom	(100) facet			(111) facet		
	E_{bind}	ΔE_{bind}	site	E_{bind}	ΔE_{bind}	site
Ni (no alloy)	-0.36	0.00	hol	1.04	0.00	hcp
Co	-0.38	-0.02	hol-3	1.03	-0.01	hcp-1
Fe	-0.39	-0.03	hol-3	1.03	-0.01	hcp-2
Cu	-0.37	-0.01	hol-2	0.99	-0.05	hcp-2
Mn	-0.41	-0.05	hol-3	0.97	-0.07	hcp-2
Al	-0.43	-0.07	hol-2,3	0.98	-0.06	hcp-2
Cr	-0.45	-0.09	hol-3	0.92	-0.12	hcp-1
V	-0.52	-0.16	hol-3	0.95	-0.09	hcp-2
W	-0.60	-0.24	hol-3	1.03	-0.01	hcp-2
Mo	-0.58	-0.22	hol-3	1.00	-0.04	hcp-2
Nb	-0.57	-0.21	hol-3	0.95	-0.09	hcp-2
Ti	-0.52	-0.16	hol-3	0.89	-0.15	hcp-2

All alloy surfaces calculated increase the binding strength of C on both the (100) and (111) facets, shown by the negative ΔE_{bind} values in Table 5.3. The largest increase in C binding strength is 0.24 eV on the (100) facet, by alloying with W, and 0.15 eV on the (111) facet, by alloying with Ti. The changes in binding energy on the alloy surfaces are much smaller for the C adsorbate than the O adsorbate, with the average C binding energy difference over both facets 19% that for O. The binding energy of C increases with the alloying atom on the (100) facet as (Ni, Cu, Co, Fe) < Mn < Al < Cr < (V, Ti) < (Nb, Mo) < W and on the (111) facet as (Ni, Fe, W, Co) < (Mo, Cu, Al, Mn) < (Nb, V) < Cr < Ti. Unlike O adsorption, the trends for C adsorption are quite different for the different facets, however the range of C binding energies is less than 0.25 eV, so small fluctuations in the binding energy have a larger effect on the trend. The average binding energy of C on the (100) facet is five times stronger than on the (111) facet, with the largest difference being 1.63 eV, when the alloying element is W, and the smallest difference being 1.36 eV, when the alloying element is Cu.

Table 5.4 compares our findings for C adsorption on Ni-based alloys with previous DFT studies in the literature. An et al. [1] found that the C binding strength on the (111) facet increases with the alloying atom as $\text{Mo} < \text{Co} < \text{Fe} < \text{Ni} < \text{Cu}$ for a 1/4 surface alloy concentration with C at sites equivalent to our hcp-2 or fcc-2 sites and as $\text{Mo} < \text{Cu} < \text{Fe} < \text{Co} < \text{Ni}$ for a 2/4 surface alloy concentrations with C at sites equivalent to our hcp-1 or fcc-1 sites. Here we calculate the binding strength of C to increase with the alloying atom as $\text{Co} < (\text{Ni}, \text{Fe}) < (\text{Mo}, \text{Cu})$ at the hcp-2 site and as $\text{Cu} < \text{Fe} < (\text{Mo}, \text{Ni}, \text{Co})$ at the hcp-1 site, in good agreement with the results presented by An et al. [1]. The only exception is the Mo alloy surface which is on the opposite side of the trends for the two studies, and it is unclear why this discrepancy occurs. None of the other previous DFT studies, shown in Table 5.4, are directly comparable to this work due to different bulk and surface alloy concentrations, yet are included here for completeness.

Table 5.4 Summary and comparison to previous studies of the change in binding energy, ΔE_{bind} , of atomic C on (111) Ni-based alloy surfaces compared to a pure Ni(111) bulk/surface. An[1] did not differentiate between fcc and hcp hollow sites and refer to the adsorption sites as three-fold hollow (3fh) sites. The number in parentheses after the binding site indicates the number of alloying atoms at the adsorption site.

Alloy Atom	Surface Alloy Conc.	Second Layer Conc.	Bulk Alloy Conc.	Ads. Conc. (ML)	Binding Site	ΔE_{bind} (eV)	Reference
Fe	0/4	1/4	4/20	1/4	hcp (0Fe)	0.52	Tsai[2]
	2/4	0/4	0/4	1/4	3fh (1Fe)	0.06	An[1]
	4/8	4/8	4/8	1/8	fcc (2Fe)	0.03	Zhang[5]
	1/4	0/4	0/4	1/4	3fh (0Fe)	0.02	An[1]
	1/9	0/9	0/9	1/9	hcp (0Fe)	-0.01	this work
	6/8	2/8	4/8	1/8	hcp (3Fe)	-0.19	Zhang[5]
W	1/9	0/9	0/9	1/9	hcp (0W)	-0.01	this work
Co	0/4	1/4	4/20	1/4	hcp (0Co)	0.51	Tsai[2]
	1/4	0/4	0/4	1/4	3fh (0Co)	0.08	An[1]
	2/4	0/4	0/4	1/4	3fh (1Co)	0.01	An[1]
	1/9	0/9	0/9	1/9	hcp (1Co)	-0.01	this work
	4/8	4/8	4/8	1/8	hcp (2Co)	-0.10	Guo[4]
	6/8	2/8	4/8	1/8	hcp (3Co)	-0.18	Guo[4]
	8/8	0/8	4/8	1/8	hcp (3Co)	-0.24	Guo[4]
Mo	1/4	0/4	0/4	1/4	3fh (0Mo)	0.49	An[1]
	2/4	0/4	0/4	1/4	3fh (1Mo)	0.43	An[1]
	1/9	0/9	0/9	1/9	hcp (0Mo)	-0.04	this work
Cu	6/8	2/8	4/8	1/8	hcp (2Cu)	1.00	Zhang[5]
	2/4	0/4	0/4	1/4	3fh (1Cu)	0.35	An[1]
	2/4	2/4	2/4	1/4	3fh (1Cu)	0.26	An[1]
	4/8	4/8	4/8	1/8	bridge (0Cu)	0.15	Zhang[5]
	1/9	0/9	0/9	1/9	hcp (0Cu)	-0.05	this work
	1/4	1/4	1/4	1/4	3fh (0Cu)	-0.13	An[1]
	1/4	0/4	0/4	1/4	3fh (0Cu)	-0.21	An[1]
Al	2/4	0/4	1/4	1/4	hcp (1Al)	0.86	Saadi[32]
	1/9	0/9	0/9	1/9	hcp (0Al)	-0.06	this work
	0/4	2/4	1/4	1/4	hcp (0Al)	-0.24	Saadi[32]
	1/4	1/4	1/4	1/4	hcp (0Al)	-0.37	Saadi[32]
	0/4	1/4	1/4	1/4	hcp (0Al)	-0.43	Saadi[32]
Mn	0/4	1/4	4/20	1/4	hcp (0Mn)	0.46	Tsai[2]
	1/9	0/9	0/9	1/9	hcp (0Mn)	-0.07	this work
Nb	1/9	0/9	0/9	1/9	hcp (0Nb)	-0.09	this work
V	1/9	0/9	0/9	1/9	hcp (0V)	-0.09	this work
Cr	1/9	0/9	0/9	1/9	hcp (1Cr)	-0.12	this work
Ti	1/9	0/9	0/9	1/9	hcp (0Ti)	-0.15	this work

Carbon Monoxide Binding

The adsorption of CO on the (100) facet of pure Ni is most stable at a hollow site (-1.97 eV) compared to a bridge site (-1.88 eV) or a top site (-1.69 eV), in agreement with previous DFT studies on Ni(100) [50, 51, 57]. CO on the (111) facet binds slightly stronger at an hcp hollow site (-1.94 eV) than an fcc hollow site (-1.93 eV), and weaker at a top site (-1.57 eV). The binding energy of CO at a bridge site on the (111) facet could not be calculated. Previous DFT studies on Ni(111) also found the hcp site [50, 51, 57] or the fcc site [58] to be most stable, in agreement with experimental studies [59, 60]. The adsorption of CO is 0.03 eV more stable on the (100) facet than the (111) facet, in good agreement with previous DFT studies that find CO adsorption to be 0.03 eV [50, 52], 0.07 eV [25, 57], 0.08 eV [51], and 0.14 eV [55] stronger on Ni(100) than Ni(111). Hammer et al. [61] calculated CO binding energies of -2.00 eV on Ni(100) and -1.88 eV on Ni(111) when using the same PBE functional, in excellent agreement with the results obtained here. Experimental results find slightly weaker CO binding energies of -1.27 eV [62] or -1.30 eV [63] on Ni(100) and -1.30 eV [64] or -1.35 eV [62] on Ni(111), however it is well known that DFT overbinds chemisorbed systems, especially with the PBE functional [53, 54].

The binding energies at the most stable binding sites for CO on the different Ni-based alloy surfaces are shown in Table 5.5. A complete list of CO binding energies for different sites on all surfaces can be found in Tables 5.S5 and 5.S6 in the Supporting Information. The lowest energy CO binding sites are Ni-rich hollow sites for all surfaces and both facets, similar to C binding, with the exception of the Ni(100) facet alloyed with V, Cr, or Ti in which the hollow-1 site is more stable by 0.02 eV, 0.15 eV, and 0.18 eV, respectively. The binding of CO on all (111) surfaces is strongest at the hcp-2 site compared to the other Ni-rich hollow sites, however the binding strength is within 0.06 eV at the fcc-2, fcc-3, hcp-2, and hcp-3 sites for each surface.

Table 5.5 Effects of substituting an alloying atom for a single Ni surface atom on carbon monoxide adsorption. Binding energy (eV) referenced to CO in vacuum, binding energy difference relative to pure Ni (eV), and binding site for 1/9 ML CO adsorption on the (100) and (111) facets of Ni-based alloys. For site locations, refer to Figure 5.1. On many surfaces, the CO binding energy is equal at multiple sites indicated by multiple site assignments.

Alloying Atom	(100) facet			(111) facet		
	E_{bind}	ΔE_{bind}	site	E_{bind}	ΔE_{bind}	site
Ni (no alloy)	-1.97	0.00	hol	-1.94	0.00	hcp
Co	-1.98	-0.01	hol-3	-1.93	0.01	hcp-2
Fe	-1.97	0.00	hol-3	-1.94	0.00	hcp-2 fcc-2
Cu	-1.98	-0.01	hol-2	-1.96	-0.02	hcp-2
Mn	-1.98	-0.01	hol-2	-1.97	-0.03	hcp-2
Al	-2.02	-0.05	hol-2	-2.01	-0.07	hcp-2
Nb	-2.05	-0.08	hol-3	-2.00	-0.06	hcp-2
Mo	-2.06	-0.09	hol-3	-1.99	-0.05	hcp-2,3 fcc-3
W	-2.07	-0.10	hol-3	-1.99	-0.05	hcp-2,3 fcc-3
V	-2.06	-0.09	hol-1	-2.02	-0.08	hcp-2
Cr	-2.14	-0.17	hol-1	-2.01	-0.07	hcp-2 fcc-2
Ti	-2.20	-0.23	hol-1	-2.04	-0.10	hcp-2

The addition of many of the alloying elements on the (100) and (111) facets strengthens the CO bond to the surface, shown by the negative ΔE_{bind} values in Table 5.5. Ni alloyed with Fe has no effect on the binding strength of CO on either facet, while Ni alloyed with Co slightly weakens the CO bond by 0.01 eV on the (111) facet. The alloying elements affect CO binding similarly on both facets, with the binding strength of CO increasing with the alloying atom as (Ni, Fe, Co, Cu, Mn) < Al < (Nb, V, Mo, W) < Cr < Ti on the (100) facet and as (Co, Ni, Fe) < (Cu, Mn) < (Mo, W, Nb, Al, Cr, V) < Ti on the (111) facet. The maximum CO binding energy difference, due to alloying with Ti on both facet, is 0.23 eV on the (100) facet and 0.10 eV on the (111) facet. This is five times smaller than the maximum change in O binding energy caused by alloying the Ni surface and about equal to the change in C binding energy. CO binds stronger to the (100) facet than the (111) facet for all Ni-based alloy surfaces, with the largest difference being 0.16 eV, when Ni is alloyed

with Ti, and the smallest difference being 0.01 eV, when Ni is alloyed with Al or Mn. Overall, CO binds similarly on both facets and across all Ni-based alloy surfaces.

A comparison of the results presented here of CO binding energy on the (111) facet with previous DFT studies is shown in Table 5.6. The results by Wang et al. [3] show excellent agreement with the results here for CO adsorption on Ni alloyed with Cu, and are the only results with a comparable binding site and bulk composition. Although the other results in Table 5.6 cannot be compared as easily, it is still evident that alloying Ni with Co or Fe decreases the binding strength of CO, alloying with Cu has a neutral effect, and alloying with Al increases the strength of CO binding.

Table 5.6 Summary and comparison to previous studies of the change in binding energy, ΔE_{bind} , of CO on (111) Ni-based alloy surfaces compared to a pure Ni(111) bulk/surface. A three-fold hollow (3fh) site designation in this work indicates that the hcp and fcc hollow sites are energetically equal. The number in parentheses after the binding site indicates the number of alloying atoms at the adsorption site.

Alloy Atom	Surface Alloy Conc.	Second Layer Conc.	Bulk Alloy Conc.	Ads. Conc. (ML)	Binding Site	ΔE_{bind} (eV)	Reference
Co	4/8	4/8	4/8	1/8	hcp (1Co)	0.12	Guo[4]
	6/8	2/8	4/8	1/8	hcp (2Co)	0.10	Guo[4]
	8/8	0/8	4/8	1/8	hcp (3Co)	0.07	Guo[4]
	1/9	0/9	0/9	1/9	hcp (0Co)	0.01	this work
Fe	6/8	2/8	4/8	1/8	top (1Fe)	0.17	Zhang[5]
	4/8	4/8	4/8	1/8	fcc (2Fe)	0.13	Zhang[5]
	1/9	0/9	0/9	1/9	3fh (0Fe)	0.00	this work
Cu	6/8	2/8	4/8	1/8	top (0Cu)	0.21	Zhang[5]
	1/4	0/4	0/4	1/4	fcc (0Cu)	0.01	Wang[3]
	1/9	0/9	0/9	1/9	hcp (0Cu)	-0.02	this work
	4/8	4/8	4/8	1/8	bridge (0Cu)	-0.03	Zhang[5]
Mn	1/9	0/9	0/9	1/9	hcp (0Mn)	-0.03	this work
Mo	1/9	0/9	0/9	1/9	3fh (0Mo)	-0.05	this work
W	1/9	0/9	0/9	1/9	3fh (0W)	-0.05	this work
Nb	1/9	0/9	0/9	1/9	hcp (0Nb)	-0.06	this work
Al	2/4	0/4	1/4	1/4	bridge (0Al)	0.11	Saadi[32]
	1/9	0/9	0/9	1/9	hcp (0Al)	-0.07	this work
	0/4	1/4	1/4	1/4	hcp (0Al)	-0.09	Kośmider[31]
	0/4	2/4	1/4	1/4	fcc (0Al)	-0.25	Saadi[32]
	1/4	1/4	1/4	1/4	hcp (0Al)	-0.34	Kośmider[31]
	0/4	1/4	1/4	1/4	3fh (0Al)	-0.35	Saadi[32]
	1/4	1/4	1/4	1/4	hcp (0Al)	-0.45	Saadi[32]
Cr	1/9	0/9	0/9	1/9	3fh (0Cr)	-0.07	this work
V	1/9	0/9	0/9	1/9	hcp (0V)	-0.08	this work
Ti	1/9	0/9	0/9	1/9	hcp (0Ti)	-0.10	this work

Alloying Atom Effect

The ligand effect and ensemble effect are analyzed in order to understand the trends in binding energy of the adsorbates to the different alloy surfaces. The ligand effect attributes changes in the chemical properties of the alloy surfaces to different electronic structures of the surfaces while the ensemble effect attributes changes in the surface properties to changes in the ensemble of atoms that make up the binding

site [65]. Herein we assess the ligand effect by calculating changes in the d-band center of the alloy surfaces relative to the pure Ni surface. According to Hammer and Nørskov's d-band model [66-68], the adsorption energy of an adsorbate scales with the d-band center of the surface. In general, a higher d-band center, closer to the Fermi level, indicates a stronger bond between the adsorbate and the surface.

The d-band center of the top layer of the pure Ni surface is calculated to be -1.17 eV and -1.21 eV for the (100) and (111) facets, respectively. Including the top two layers changes the d-band center to -1.33 eV and -1.34 eV for Ni(100) and Ni(111), respectively. This is in good agreement with previous calculations for the Ni(111) d-band center of -1.16 eV [3, 69], -1.32 eV [70], and -1.87 eV [71]. The d-band center for the (111) facet is lower than for the (100) facet, which has been shown to be the trend for many metals including Ni [56], Pd [72], Pt [73], Cu [74-76], and Ag [77], and correlates well with weaker binding of O, C, and CO on the (111) facet relative to the (100) facet.

The d-band center for the top layer of the (100) and (111) facets for each Ni-based alloy surface is shown in Table 5.7. The shift in d-band center is similar on both facets and increases with the alloying atom as $\text{Cu} < \text{Ni} < \text{Co} < (\text{Al}, \text{Fe}) < (\text{W}, \text{Mo}, \text{Mn}) < \text{V} < (\text{Nb}, \text{Cr}, \text{Ti})$ on the (100) facet and as $\text{Cu} < (\text{Co}, \text{Ni}) < \text{Fe} < (\text{Mo}, \text{W}, \text{Al}) < \text{Mn} < (\text{Nb}, \text{V}, \text{Ti}) < \text{Cr}$ on the (111) facet. The surfaces can be divided into two groups on each facet: those with lower d-band centers (d-band center shift ≤ 0.16 eV including Ni alloyed with Cu, Co, Fe, Al, W, Mo, and Mn) and those with higher d-band centers (d-band center shift ≥ 0.17 eV including Ni alloyed with V, Nb, Ti, and Cr). In general, the d-band center is lower for Ni alloyed with elements that are farther to the right in the periodic table and higher when the alloying elements are farther left.

Table 5.7 Effects of substituting an alloying atom for a single Ni surface atom on the d-band of the top surface layer and the Bader charge of the alloying atom for the (100) and (111) facets. The d-band center relative to the Fermi level, ϵ_d (eV), the change in the d-band center relative to the pure Ni surface, $\Delta\epsilon_d$ (eV), the width of the d-band, w_d (eV), the number of valence d-electrons per surface transition metal atom, n_d , and the Bader charge of the alloying atom ($|e|$) are shown.

Alloying Atom	ϵ_d		$\Delta\epsilon_d$		w_d		n_d		Bader charge	
	100	111	100	111	100	111	100	111	100	111
Cu	-1.21	-1.26	-0.04	-0.05	1.79	1.82	8.63	8.56	0.05	0.02
Ni (no alloy)	-1.17	-1.21	0.00	0.00	1.79	1.80	8.70	8.49	-0.05	0.00
Al	-1.10	-1.11	0.07	0.10	1.82	1.85	8.69	8.65	1.41	1.53
Co	-1.14	-1.23	0.03	-0.02	1.84	1.85	8.51	8.49	0.20	0.13
Fe	-1.09	-1.18	0.08	0.03	1.86	1.94	8.28	8.27	0.41	0.33
W	-1.05	-1.12	0.12	0.09	1.94	1.94	8.32	8.37	0.61	0.64
Mn	-1.01	-1.07	0.16	0.14	1.92	1.89	8.28	8.30	0.58	0.53
Mo	-1.03	-1.13	0.14	0.08	1.90	1.95	8.17	8.29	0.56	0.62
V	-0.97	-1.02	0.20	0.19	1.87	1.92	8.12	7.99	0.86	0.96
Nb	-0.93	-1.04	0.24	0.17	1.93	1.94	8.14	7.98	0.98	0.99
Ti	-0.91	-1.00	0.26	0.21	1.93	1.92	7.90	8.05	1.17	1.23
Cr	-0.91	-0.82	0.26	0.39	1.91	2.13	8.24	7.92	0.68	0.67

Kitchin et al. [78] have shown, through alloying Pt with 3d transition metals, that alloying with elements to the left in the periodic table decreases the d-band center, which is opposite to the trend observed here. The difference between the two d-band center trends is related to the differences in the alloying systems and in the electron filling of the d-band. The alloying system studied by Kitchin et al. [78] contained a sandwich structure with the alloying atoms in the second layer so that the number of d-electrons per atom in the top layer remained constant. When alloying with elements to the left in the periodic table, the larger d-orbital overlap causes an increase in the d-band width, as seen by Kitchin et al. [78] and here in Table 5.7 (roughly going down the column). In the work by Kitchin et al. [78], the d-band center must be shifted down with increasing d-band width in order to keep the d-band filling constant, so alloying with elements to the left in the periodic table shifts the d-band center down. Here, the alloying atom is in the top layer and the number of valence d-electrons per surface transition metal atom is not constant, as shown in

Table 5.7. The number of valence d-electrons is determined by calculating the fraction of electronic d-states below the Fermi level for the entire surface and multiplying by 10 due to the d-orbitals of each surface transition metal atoms being able to hold ten valence electrons. Due to the number of d-electrons not being constant, we find the d-band center shifts up for alloying elements farther left in the periodic table, as is observed for pure transition metal surfaces.

Cu has a completely filled d-orbital, unlike the remaining alloying elements considered herein, resulting in Ni alloyed with Cu having the most negative d-band center on both facets. The d-band center of Ni alloyed with Co is similar to the pure Ni surface, but is shifted slightly positive on the (100) facet and slightly negative on the (111) facet. This is in good agreement with previous DFT studies that found Ni(111) alloyed with Cu lowers the d-band center by 0.12 eV at a 1/4 alloy concentration [3, 69] while Ni alloyed with Co lowers the d-band center by 0.06 eV [70] or 0.11 eV [71] at a 1/2 alloy concentration. Here, the d-band center is lowered by 0.05 eV for the (111) Cu alloy and by 0.02 eV for the (111) Co alloy, which is expected for a lower 1/9 alloy concentration than the references cited above. Alloying Ni with all remaining elements shifts the d-band center in the positive direction.

The Bader charges of the atoms in the clean surfaces are calculated, with the charge on the alloying atom shown in Table 5.7. The charge on the Al alloying atom is largest, followed by the charge on the Ti alloying atom. Of the transition metal alloying elements, the charge increases as the alloying element moves left in the periodic table (roughly going down the column in Table 5.7). The more noble transition metals such as Cu and Ni have almost no charge, while the least noble transition metal Ti has a Bader charge greater than 1 |e|. The surfaces in which the transition metal alloying atom has the largest charge correspond to the surfaces with a smaller number of valence d-electrons and a higher d-band center. The surfaces with a high d-band center and a more positively charged transition metal alloying atom are also the surfaces that bind the adsorbates more strongly.

The ensemble effect in an alloy surface accounts for changes in the catalytic properties of the surface due to changes in the chemical composition of the adsorption site. To understand the ensemble effect, the range of binding energies on the different

alloy surfaces is calculated for each adsorbate as the difference between the most strongly bound adsorbate and the most weakly bound adsorbate at each unique site. For example, at the fcc-1 site O binds most strongly (-3.89 eV) to Ni alloyed with V and most weakly (-2.60 eV) to Ni alloyed with Cu and has a range of 1.29 eV. The ranges for only the unique hollow sites are shown in Table 5.8, but the same trends are observed for all binding sites, as can be calculated from the Supporting Information.

Table 5.8 Binding energy range, eV, of O, C, and CO over the twelve alloy surfaces at each unique hollow site. For site locations, refer to Figure 5.1. CO binding at the hcp-1 and fcc-1 sites was not stable. The O binding range at the hollow-1 site does not include Ni alloyed with W and the C binding range at the hcp-1 and fcc-1 sites do not include Ni alloyed with Al, W, Nb, or Ti.

	O range	C range	CO range
hollow-1	0.90	0.60	0.43
hcp-1	1.33	0.62	-----
fcc-1	1.29	0.53	-----
hollow-2	0.06	0.13	0.07
hcp-2	0.13	0.17	0.11
fcc-2	0.14	0.17	0.10
hollow-3	0.10	0.25	0.12
hcp-3	0.09	0.12	0.08
fcc-3	0.12	0.10	0.08

The binding energy range for all adsorbates at sites neighboring an alloying atom are much larger than for Ni-only sites, suggesting that the chemical makeup of the adsorption site has a large influence on the binding energy of the adsorbate and that the ensemble effect plays a large role in the difference in binding energies on the different alloy surfaces. In general, O binds most stably adjacent to the alloying atom and has binding energies that vary across the different alloy surfaces while C and CO bind most stably away from the alloying atom and have binding energies that stay relatively the same across the different alloy surfaces. The O binding energies vary across the different alloy surfaces due to the differences in the composition of the binding sites while the C and CO binding energies are similar across the different alloy surfaces due to the similarity in the chemical composition of the binding sites, indicative of the ensemble effect.

Figure 5.2 shows the binding energy of the C, CO, and O adsorbates on the (100) and (111) facets versus the shift in d-band center for each Ni-based alloy surface. The binding energies plotted in black, blue, and red are at the most common strongest binding sites across the alloy surfaces and correspond to the hollow-3 and hcp-2 sites for both C and CO on the (100) and (111) facets, respectively, and the hollow-1 and fcc-1 sites for O on the (100) and (111) facets, respectively. Plotted in gray are binding energies of each adsorbate at the most stable binding site if the binding site is different than the most common binding site. The trendlines are for each adsorbate at the most common binding site.

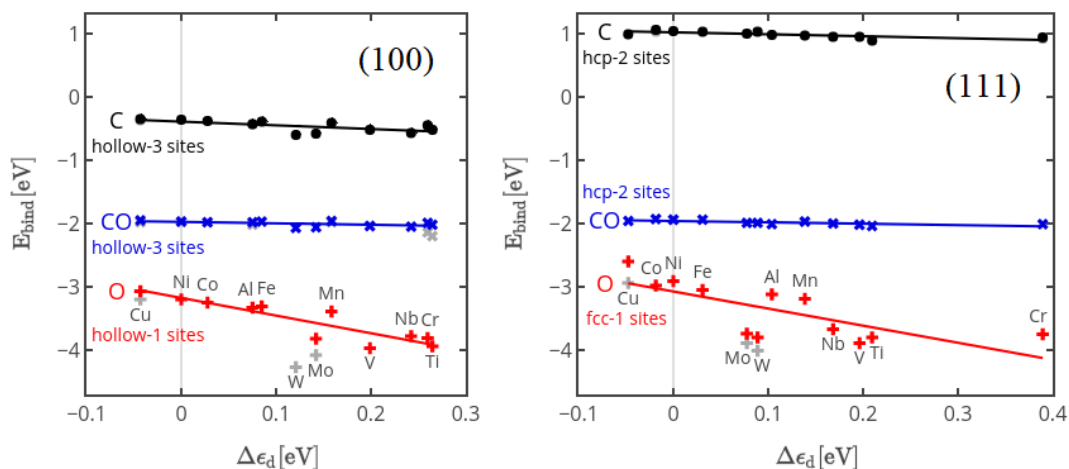


Figure 5.2 Binding energy of C, CO, and O adsorbates versus the shift in d-band center of the alloyed (100) and (111) surfaces. Colored points (dark in black and white) represent binding energies at the most common strongest site, as indicated in the figure. The binding of O on Ni(100) alloyed with W is not stable at the hollow-1 site. Gray points (light in black and white) represent binding energies at the most stable site if the site is different from the most common site.

All trendlines for the binding energies as a function of the d-band center shift in Figure 5.2 have a negative slope, indicating that surfaces with higher d-band centers bind adsorbates more strongly, in good agreement with the d-band model for different transition metals proposed by Hammer and Nørskov [66-68]. According to Hammer and Nørskov's d-band model, surfaces with a high d-band center (Ni alloyed with V, Nb, Ti, and Cr) should bind the adsorbates strongest and surfaces with a low d-band center (pure Ni and Ni alloyed with Cu, Co, Fe, Al, W, Mo, and Mn) should

bind adsorbates weakest, as is seen here. The only exception is Ni alloyed with W and Mo, which have a lower d-band center than would be expected for how strongly they bind the adsorbates. The most negative trendline slopes in Figure 5.2 are for O binding, which is bound adjacent to the alloying atom, while the C and CO binding slopes, with C and CO bound at Ni-only sites, have only a slightly negative slope. The difference between sites adjacent to the alloying atom and Ni-only sites suggests that the ensemble effect plays a role in the change in adsorbate binding. While the ligand effect plays a small role in changing the adsorbate binding energies, the difference in binding energies on the different alloy surfaces is dominated by the ensemble effect.

Carbon Monoxide Reactions

Multiple reaction mechanisms for C-Ni formation from CO have been proposed in the literature, such as the CO dissociation reaction $\text{CO} \rightarrow \text{C} + \text{O}$ and the Boudouard reaction $2\text{CO} \rightarrow \text{C} + \text{CO}_2$ [79, 80]. Both reactions are examined here from a thermodynamic perspective using gas phase CO as the reference species when comparing reactant and product energies.

For CO dissociation using the gas phase CO reference state, the CO reactant energy is the same as the CO binding energy reported earlier, but the C+O product energy is calculated differently than the individual O and C adsorbates reported earlier. The reactant energy, product energy, and reaction energy for CO dissociation on the (100) and (111) facets of all Ni-based alloy surfaces are shown in Table 5.9. In all instances, the binding energies correspond to the adsorbate being in its minimum energy adsorption site, and the C+O product energy corresponds to the two adsorbates being infinitely far apart.

Table 5.9 Effects of substituting an alloying atom for a single Ni surface atom on CO dissociation reaction energies on the (100) and (111) facets of Ni-based alloys. Reactant energy, product energy, and net reaction energy (eV) are shown relative to one CO molecule in the gas phase.

Alloying Atom	(100) facet			(111) facet		
	E(CO _{ads})	E(C _{ads} +O _{ads})	E _{rxn}	E(CO _{ads})	E(C _{ads} +O _{ads})	E _{rxn}
Ni (no alloy)	-1.97	-2.38	-0.42	-1.94	-0.71	1.23
Cu	-1.98	-2.40	-0.42	-1.96	-0.78	1.18
Co	-1.98	-2.46	-0.48	-1.93	-0.78	1.14
Fe	-1.97	-2.53	-0.56	-1.94	-0.85	1.10
Al	-2.02	-2.59	-0.58	-2.01	-0.97	1.04
Mn	-1.98	-2.63	-0.65	-1.97	-1.05	0.91
Cr	-2.14	-3.07	-0.92	-2.01	-1.66	0.35
Nb	-2.05	-3.18	-1.13	-2.00	-1.54	0.46
Ti	-2.20	-3.29	-1.09	-2.04	-1.74	0.30
V	-2.06	-3.32	-1.26	-2.02	-1.77	0.25
Mo	-2.06	-3.48	-1.41	-1.99	-1.72	0.28
W	-2.07	-3.70	-1.63	-1.99	-1.81	0.19

The CO dissociation reaction is exothermic on the (100) facet and endothermic on the (111) facet for all Ni-based alloy surfaces. The reaction energy on the pure Ni surface is -0.42 eV on the (100) facet and 1.23 eV on the (111) facet, similar to previous calculations which find CO dissociation reaction energies of -0.36 eV [50], 0.12 eV [51], and 0.82 eV [57] on the (100) facet and 1.35 eV [52], 1.90 eV [51], and 2.60 eV [57] on the (111) facet. CO dissociation becomes more favorable in the presence of an alloying atom, with each alloying atom affecting CO dissociation similarly on both facets. The CO dissociation reaction becomes increasingly exothermic on the (100) facet with the alloying atom as (Ni, Cu) > Co > (Fe, Al) > Mn >> Cr > Ti > Nb > V > Mo > W and increasingly less endothermic on the (111) facet with the alloying atom as Ni > Cu > Co > Fe > Al > Mn >> Nb > Cr > (Ti, Mo) > V > W.

The CO reactant energy is similar for all surfaces and both facets, but a wide range of C+O product energies exists on the different alloy surfaces and facets, shown visually in Figure 5.3. The C+O products become more thermodynamically favorable with the alloying atom as Ni > (Cu, Co) > Fe > Al > Mn >> Nb > Cr > (Mo, Ti) > V > W on the (111) facet and as (Ni, Cu) > Co > Fe > Al > Mn >> Cr > Nb > Ti >

$V > Mo > W$ on the (100) facet. There is a divide on each facet between the surfaces that bind C+O weakly and have a more endothermic CO dissociation reaction energy (pure Ni surface and Ni alloyed with Cu, Co, Fe, Al, and Mn) and those that bind C+O strongly and have a more exothermic CO dissociation reaction energy (Ni alloyed with W, Mo, V, Ti, Nb, and Cr).

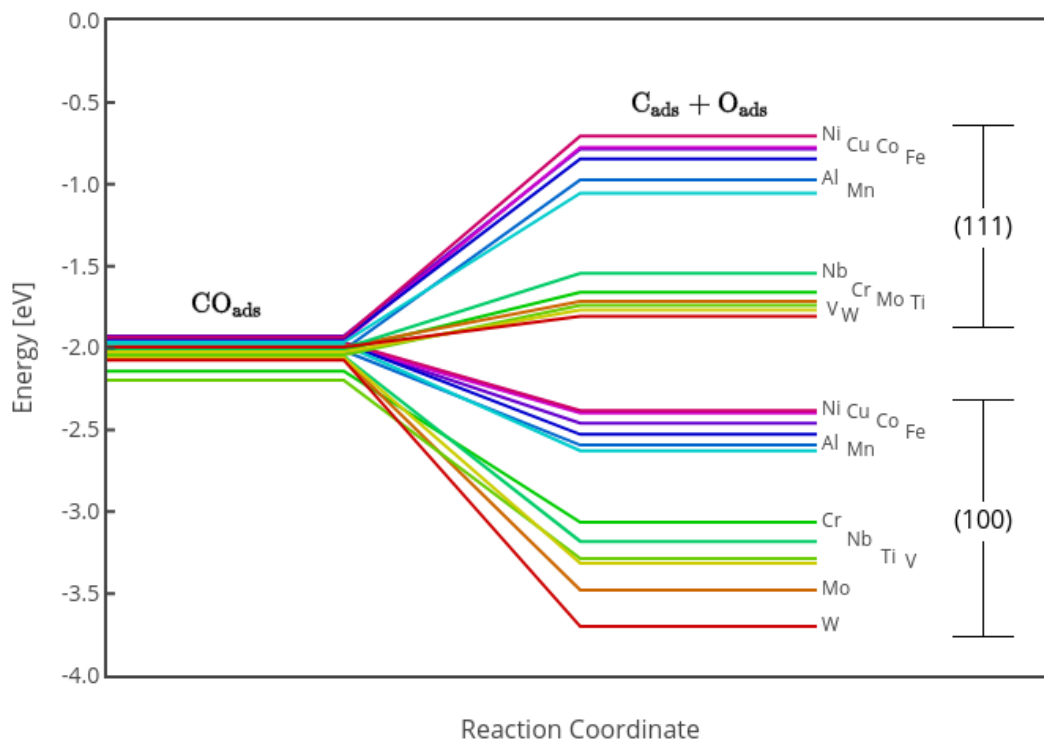


Figure 5.3 Binding energies of CO dissociation reactants and products relative to CO in the gas phase on the (100) and (111) facets of Ni surfaces alloyed with the indicated elements.

The trends in C+O product binding energies show similarities to the trends of both individual C binding and individual O binding behavior. The binding behavior of C+O is similar to C binding in that the adsorbate binding is much stronger on the (100) facet than the (111) facet. The difference in binding energies of both O and CO on the (100) and (111) facets is small compared to the difference of C binding on the two facets, so the binding of C dominates the reaction energy trends when comparing the two facets. The C+O products exhibit similar behavior to O binding in that they both have a wide range of binding energies over the different alloy surfaces. The

difference in binding strength of either C or CO on the different Ni-based alloy surfaces is much smaller than the O binding energy differences for different alloy surfaces, so the binding of O dominates the reaction energy trends when comparing the surfaces of a given facet.

In the Boudouard reaction, the 2CO reactant energy comes from adsorbed CO while the C+CO₂ product energy comes from adsorbed C and gas phase CO₂, as previous DFT studies have found CO₂ to bind weakly to the Ni surface [81, 82]. The reactant energy, product energy, and reaction energy for the Boudouard reaction on the (100) and (111) facets for all Ni-based alloy surfaces are listed in Table 5.10. All reactant and product energies are relative to two gas phase CO molecules and correspond to the adsorbates being infinitely far apart at their lowest energy site.

Table 5.10 Effects of substituting an alloying atom for a single Ni surface atom on Boudouard reaction energies on the (100) and (111) facets of Ni-based alloys. Reactant energy, product energy, and net reaction energy (eV) are shown relative to two CO molecules in the gas phase.

Alloying Atom	(100) facet			(111) facet		
	E(2CO _{ads})	E(C _{ads} +CO ₂)	E _{rxn}	E(2CO _{ads})	E(C _{ads} +CO ₂)	E _{rxn}
Ti	-4.39	-3.13	1.26	-4.09	-1.72	2.37
Cr	-4.28	-3.04	1.24	-4.03	-1.70	2.33
Al	-4.03	-3.05	0.99	-4.02	-1.63	2.39
V	-4.11	-3.13	0.99	-4.05	-1.66	2.38
W	-4.15	-3.21	0.93	-3.99	-1.58	2.40
Mo	-4.13	-3.19	0.94	-3.99	-1.61	2.37
Cu	-3.96	-2.98	0.99	-3.92	-1.62	2.30
Nb	-4.10	-3.18	0.92	-4.00	-1.66	2.34
Ni(no alloy)	-3.93	-2.97	0.96	-3.87	-1.57	2.30
Fe	-3.94	-3.00	0.94	-3.89	-1.58	2.31
Co	-3.96	-2.99	0.97	-3.85	-1.59	2.27
Mn	-3.96	-3.02	0.94	-3.93	-1.65	2.29

The Boudouard reaction is endothermic on all surfaces and both facets, with the (111) facet having the most endothermic reactions. The reaction becomes less endothermic and more favorable with the alloying atom as (Ti, Cr) > (Al, Cu, V, Co, Ni, Mn, Mo, Fe, W, Nb) on the (100) facet and as (W, Al, V, Mo, Ti) > (Nb, Cr, Fe, Cu, Ni, Mn, Co) on the (111) facet. The reaction energies within each facet are very

similar, with a total range of 0.34 eV on the (100) facet and 0.13 eV on the (111) facet, however between the two facets the reaction energies are very different, with an average reaction energy difference of 1.33 eV between the two facets. The small reaction energy ranges are due to small reactant energy ranges, 0.46 eV and 0.24 eV on the (100) and (111) facets, respectively, and small product energy ranges, 0.24 eV and 0.15 eV on the (100) and (111) facets, respectively. The small reactant energy ranges and small reactant energy differences between the two facets occur because CO binds similarly to all surfaces and both facets, with a total reactant energy range of 0.54 eV over both facets. The small product energy range on each facet and large product energy difference and reaction energy difference between the two facets are due entirely to differences in C binding, as the energy of the gas phase CO₂ product is the same for all surfaces. The reactant and product energies are shown visually in Figure 5.4.

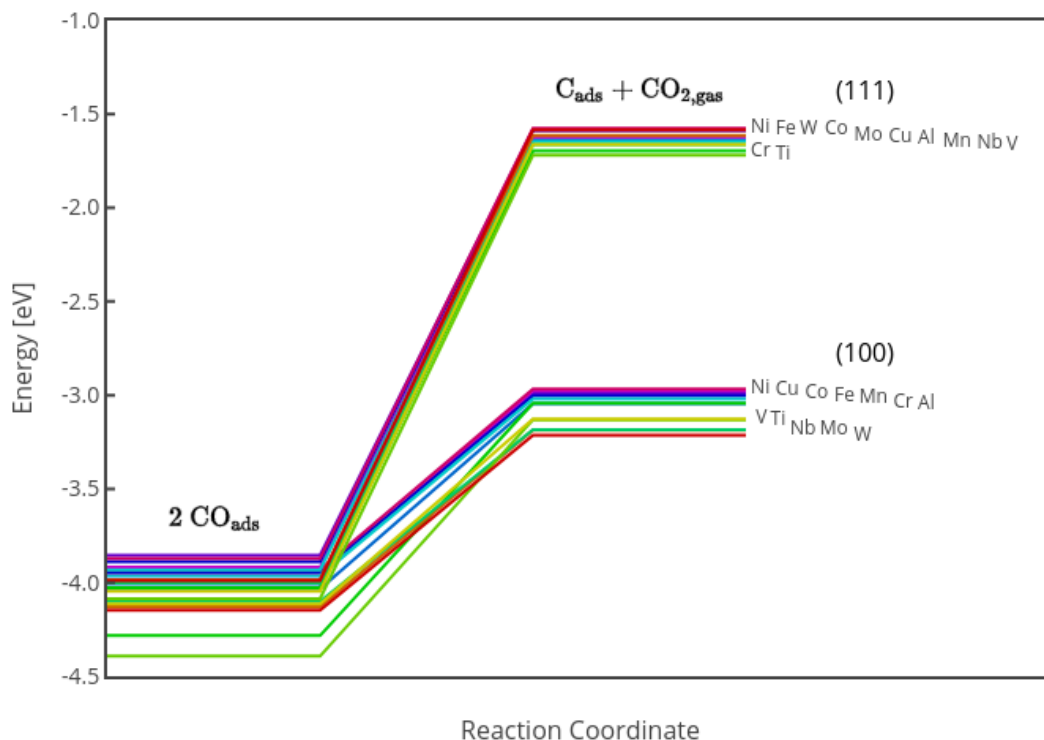


Figure 5.4 Binding energies of reactants and products in the Boudouard reaction relative to two gas phase CO molecules on the (100) and (111) facets of Ni surfaces alloyed with the indicated elements.

In a microkinetic model study on steam methane reforming, Blaylock et al. [83] calculated energies of the Boudouard reaction and the CO dissociation reaction on the Ni(111) surface at 800°C, 1 bar, and 1 ML coverage, and determined the CO dissociation reaction enthalpy to be 1.49 eV, in reasonable agreement to our calculation of 1.23 eV. Blaylock et al. [83] calculated Boudouard reaction energies in a number of different ways and found a reaction enthalpy of 1.77 eV assuming the CO₂ product remains adsorbed, 2.06 eV with a desorbed CO₂ product, and 1.49 eV with dissociation of the CO₂ product into CO+O. Their calculation of 2.06 eV for the Boudouard reaction producing desorbed CO₂ is in reasonable agreement with our calculation of 2.30 eV.

The CO dissociation reaction is thermodynamically more favorable than the Boudouard reaction on the pure Ni surface by 1.38 eV on the (100) facet and 1.07 eV on the (111) facet. The addition of an alloying element on either facet causes the CO dissociation reaction to become more exothermic but has little effect on the Boudouard reaction energies, causing the CO dissociation reaction to become even more favorable than the Boudouard reaction. The largest difference between the two reaction mechanisms is when the alloying element is W, in which the CO dissociation reaction is more favorable than the Boudouard reaction by 2.56 eV on the (100) facet and 2.21 eV on the (111) facet.

The overall CO₂ breakdown starts with CO₂ dissociation into CO and O, followed by CO breakdown via either direct CO dissociation or the Boudouard reaction. Figures showing the energies for the complete CO₂ breakdown mechanisms via CO dissociation and the Boudouard reaction are included in Figures 5.S1-5.S4 in the Supporting Information. These figures are similar to Figures 5.3 and 5.4, but are shifted down by the binding energy of O to account for the co-adsorption of CO and O and are referenced to gas phase CO₂ instead of gas phase CO.

Conclusions

The results presented herein give a well-rounded look at the products of CO₂ breakdown on Ni surfaces alloyed with the most common alloying elements in industrial applications. The binding of O occurs at alloy-rich sites for all surfaces

except Ni alloyed with Cu, in which Ni-rich sites are more stable, while the binding of C and CO occur at Ni-rich sites for the majority of the surfaces. The O adsorption energy changes significantly with the alloying elements, dividing the surfaces into a group that binds O strongly (pure Ni and Ni alloyed with Cu, Co, Fe, Al, or Mn) and a group that binds O more weakly (Ni alloyed with W, Mo, V, Cr, Nb, or Ti). This divide also exists for the C and CO adsorbates, although it is much less pronounced. All three adsorbates bind stronger on the (100) facet than the (111) facet for the majority of the Ni-based alloy surfaces, with C binding significantly stronger to the (100) facet and O and CO binding only slightly stronger to the (100) facet. The CO binding energy is comparable for all Ni-based alloy surfaces studied and both facets. The effect that the alloying atom has on the binding energies of O, C, and CO is due mainly to the ensemble effect rather than the ligand effect. The O binding energies vary across the different alloy surfaces because O binds adjacent to the alloying atom so that the binding sites are chemically different while the C and CO binding energies are relatively constant across the different alloy surfaces because they bind away from the alloying atom in binding sites that are chemically the same.

The breakdown of CO can proceed via CO dissociation or the Boudouard reaction. All reactions are endothermic except CO dissociation on the (100) facet. The CO dissociation reaction is thermodynamically more favorable than the Boudouard reaction on the (100) and (111) facets of all Ni-based alloy surfaces considered herein. Both CO breakdown mechanisms are much more favorable on the (100) facet than the (111) facet, due to the adsorbed C product being much more stable on the (100) facet. The Boudouard reaction energies are similar for all alloy surfaces within a given facet, while CO dissociation has a wide reaction energy range within each facet. The wide CO dissociation reaction energy ranges stem from the adsorbed O product having wide binding energy ranges, causing CO to dissociate more favorable on Ni alloyed with W, Mo, V, Cr, Nb, or Ti than on the pure Ni surface or Ni alloyed with Cu, Co, Fe, Al, or Mn. With applications such as inhibiting corrosion of structural materials, it is favorable to avoid CO breakdown so that the corrosive atomic species are not formed. To inhibit CO breakdown on Ni-based alloy surfaces, it is best to alloy with Cu, Co, Fe, Al, Mn, and likely other elements in groups ≥ 7 of

the periodic table. The (111) facet is better at inhibiting CO breakdown than the (100) facet, however both facets are likely to be found in structural building materials for industrial applications.

The effect of substituting an alloying element into a Ni surface has been explored for the alloying elements Al, Co, Cr, Cu, Fe, Mn, Mo, Nb, Ti, V, and W on the (100) and (111) facets. This is the first comprehensive study examining a wide range of Ni-based alloys on two common facets in a consistent manner. The knowledge gained from the binding energies of O, C, and CO on the different surfaces and the CO breakdown mechanisms via CO dissociation and the Boudouard reaction will be helpful for understanding corrosion by O and C on Ni-based alloy surfaces for applications such as those involving supercritical CO₂.

Acknowledgements

This research was performed in part using funding received from the DOE Office of Nuclear Energy's Nuclear Energy University Program, award number DE-NE0008424. This work also used the Extreme Science and Engineering Discovery Environment (XSEDE), which is supported by the National Science Foundation grant number ACI-1548562. The XSEDE Comet cluster at the San Diego Supercomputer Center was used through allocation TG-ENG170002.

References

- [1] W. An, D. Gatewood, B. Dunlap, C.H. Turner, Catalytic Activity of Bimetallic Nickel Alloys for Solid-Oxide Fuel Cell Anode Reactions from Density-Functional Theory, *Journal of Power Sources*, 196 (2011) 4724-4728.
- [2] H.C. Tsai, S.I. Morozov, T.H. Yu, B.V. Merinov, W.A. Goddard, First-Principles Modeling of Ni₄M (M = Co, Fe, and Mn) Alloys as Solid Oxide Fuel Cell Anode Catalyst for Methane Reforming, *Journal of Physical Chemistry C*, 120 (2016) 207-214.
- [3] M. Wang, Z. Fu, Z. Yang, Tuning the Performance of Ni-Based Catalyst by Doping Coinage Metal on Steam Reforming of Methane and Carbon-Tolerance, *Fuel Cells*, 14 (2014) 251-258.
- [4] X.Q. Guo, H.Y. Liu, B.J. Wang, Q. Wang, R.G. Zhang, Insight Into C + O(OH) Reaction for Carbon Elimination on Different Types of CoNi(111) Surfaces: a DFT Study, *RSC Advances*, 5 (2015) 19970-19982.

- [5] R.G. Zhang, X.Q. Guo, B.J. Wang, L.M. Ling, Insight Into the Effect of CuNi(111) and FeNi(111) Surface Structure and Second Metal Composition on Surface Carbon Elimination by O or OH: A Comparison Study with Ni(111) Surface, *Journal of Physical Chemistry C*, 119 (2015) 14135-14144.
- [6] V. Alexandrov, M.L. Sushko, D.K. Schreiber, S.M. Bruemmer, K.M. Rosso, Adsorption and Diffusion of Atomic Oxygen and Sulfur at Pristine and Doped Ni Surfaces with Implications for Stress Corrosion Cracking, *Corrosion Science*, 113 (2016) 26-30.
- [7] N.K. Das, T. Shoji, A Density Functional Study of Atomic Oxygen and Water Molecule Adsorption on Ni(111) and Chromium-Substituted Ni(111) Surfaces, *Applied Surface Science*, 258 (2011) 442-447.
- [8] M. Mecheri, Y. Le Moullec, Supercritical CO₂ Brayton Cycles for Coal-Fired Power Plants, *Energy*, 103 (2016) 758-771.
- [9] V. Firouzdor, K. Sridharan, G. Cao, M. Anderson, T.R. Allen, Corrosion of a Stainless Steel and Nickel-Based Alloys in High Temperature Supercritical Carbon Dioxide Environment, *Corrosion Science*, 69 (2013) 281-291.
- [10] R.G. Brese, J.R. Keiser, B.A. Pint, Effect of Thermal Cycling on Compatibility in CO₂ for Concentrated Solar Power Applications, *Oxidation of Metals*, 87 (2017) 631-642.
- [11] R.I. Olivares, W. Stein, T.D. Nguyen, D.J. Young, Corrosion of Nickel-Base Alloys by Supercritical CO₂, 2016.
- [12] R.I. Olivares, D.J. Young, P. Marvig, W. Stein, Alloys SS316 and Hastelloy-C276 in Supercritical CO₂ at High Temperature, *Oxidation of Metals*, 84 (2015) 585-606.
- [13] B.A. Pint, R.G. Brese, J.R. Keiser, Effect of Pressure on Supercritical CO₂ Compatibility of Structural Alloys at 750 Degrees C, *Materials and Corrosion*, 68 (2017) 151-158.
- [14] B.A. Pint, J.R. Keiser, Initial Assessment of Ni-Base Alloy Performance in 0.1 MPa and Supercritical CO₂, *Jom*, 67 (2015) 2615-2620.
- [15] A. Farjamnia, B. Jackson, The Dissociative Chemisorption of CO₂ on Ni(100): A Quantum Dynamics Study, *Journal of Chemical Physics*, 146 (2017).
- [16] H.J. Freund, M.W. Roberts, Surface Chemistry of Carbon Dioxide, *Surface Science Reports*, 25 (1996) 225-273.
- [17] S. Ghosh, S. Hariharan, A.K. Tiwari, Water Adsorption and Dissociation on Copper/Nickel Bimetallic Surface Alloys: Effect of Surface Temperature on Reactivity, *Journal of Physical Chemistry C*, 121 (2017) 16351-16365.
- [18] S. Roy, S. Hariharan, A.K. Tiwari, Pt–Ni Subsurface Alloy Catalysts: An Improved Performance toward CH₄ Dissociation, *The Journal of Physical Chemistry C*, 122 (2018) 10857-10870.

- [19] A. Logadottir, T.H. Rod, J.K. Norskov, B. Hammer, S. Dahl, C.J.H. Jacobsen, The Bronsted-Evans-Polanyi Relation and the Volcano Plot for Ammonia Synthesis over Transition Metal Catalysts, *Journal of Catalysis*, 197 (2001) 229-231.
- [20] J.K. Norskov, T. Bligaard, A. Logadottir, S. Bahn, L.B. Hansen, M. Bollinger, H. Bengaard, B. Hammer, Z. Sljivancanin, M. Mavrikakis, Y. Xu, S. Dahl, C.J.H. Jacobsen, Universality in Heterogeneous Catalysis, *Journal of Catalysis*, 209 (2002) 275-278.
- [21] T. Bligaard, J.K. Norskov, S. Dahl, J. Matthiesen, C.H. Christensen, J. Sehested, The Bronsted-Evans-Polanyi Relation and the Volcano Curve in Heterogeneous Catalysis, *Journal of Catalysis*, 224 (2004) 206-217.
- [22] M.K. Rajumon, K. Prabhakaran, C.N.R. Rao, Adsorption of Oxygen on (100), (110) and (111) Surfaces of Ag, Cu and Ni: An Electron Spectroscopic Study, *Surface Science*, 233 (1990) L237-L242.
- [23] J.T. Stuckless, C.E. Wartnaby, N. AlSarraf, S.J.B. DixonWarren, M. Kovar, D.A. King, Oxygen Chemisorption and Oxide Film Growth on Ni{100}, {110}, and {111}: Sticking Probabilities and Microcalorimetric Adsorption Heats, *Journal of Chemical Physics*, 106 (1997) 2012-2030.
- [24] W.B. Zhang, C. Chen, H.Q. Xie, A Comparative Density-Functional Theory Investigation of Oxygen Adsorption on Stepped Ni Surfaces $3(hkl) \times (111) hkl = (111), (100), (110)$: Role of Terrace Orientation, *Journal of the Physical Society of Japan*, 82 (2013).
- [25] A. Mohsenzadeh, T. Richards, K. Bolton, DFT Study of the Water Gas Shift Reaction on Ni(111), Ni(100) and Ni(110) Surfaces, *Surface Science*, 644 (2016) 53-63.
- [26] R.S. Bordoli, J.C. Vickerman, J. Wolstenholme, Surface Coverage Measurements by SIMS for CO Adsorption on a Number of Metals and for CO and H₂S Co-Adsorption on Ni(110), (100) and (111), *Surface Science*, 85 (1979) 244-262.
- [27] A. Brown, J.C. Vickerman, SIMS Studies of Adsorbate Structure .1. CO Adsorption on Ru(001), Ni(111) and Ni(100), *Surface Science*, 117 (1982) 154-164.
- [28] M. Shayegan, R.E. Glover, R.L. Park, Low Temperature Adsorption of CO and O₂ on Ni(100) and Ni(111): Evidence for Precursors, *Journal of Vacuum Science & Technology a-Vacuum Surfaces and Films*, 4 (1986) 1333-1335.
- [29] A. Grossmann, W. Erley, H. Ibach, Adsorbate-Induced Surface Stress: CO on Ni(100) and Ni(111), *Surface Science*, 313 (1994) 209-214.
- [30] S. Masuda, R. Suzuki, M. Aoki, Y. Morikawa, R. Kishi, M. Kawai, Spatial Electron Distribution of CO Adsorbed on Ni(100) and Ni(111) Surfaces Probed by Metastable Impact Electron Spectroscopy, *Journal of Chemical Physics*, 114 (2001) 8546-8554.

- [31] K. Kośmider, Theoretical Study of CO and Pb Adsorption on the Ni(111) and Ni₃Al(111) Surfaces, *Applied Surface Science*, 256 (2010) 4806-4812.
- [32] S. Saadi, B. Hinnemann, C.C. Appel, S. Helveg, F. Abild-Pedersen, J.K. Norskov, First-Principles Investigations of Ni₃Al(111) and NiAl(110) Surfaces at Metal Dusting Conditions, *Surface Science*, 605 (2011) 582-592.
- [33] Q. Wu, S.S. Li, Y. Ma, S.K. Gong, Comparison of O Adsorption on Ni₃Al (001), (011), and (111) Surfaces Through First-Principles Calculations, *Physica B-Condensed Matter*, 407 (2012) 2321-2328.
- [34] N.K. Das, T. Shoji, Early Stage Oxidation of Ni-Cr Binary Alloy (111), (110) and (100) Surfaces: A Combined Density Functional and Quantum Chemical Molecular Dynamics Study, *Corrosion Science*, 73 (2013) 18-31.
- [35] G. Kresse, J. Hafner, Ab Initio Molecular Dynamics for Liquid Metals, *Physical Review B*, 47 (1993) 558-561.
- [36] G. Kresse, J. Hafner, Ab Initio Molecular-Dynamics Simulation of the Liquid-Metal-Amorphous-Semiconductor Transition in Germanium, *Physical Review B*, 49 (1994) 14251-14269.
- [37] G. Kresse, J. Furthmuller, Efficient Iterative Schemes for Ab Initio Total-Energy Calculations Using a Plane-Wave Basis Set, *Physical Review B*, 54 (1996) 11169-11186.
- [38] G. Kresse, J. Furthmuller, Efficiency of Ab-Initio Total Energy Calculations for Metals and Semiconductors Using a Plane-Wave Basis Set, *Computational Materials Science*, 6 (1996) 15-50.
- [39] J. Towns, T. Cockerill, M. Dahan, I. Foster, K. Gaither, A. Grimshaw, V. Hazlewood, S. Lathrop, D. Lifka, G.D. Peterson, R. Roskies, J.R. Scott, N. Wilkins-Diehr, XSEDE: Accelerating Scientific Discovery, *Computing in Science & Engineering*, 16 (2014) 62-74.
- [40] S.R. Bahn, K.W. Jacobsen, An Object-Oriented Scripting Interface to a Legacy Electronic Structure Code, *Computing in Science & Engineering*, 4 (2002) 56-66.
- [41] J.P. Perdew, K. Burke, M. Ernzerhof, Generalized Gradient Approximation Made Simple, *Physical Review Letters*, 77 (1996) 3865-3868.
- [42] J.P. Perdew, K. Burke, M. Ernzerhof, Errata: Generalized Gradient Approximation Made Simple, *Physical Review Letters*, 78 (1997) 1396-1396.
- [43] P.E. Blöchl, Projector Augmented-Wave Method, *Physical Review B*, 50 (1994) 17953-17979.
- [44] G. Kresse, D. Joubert, From Ultrasoft Pseudopotentials to the Projector Augmented-Wave Method, *Physical Review B*, 59 (1999) 1758-1775.
- [45] N.W. Ashcroft, N.D. Mermin, *Solid State Physics*, Holt, Rinehart and Winston, New York, 1976.

- [46] G. Henkelman, A. Arnaldsson, H. Jónsson, A Fast and Robust Algorithm for Bader Decomposition of Charge Density, *Computational Materials Science*, 36 (2006) 354-360.
- [47] E. Sanville, S.D. Kenny, R. Smith, G. Henkelman, Improved Grid-Based Algorithm for Bader Charge Allocation, *Journal of Computational Chemistry*, 28 (2007) 899-908.
- [48] W. Tang, E. Sanville, G. Henkelman, A Grid-Based Bader Analysis Algorithm without Lattice Bias, *Journal of Physics-Condensed Matter*, 21 (2009).
- [49] M. Yu, D.R. Trinkle, Accurate and Efficient Algorithm for Bader Charge Integration, *Journal of Chemical Physics*, 134 (2011).
- [50] C. Fan, Y.A. Zhu, M.L. Yang, Z.J. Sui, X.G. Zhou, D. Chen, Density Functional Theory-Assisted Microkinetic Analysis of Methane Dry Reforming on Ni Catalyst, *Industrial & Engineering Chemistry Research*, 54 (2015) 5901-5913.
- [51] X.B. Hao, B.J. Wang, Q. Wang, R.G. Zhang, D.B. Li, Insight Into Both Coverage and Surface Structure Dependent CO Adsorption and Activation on Different Ni Surfaces from DFT and Atomistic Thermodynamics, *Physical Chemistry Chemical Physics*, 18 (2016) 17606-17618.
- [52] Y.A. Zhu, D. Chen, X.G. Zhou, W.K. Yuan, DFT Studies of Dry Reforming of Methane on Ni Catalyst, *Catalysis Today*, 148 (2009) 260-267.
- [53] F. Abild-Pedersen, M.P. Andersson, CO Adsorption Energies on Metals with Correction for High Coordination Adsorption Sites - A Density Functional Study, *Surface Science*, 601 (2007) 1747-1753.
- [54] J. Wellendorff, T.L. Silbaugh, D. Garcia-Pintos, J.K. Norskov, T. Bligaard, F. Studt, C.T. Campbell, A Benchmark Database for Adsorption Bond Energies to Transition Metal Surfaces and Comparison to Selected DFT Functionals, *Surface Science*, 640 (2015) 36-44.
- [55] J.A. Herron, J. Scaranto, P. Ferrin, S. Li, M. Mavrikakis, Trends in Formic Acid Decomposition on Model Transition Metal Surfaces: A Density Functional Theory study, *ACS Catalysis*, 4 (2014) 4434-4445.
- [56] J.D. Li, E. Croiset, L. Ricardez-Sandoval, Methane Dissociation on Ni (100), Ni (111), and Ni (553): A Comparative Density Functional Theory Study, *Journal of Molecular Catalysis A: Chemical*, 365 (2012) 103-114.
- [57] A. Mohsenzadeh, T. Richards, K. Bolton, A Density Functional Theory Study of Hydrocarbon Combustion and Synthesis on Ni Surfaces, *Journal of Molecular Modeling*, 21 (2015).
- [58] G.C. Wang, Y.H. Zhou, Y. Morikawa, J. Nakamura, Z.S. Cai, X.Z. Zhao, Kinetic Mechanism of Methanol Decomposition on Ni(111) Surface: A Theoretical Study, *Journal of Physical Chemistry B*, 109 (2005) 12431-12442.

- [59] A. Beniya, N. Isomura, H. Hirata, Y. Watanabe, Low Temperature Adsorption and Site-Conversion Process of CO on the Ni(111) Surface, *Surface Science*, 606 (2012) 1830-1836.
- [60] G. Held, J. Schuler, V. Sklarek, H.P. Steinruck, Determination of Adsorption Sites of Pure and Coadsorbed CO on Ni(111) by High Resolution X-ray Photoelectron Spectroscopy, *Surface Science*, 398 (1998) 154-171.
- [61] B. Hammer, L.B. Hansen, J.K. Norskov, Improved Adsorption Energetics Within Density-Functional Theory Using Revised Perdew-Burke-Ernzerhof Functionals, *Physical Review B*, 59 (1999) 7413-7421.
- [62] J.T. Stuckless, N. Al-Sarraf, C. Wartnaby, D.A. King, Calorimetric Heats of Adsorption for CO on Nickel Single Crystal Surfaces, *Journal of Chemical Physics*, 99 (1993) 2202-2212.
- [63] J.C. Tracy, Structural Influences on Adsorption Energy. II. CO on Ni(100), *Journal of Chemical Physics*, 56 (1972).
- [64] J.B. Miller, H.R. Siddiqui, S.M. Gates, J.N. Russell, J.T. Yates, J.C. Tully, M.J. Cardillo, Extraction of Kinetic Parameters in Temperature Programmed Desorption: A Comparison of Methods, *Journal of Chemical Physics*, 87 (1987) 6725-6732.
- [65] P. Liu, J.K. Norskov, Ligand and Ensemble Effects in Adsorption on Alloy Surfaces, *Physical Chemistry Chemical Physics*, 3 (2001) 3814-3818.
- [66] B. Hammer, J.K. Norskov, Electronic Factors Determining the Reactivity of Metal Surfaces, *Surface Science*, 343 (1995) 211-220.
- [67] B. Hammer, J.K. Norskov, Why Gold is the Noblest of All the Metals, *Nature*, 376 (1995) 238-240.
- [68] B. Hammer, J.K. Norskov, Theoretical Surface Science and Catalysis - Calculations and Concepts, in: B.C. Gates, H. Knozinger (Eds.) *Advances in Catalysis*, Vol 45: Impact of Surface Science on Catalysis2000, pp. 71-129.
- [69] P.J. Zuo, Z.M. Fu, Z.X. Yang, First-Principles Study on the Mechanism of Coking Inhibition by the Ni(111) Surface Doped with IB-Group Metals at the Anode of Solid Oxide Fuel Cells, *Journal of Power Sources*, 242 (2013) 762-767.
- [70] H.M. Sun, X.J. Yang, L.J. Zhao, Y. Li, J.M. Zhang, L. Tang, Y.N. Zou, C. Dong, J.S. Lian, Q. Jiang, Nanostructured $\text{Co}_x\text{Ni}_{1-x}$ Bimetallic Alloys for High Efficient and Ultrafast Adsorption: Experiments and First-Principles Calculations, *RSC Advances*, 6 (2016) 9209-9220.
- [71] H.Y. Liu, R.G. Zhang, R.X. Yan, B.J. Wang, K.C. Xie, CH_4 Dissociation on NiCo (111) Surface: A First-Principles Study, *Applied Surface Science*, 257 (2011) 8955-8964.
- [72] Q. Ge, M. Neurock, Correlation of Adsorption Energy with Surface Structure: Ethylene Adsorption on Pd Surfaces, *Chemical Physics Letters*, 358 (2002) 377-382.

- [73] Z.H. Liu, J.C. Chai, G.J. Xu, Q.F. Wang, G.L. Cui, Functional Lithium Borate Salts and Their Potential Application in High Performance Lithium Batteries, *Coordination Chemistry Reviews*, 292 (2015) 56-73.
- [74] K. Sun, M.H. Zhang, L.C. Wang, Effects of Catalyst Surface and Hydrogen Bond on Ethanol Dehydrogenation to Ethoxy on Cu Catalysts, *Chemical Physics Letters*, 585 (2013) 89-94.
- [75] S.S. Tafreshi, A. Roldan, N.H. de Leeuw, Density Functional Theory Study of the Adsorption of Hydrazine on the Perfect and Defective Copper (100), (110), and (111) Surfaces, *Journal of Physical Chemistry C*, 118 (2014) 26103-26114.
- [76] G.C. Wang, J. Nakamura, Structure Sensitivity for Forward and Reverse Water-Gas Shift Reactions on Copper Surfaces: A DFT Study, *Journal of Physical Chemistry Letters*, 1 (2010) 3053-3057.
- [77] W.A. Saidi, H.J. Feng, K.A. Fichthorn, Binding of Polyvinylpyrrolidone to Ag Surfaces: Insight into a Structure-Directing Agent from Dispersion-Corrected Density Functional Theory, *Journal of Physical Chemistry C*, 117 (2013) 1163-1171.
- [78] J.R. Kitchin, J.K. Norskov, M.A. Barteau, J.G. Chen, Modification of the Surface Electronic and Chemical Properties of Pt(111) by Subsurface 3d Transition Metals, *Journal of Chemical Physics*, 120 (2004) 10240-10246.
- [79] E.M. Muller-Lorenz, H.J. Grabke, Coking by Metal Dusting of Steels, *Materials and Corrosion-Werkstoffe Und Korrosion*, 50 (1999) 614-621.
- [80] D.L. Trimm, Catalysts for the Control of Coking During Steam Reforming, *Catalysis Today*, 49 (1999) 3-10.
- [81] S.G. Wang, D.B. Cao, Y.W. Li, J.G. Wang, H.J. Jiao, Chemisorption of CO₂ on Nickel Surfaces, *Journal of Physical Chemistry B*, 109 (2005) 18956-18963.
- [82] K. Czelej, K. Cwieka, K.J. Kurzydowski, CO₂ Stability on the Ni Low-Index Surfaces: van der Waals Corrected DFT Analysis, *Catalysis Communications*, 80 (2016) 33-38.
- [83] D.W. Blaylock, T. Ogura, W.H. Green, G.J.O. Beran, Computational Investigation of Thermochemistry and Kinetics of Steam Methane Reforming on Ni(111) under Realistic Conditions, *Journal of Physical Chemistry C*, 113 (2009) 4898-4908.

Supporting Information

Table 5.S1 Binding energies, in eV, for O adsorption on Ni-based alloy (100) surfaces. Binding energies are calculated relative to O₂ in vacuum. In the pictures, green is nickel, gray is the alloying atom, and red is oxygen. Oxygen is not stable at top-2, top-3, bridge-2, or bridge-4 sites.

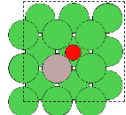
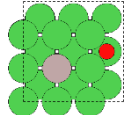
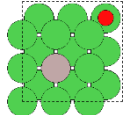
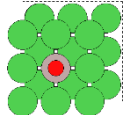
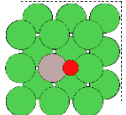
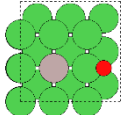
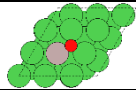
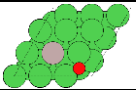
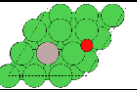
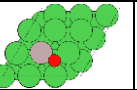
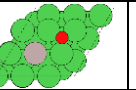
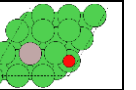
						
Alloying Atom	hollow-1	hollow-2	hollow-3	top-1	bridge-1	bridge-3
Ni (no alloy)	-3.20	-3.20	-3.20	-1.30	-2.50	-2.50
Cu	-3.07	-3.20	-3.18	-0.39	-2.09	-2.48
Co	-3.25	-3.20	-3.21	-1.89	-2.70	-2.50
Fe	-3.31	-3.21	-3.21	-2.03	-2.75	-2.51
Al	-3.33	-3.24	-3.20	-1.61	-2.86	-2.51
Mn	-3.39	-3.21	-3.21	-2.23	-2.84	-2.51
Nb	-3.78	-3.18	-3.28	-3.68	-3.76	-2.51
Cr	-3.81	-3.24	-3.21	-3.58	-3.70	-2.59
Ti	-3.94	-3.21	-3.27	-3.23	-3.71	-2.53
V	-3.97	-3.21	-3.26	-3.79	-3.94	-2.52
Mo	-3.82	-3.18	-3.27	-4.08	-3.96	-2.52
W	-----	-3.20	-3.28	-4.27	-4.14	-2.51

Table 5.S2 Binding energies, in eV, for O adsorption on Ni-based alloy (111) surfaces. Binding energies are calculated relative to O₂ in vacuum. In the pictures, green is nickel, gray is the alloying atom, and red is oxygen. Oxygen is not stable at top-2 sites or bridge sites.

						
Alloying Atom	fcc-1	fcc-2	fcc-3	hcp-1	hcp-2	hcp-3
Ni (no alloy)	-2.91	-2.91	-2.91	-2.80	-2.80	-2.80
Cu	-2.60	-2.94	-2.89	-2.51	-2.82	-2.78
Co	-2.98	-2.90	-2.92	-2.89	-2.79	-2.81
Fe	-3.05	-2.92	-2.93	-2.95	-2.79	-2.81
Al	-3.12	-2.91	-2.98	-3.05	-2.79	-2.85
Mn	-3.19	-2.93	-2.91	-3.09	-2.81	-2.79
Nb	-3.67	-2.87	-2.96	-3.59	-2.78	-2.82
Cr	-3.75	-2.92	-2.99	-3.70	-2.81	-2.84
Ti	-3.80	-2.97	-2.99	-3.73	-2.87	-2.85
Mo	-3.74	-2.86	-2.99	-3.68	-2.77	-2.84
V	-3.89	-2.95	-3.01	-3.84	-2.85	-2.86
W	-3.80	-2.83	-3.00	-3.73	-2.74	-2.85

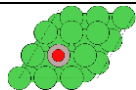
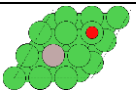
		
Alloying Atom	top-1	top-3
Ni (no alloy)	-1.06	-1.06
Cu	-0.19	-1.06
Co	-1.64	-1.05
Fe	-1.80	-1.05
Al	-1.12	-1.10
Mn	-2.07	-1.04
Nb	-3.47	-1.00
Cr	-3.41	-0.98
Ti	-2.93	-1.04
Mo	-3.89	-1.01
V	-3.54	-1.06
W	-4.01	-1.03

Table 5.S3 Binding energies, in eV, for C adsorption on Ni-based alloy (100) surfaces. Binding energies are calculated relative to graphite. In the pictures, green is nickel, gray is the alloying atom, and black is carbon. Carbon is not stable at top-2, top-3, bridge-2, or bridge-4 sites.

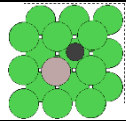
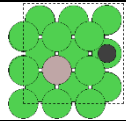
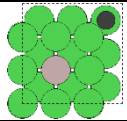
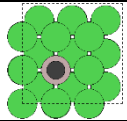
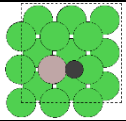
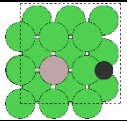
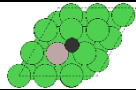
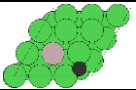
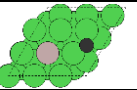
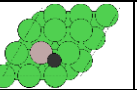
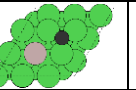
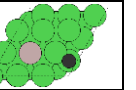
						
Alloying Atom	hollow-1	hollow-2	hollow-3	top-1	bridge-1	bridge-3
Ni (no alloy)	-0.36	-0.36	-0.36	3.37	1.84	1.84
Cu	-0.04	-0.37	-0.35	4.80	2.55	1.84
Co	-0.28	-0.34	-0.38	2.79	1.73	1.88
Fe	-0.15	-0.35	-0.39	2.89	2.01	1.87
Mn	-0.16	-0.36	-0.41	3.18	2.19	1.84
Al	0.17	-0.43	-0.43	5.34	2.81	1.83
Cr	-0.43	-0.42	-0.45	2.61	1.73	1.78
V	-0.18	-0.33	-0.52	3.56	2.08	1.95
Ti	-0.09	-0.32	-0.52	4.73	2.54	1.92
Nb	0.00	-0.30	-0.57	4.13	2.31	1.98
Mo	-0.22	-0.34	-0.58	2.77	1.69	1.97
W	-0.14	-0.35	-0.60	2.96	1.75	2.00

Table 5.S4 Binding energies, in eV, for C adsorption on Ni-based alloy (111) surfaces. Binding energies are calculated relative to graphite. In the pictures, green is nickel, gray is the alloying atom, and black is carbon. Carbon is not stable at top-2 sites or bridge sites.

						
Alloying Atom	fcc-1	fcc-2	fcc-3	hcp-1	hcp-2	hcp-3
Ni (no alloy)	1.09	1.09	1.09	1.04	1.04	1.04
Fe	1.32	1.07	1.12	1.22	1.03	1.07
W	-----	1.05	1.08	-----	1.03	1.08
Co	1.12	1.11	1.12	1.03	1.06	1.08
Mo	1.15	1.03	1.08	1.05	1.00	1.08
Cu	1.54	1.05	1.09	1.54	0.99	1.01
Al	-----	1.02	1.05	-----	0.98	1.00
Mn	1.32	1.02	1.09	1.25	0.97	1.04
Nb	-----	1.00	1.11	-----	0.95	1.10
V	1.28	0.99	1.08	1.20	0.95	1.06
Cr	1.01	0.98	1.02	0.92	0.94	0.98
Ti	-----	0.94	1.09	-----	0.89	1.06

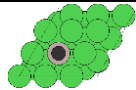
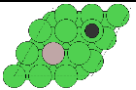
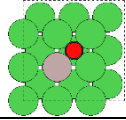
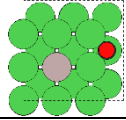
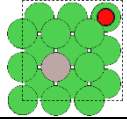
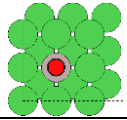
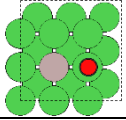
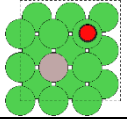
		
Alloying Atom	top-1	top-3
Ni (no alloy)	3.45	3.45
Fe	3.09	3.47
W	3.30	3.38
Co	2.95	3.47
Mo	3.11	3.39
Cu	4.74	3.44
Al	5.48	3.39
Mn	3.28	3.46
Nb	4.36	3.42
V	3.73	3.40
Cr	2.81	3.39
Ti	4.83	3.42

Table 5.S5 Binding energies, in eV, for CO adsorption on Ni-based alloy (100) surfaces. Binding energies are calculated relative to CO in vacuum. In the pictures, green is nickel, gray is the alloying atom, black is carbon, and red is oxygen.

						
Alloying Atom	hollow-1	hollow-2	hollow-3	top-1	top-2	top-3
Ni (no alloy)	-1.97	-1.97	-1.97	-1.69	-1.69	-1.69
Fe	-1.90	-1.96	-1.97	-1.43	-1.71	-1.69
Co	-1.91	-1.95	-1.98	-1.75	-1.68	-1.69
Cu	-1.86	-1.98	-1.95	-0.88	-1.71	-1.69
Mn	-1.92	-1.98	-1.96	-1.18	-1.75	-1.68
Al	-1.78	-2.02	-1.98	-0.44	-1.76	-1.69
Nb	-2.04	-1.97	-2.05	-1.23	-1.74	-1.69
V	-2.06	-1.95	-2.04	-1.42	-1.75	-1.69
Mo	-1.94	-1.96	-2.06	-1.73	-1.72	-1.68
W	-1.89	-1.96	-2.07	-1.80	-1.71	-1.69
Cr	-2.14	-1.99	-1.99	-1.65	-1.81	-1.68
Ti	-2.20	-1.97	-2.02	-1.02	-1.79	-1.69

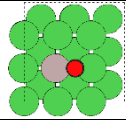
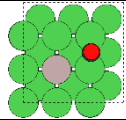
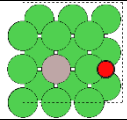
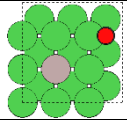
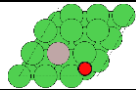
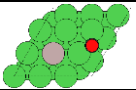
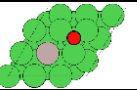
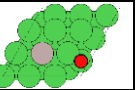
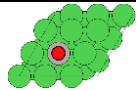
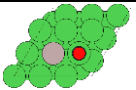
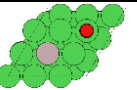
				
Alloying Atom	bridge-1	bridge-2	bridge-3	bridge-4
Ni (no alloy)	-1.88	-1.88	-1.88	-1.88
Fe	-1.62	-1.88	-1.84	-1.89
Co	-1.81	-1.87	-1.85	-1.91
Cu	-----	-1.89	-1.90	-1.86
Mn	-----	-1.90	-1.87	-1.89
Al	-----	-1.89	-1.93	-1.90
Nb	-----	-1.90	-1.89	-1.94
V	-1.69	-1.91	-1.86	-1.93
Mo	-1.85	-1.89	-1.88	-1.94
W	-1.87	-1.87	-1.88	-1.95
Cr	-----	-1.92	-1.92	-1.90
Ti	-----	-1.93	-1.88	-1.93

Table 5.S6 Binding energies, in eV, for CO adsorption on Ni-based alloy (111) surfaces. Binding energies are calculated relative to CO in vacuum. In the pictures, green is nickel, gray is the alloying atom, black is carbon, and red is oxygen. CO is not stable at the fcc-1, hcp-1, or bridge sites.

				
Alloying Atom	fcc-2	fcc-3	hcp-2	hcp-3
Co	-1.92	-1.91	-1.93	-1.92
Ni (no alloy)	-1.93	-1.93	-1.94	-1.94
Fe	-1.94	-1.92	-1.95	-1.93
Cu	-1.95	-1.93	-1.96	-1.94
Mn	-1.96	-1.93	-1.97	-1.94
Mo	-1.98	-1.99	-1.99	-1.99
W	-1.98	-1.99	-1.99	-2.00
Nb	-1.98	-1.99	-2.00	-1.99
Al	-1.99	-1.99	-2.01	-1.99
Cr	-2.01	-1.99	-2.01	-2.00
V	-2.00	-1.97	-2.02	-1.97
Ti	-2.02	-1.98	-2.04	-1.98

			
Alloying Atom	top-1	top-2	top-3
Co	-1.66	-1.57	-1.56
Ni (no alloy)	-1.57	-1.57	-1.57
Fe	-1.32	-1.58	-1.56
Cu	-0.69	-1.58	-1.58
Mn	-1.20	-1.60	-1.56
Mo	-1.54	-1.57	-1.57
W	-1.56	-----	-1.58
Nb	-1.13	-1.58	-1.56
Al	-0.31	-----	-1.60
Cr	-1.63	-1.63	-1.54
V	-1.30	-1.62	-1.59
Ti	-0.95	-1.64	-1.58

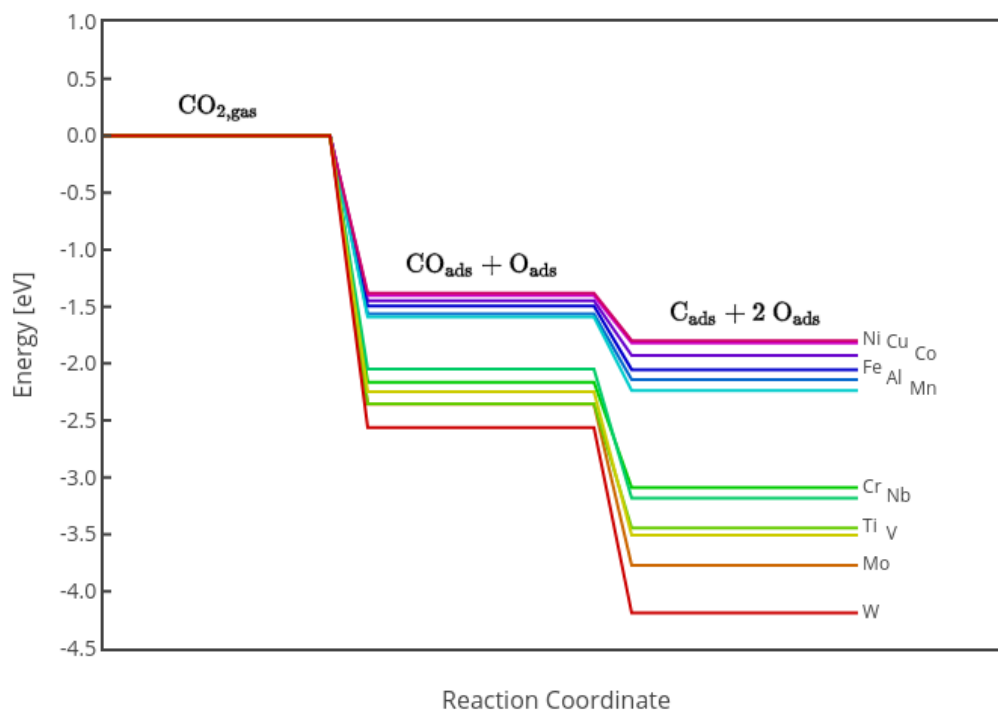


Figure 5.S1 Binding energies of CO₂ breakdown steps via CO dissociation relative to gas phase CO₂ on the (100) facet of Ni surfaces alloyed with the indicated elements.

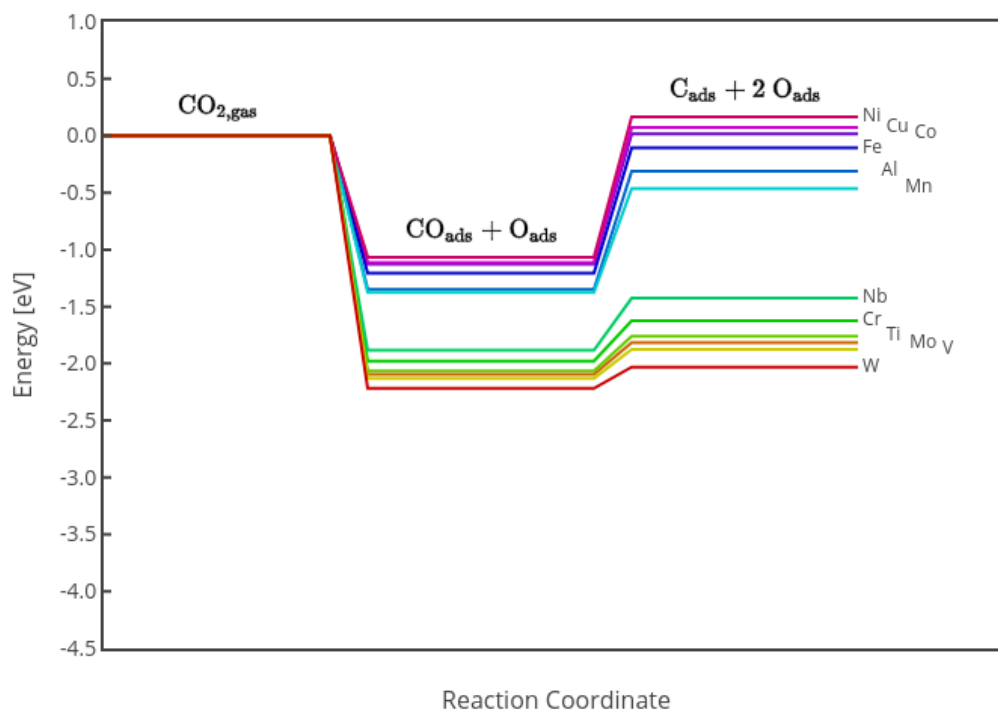


Figure 5.S2 Binding energies of CO₂ breakdown steps via CO dissociation relative to gas phase CO₂ on the (111) facet of Ni surfaces alloyed with the indicated elements.

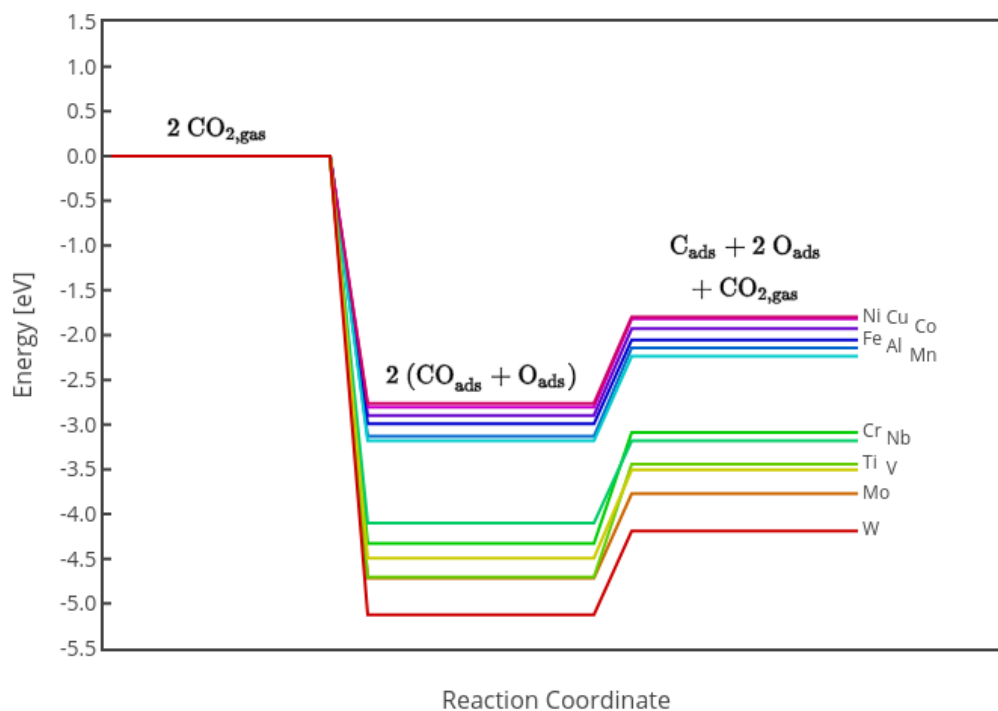


Figure 5.S3 Binding energies as CO_2 breaks down via the Boudouard reaction relative to gas phase CO_2 on the (100) facet of Ni surfaces alloyed with the indicated elements.

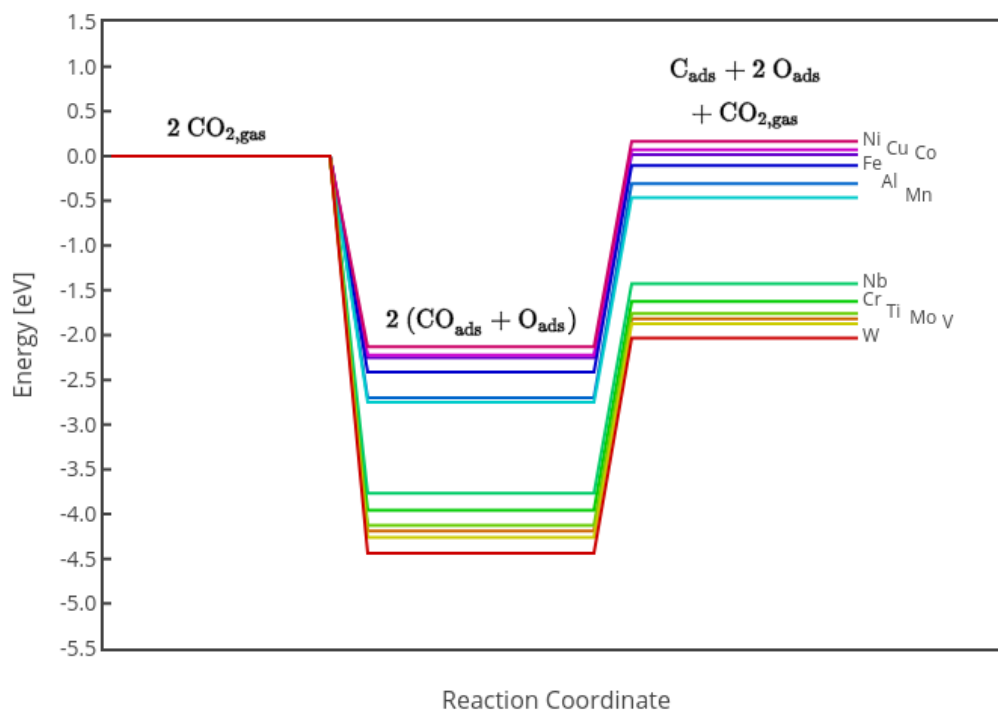


Figure 5.S4 Binding energies as CO_2 breaks down via the Boudouard reaction relative to gas phase CO_2 on the (111) facet of Ni surfaces alloyed with the indicated elements.

CHAPTER 6

FLUOROETHYLENE CARBONATE BREAKDOWN MECHANISMS
AND ENERGETICS ON TWO LITHIUM SILICIDE SURFACES

Lynza H. Sprowl¹, Líney Árnadóttir¹, Maria K. Y. Chan^{2,*}

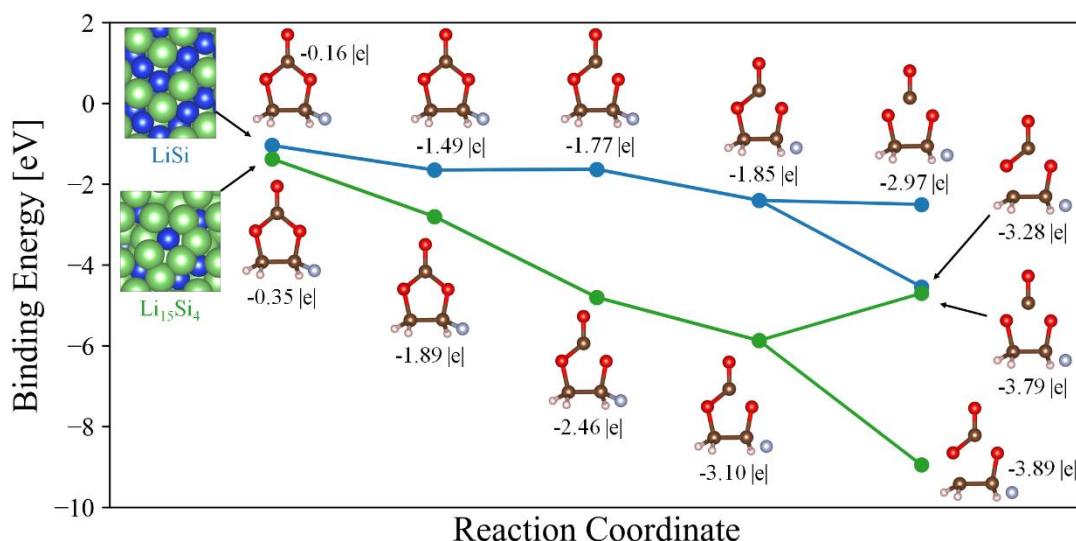
¹ School of Chemical, Biological and Environmental Engineering
Oregon State University, Corvallis, OR 97331, USA

² Center for Nanoscale Materials,
Argonne National Laboratory, Argonne, IL 60439, USA

* Corresponding author

Prepared for submission to *ACS Applied Materials & Interfaces*.

Abstract



Lithium-ion batteries are promising energy storage technologies that are being improved upon every day. One challenge with lithium-ion batteries that use a silicon anode is the reductive decomposition of electrolyte on the surface forming a solid-electrolyte interphase. The solid-electrolyte interphase is a passivating layer that prevents further electrolyte breakdown and consumption, but can also be detrimental if not formed properly by consuming lithium ions and preventing lithium ion diffusion to the anode. Fluoroethylene carbonate is one of the best electrolyte additives used to promote the formation of a more robust solid-electrolyte interphase on silicon anodes. Herein we use density functional theory to investigate the breakdown energies, mechanism, and charge transfer of fluoroethylene carbonate on a silicon anode in two different charge states: the lesser charged LiSi surface and the more charged Li₁₅Si₄ surface. The reductive decomposition of fluoroethylene carbonate on LiSi and Li₁₅Si₄ to F, CO₂, and CH₂CHO is energetically most favorable on both surfaces, but F, CO, and OCH₂CHO can also form. Forming F, CO₂, and CH₂CHO is about twice as energetically favorable as forming F, CO, and OCH₂CHO on both surfaces and the breakdown of fluoroethylene carbonate via either breakdown mechanism is about two times more favorable on the Li₁₅Si₄ surface than the LiSi surface. The electron charge transferred from the anode to the fluoroethylene

carbonate breakdown products is larger when forming F, CO₂, and CH₂CHO than when forming F, CO, and OCH₂CHO and is also larger on the Li₁₅Si₄ surface than the LiSi surface.

Introduction

Lithium-ion batteries are one of the most popular types of rechargeable batteries and are used in many electronic applications such as cellphones, power tools, laptop computers, and electric vehicles. Lithium-ion batteries work by shuttling Li⁺ ions through the electrolyte between the anode and cathode while the electrons move around the outer circuit to power a device, as shown in Figure 6.1. Common cathode materials include lithium metal oxides (LiCoO₂, LiMn₂O₄) and lithium metal phosphates (LiFePO₄), while graphite and other carbon materials are the most common anode materials [1]. However, new battery materials are being explored as consumers demand batteries with higher energy densities and higher power densities.

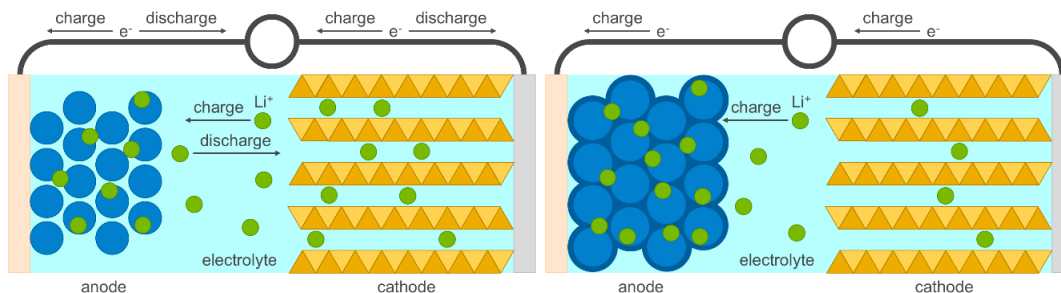


Figure 6.1 Schematic of a lithium-ion battery with a silicon anode. Upon charging the battery, the silicon expands with the addition of lithium and a solid-electrolyte interphase (dark blue) forms on the anode.

Silicon is a promising new anode material for lithium ion batteries because it can store much more lithium than conventional graphitic anodes. Silicon can alloy with lithium to form Li₂₂Si₅ with a specific capacity of 4200 mA h g⁻¹, while graphite forms LiC₆ with a specific capacity of 372 mA h g⁻¹ [2]. However, silicon has not yet been widely adopted in commercial settings due to fundamental challenges in the chemical and mechanical properties of lithiated silicon. The large uptake of lithium during battery charging leads to volumetric expansion of the silicon by ~300%-400%,

shown in Figure 6.1. This can lead to cracking and pulverization of the anode and possibly lead to silicon pieces breaking off and losing electric contact [3].

Another challenge with silicon anodes is controlling the solid-electrolyte interphase (SEI) layer that forms due to reductive decomposition of electrolyte on the anode surface, shown in Figure 6.1. The SEI may be beneficial, in that it functions as a passivating layer that prevents further electrolyte from breaking down, however it can also be detrimental in that it consumes Li^+ , lowering the anode capacity and reducing the overall lifetime of the battery [4]. The ideal SEI should be ionically conductive so that Li^+ ions reach the anode and electronically insulating so that further electrolyte is not reduced. Furthermore, the SEI becomes a challenge in Li-ion batteries with silicon anodes because the silicon anode expands and contracts with lithium uptake and release causing continuous construction and destruction of the SEI, and therefore continuous consumption of Li^+ ions [5]. Controlling the electrolyte breakdown products so that the SEI has the ideal properties is a great challenge in advancing lithium-ion batteries with silicon anodes.

The conventional electrolyte in lithium-ion batteries is composed of lithium salts and organic solvents, such as ethylene carbonate (EC) and dimethyl carbonate (DMC). In these systems, EC is the major electrolyte solvent that breaks down to form the SEI. The predominant SEI products in a cell cycled with EC are lithium ethylene dicarbonate (LEDC), Li_2CO_3 , LiF , and Li_xSiO_y [6, 7]. In batteries cycled with EC, a thick, rough SEI forms that can crack and become porous, resulting in the cell losing capacity over time [6, 8, 9]. The reductive decomposition of EC does not form an adequate SEI, so electrolyte additives, such as fluoroethylene carbonate (FEC), shown in Figure 6.2, are added to form a more robust SEI. The addition of FEC as an electrolyte additive forms a thinner SEI with fewer cracks that is more stable, homogeneous, and passivating than the SEI formed from cycling in EC, resulting in a higher capacity retention over more cycles [8, 9]. The main SEI products in a cell cycled with FEC are LiF , Li_xSiO_y , and insoluble polymeric species such as polyenes and polycarbonate [7, 10].

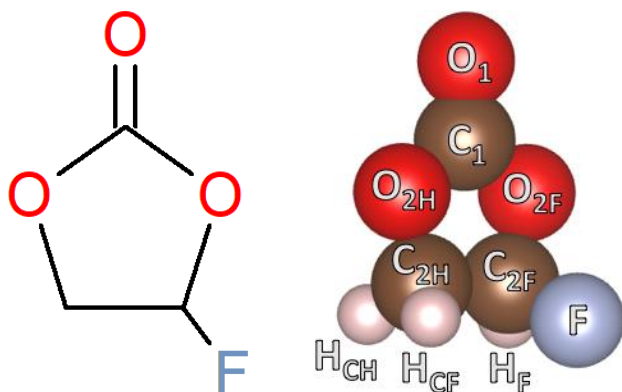


Figure 6.2 Fluoroethylene carbonate skeletal formula (left) and atomic model (right) with labels to differentiate each individual atom.

Experimental techniques have determined SEI chemical compositions and morphologies, but further information can be gained from computational techniques, such as electrolyte breakdown mechanisms and reduction dependence on the degree of silicon lithiation, which correlates to the charge state of the battery. An excellent review by Soto et al. [11] summarizes the progress in understanding SEI formation via computational methods. Using ab-initio molecular dynamics, Balbuena and coworkers [12-15] determined EC and FEC breakdown products and mechanisms on silicon anodes with various degrees of lithiation and found the products of EC reduction to depend on the degree of lithiation [12] and the FEC reduction products to be independent of the degree of lithiation [15].

On the LiSi_4 and LiSi_2 surfaces, EC gains two electrons and forms ring-opened $\text{OCOCH}_2\text{CH}_2\text{O}^{2-}$ [12]. On the LiSi surface, EC can gain two electrons forming ring-opened $\text{OCOCH}_2\text{CH}_2\text{O}^{2-}$ or it can decompose via direct two-electron transfer to the liquid phase and form $\text{CO}_3^{2-}/\text{C}_2\text{H}_4$ [12]. On the $\text{Li}_{13}\text{Si}_4$ surface, adsorbed EC can reduce via a four-electron mechanism into $\text{CO}^{2-}/\text{OCH}_2\text{CH}_2\text{O}^{2-}$ [12], via a two-electron transfer mechanism to $\text{CO}/\text{OCH}_2\text{CH}_2\text{O}^{2-}$, $\text{CO}_3^{2-}/\text{C}_2\text{H}_4$, or ring-opened $\text{OCOCH}_2\text{CH}_2\text{O}^{2-}$ [12-14]. In contrast to EC, FEC can be reduced on the surface via a two-electron mechanism to $\text{F}^-/\text{CO}/\text{OCH}_2\text{CHO}^-$ or $\text{F}^-/\text{H}/\text{CO}/\text{OCHCHO}^-$ [13], or via a four-electron mechanism to $\text{F}^-/\text{CO}_2^{2-}/\text{CH}_2\text{CHO}^-$, $\text{F}^-/\text{CO}^{2-}/\text{OCH}_2\text{CHO}^-$, or $\text{F}^-/\text{H}/\text{CO}^{2-}/\text{OCHCHO}^{2-}$ [14, 15]. Through a two-electron mechanism, FEC also was observed to eject F^- and initiate nucleophilic attack on a neighboring EC molecule, which could lead to oligomer formation [13]. With a forced one-electron transfer

mechanism of a $\text{Li}^+(\text{FEC}^-)$ complex in vacuum, the products are $\text{F}^-/\text{CO}_2/\text{CH}_2\text{CHO}$ [13]. The biggest difference between the EC and FEC dissociation products, aside from the formation of F^- from FEC, is the presence of CO_3^{2-} formed from EC and CO_2 or CO_2^{2-} formed from FEC. Both EC and FEC are observed to ring-open and form CO with varying charge states.

Density functional theory studies have determined binding energies and reaction energies of EC as it decomposes on silicon anode surfaces [16-18] and in vacuum [19]. On a silicon surface without any Li, EC breakdown is most favorable on Si(100), with an intact binding energy of -1.1 eV and a ring-opened energy of -3.2 eV [16], while on a silicon surface with one Li atom, EC binds strongest to Li/Si(111) with a binding energy of -1.27 eV and can dissociate to O and ring-closed $\text{CO}_2\text{C}_2\text{H}_4$ with a final energy of about -2 eV [17]. On a silicon cluster with one Li atom, EC can also gain one electron forming ring-opened $\text{CH}_2\text{CH}_2\text{OCO}_2^-$ with a reaction energy of -5.88 eV or two electrons forming $\text{CO}_3^{2-}/\text{C}_2\text{H}_4$ with a reaction energy of -10.74 eV [18]. In a study of $\text{Li}^+(\text{EC})$ in vacuum, FEC was found to form a ring-opened complex $\text{Li}^+(\text{CH}_2\text{CH}_2\text{OCO}_2^-)$ with a final energy of -5.08 eV or further breakdown to $\text{LiCO}_3^-/\text{C}_2\text{H}_4$ with a final energy of -7.09 eV [19]. The reaction in vacuum from $2\text{Li}^+(\text{EC}^-)$ to lithium butylene dicarbonate has a total reaction energy of -7.01 eV and the reaction to lithium ethylene dicarbonate has a total reaction energy of -6.61 eV [19]. Understanding the energies of the reactions shows how energetically favorable the breakdown of EC is, at least on low-lithiation silicon, and can elucidate the most stable products.

The thermodynamics and kinetics of FEC breakdown have been explored to a lesser extent [13, 18]. On a silicon cluster with one Li^+ , the binding energy of neutral FEC is -1.14 eV, one-electron reduced FEC^- is -6.60 eV, and two-electron reduced FEC^{2-} is -9.13 eV [13, 18]. Further ring-opening mechanisms are thermodynamically favorable with small kinetic barriers after the two-electron transfer, but are either endothermic or exhibit high kinetic barriers after the one-electron transfer [13]. This is useful for understanding FEC breakdown via one- or two-electron reduction mechanisms on silicon surfaces, but previous studies have also found FEC to breakdown via four-electron reduction mechanisms and on surfaces with a higher

lithiation [14, 15]. To fully comprehend FEC breakdown, we aim to understand the energetics of FEC breakdown products from four-electron transfer mechanisms on surfaces with higher lithiation. Herein we use density functional theory to investigate FEC breakdown on LiSi and Li₁₅Si₄ surfaces. These two surfaces are chosen because they are on opposite ends of the charging spectrum, with LiSi having a low lithiation state, corresponding to a low battery charge state, and Li₁₅Si₄ being highly lithiated, corresponding to a high battery charge state.

Methods

Density functional theory (DFT) is used to examine the breakdown on FEC on the LiSi and Li₁₅Si₄ phases. The general procedure is to first analyze different facets of LiSi and Li₁₅Si₄ to determine the lowest energy facets. Next, FEC is placed onto the lowest energy facet of LiSi and Li₁₅Si₄ in different orientations to determine the lowest energy binding configurations. The lowest energy configuration of FEC on each surface is then placed across the corresponding lowest energy facet to simulate possible binding sites across the entire surface. The FEC dissociation products and reaction energies are then determined. A Bader charge analysis is performed on the FEC reductive decomposition products to understand the charge transfer for the reductive decomposition reactions. Density of states plots are compared for FEC on the LiSi and Li₁₅Si₄ surfaces to understand the difference between the two lithium silicide surfaces.

The DFT calculations are carried out using the Vienna Ab initio Simulation Package (VASP) [20-23]. The exchange-correlation energy is treated by the Perdew-Burke-Ernzerof (PBE) functional within the general gradient approximation [24, 25], while the core electrons are modeled in the projector augmented wave method [26, 27]. The calculations are spin-polarized and include van der Waals corrections via the method of Grimme [28, 29]. The calculations run until the forces on all the atoms are below 0.05 eV/Ångstrom.

The Materials Project [30] is used to obtain the structures of the bulk phase LiSi [31, 32] and Li₁₅Si₄ [33, 34]. The unit cell for LiSi is approximately 9.2, 9.2, and 5.6 Ångstroms, in the x-, y-, and z-directions, respectively. The LiSi unit cell contains

16 Li atoms and 16 Si, so it may be referred to as $\text{Li}_{16}\text{Si}_{16}$. The unit cell for $\text{Li}_{15}\text{Si}_4$ is cubic, with the x-, y-, and z-dimensions each measuring about 10.2 Ångstroms. The $\text{Li}_{15}\text{Si}_4$ unit cell contains 60 Li atoms and 16 Si atoms, so it may be referred to as $\text{Li}_{60}\text{Si}_{16}$. The energies of the bulk phases of LiSi and $\text{Li}_{15}\text{Si}_4$ are calculated with an energy cutoff of 520 eV using 4x4x6 k-points for the LiSi bulk and 3x3x3 k-points for the $\text{Li}_{15}\text{Si}_4$ bulk.

Atomic Simulation Environment (ASE) [35, 36] is used to construct the surface models. Five low-index LiSi surface facets and three low-index $\text{Li}_{15}\text{Si}_4$ surface facets are considered in order to identify the most stable surfaces. After the LiSi surface facets are made, each $\text{Li}_{16}\text{Si}_{16}$ slab is repeated a second time along the thinnest direction so that the slab x-, y-, and z-dimensions are closer to being equal in dimensions, creating a $\text{Li}_{32}\text{Si}_{32}$ slab with more of a cubic shape. This increases the total number of atoms, volume of the slab, and surface area of the slab, making the $\text{Li}_{32}\text{Si}_{32}$ facets more comparable with the $\text{Li}_{60}\text{Si}_{16}$ facets.

For surface energy calculations, the $\text{Li}_{32}\text{Si}_{32}$ and $\text{Li}_{60}\text{Si}_{16}$ slabs are then repeated in the z-direction, creating 12-22 Ångstrom thick $\text{Li}_{64}\text{Si}_{64}$ and $\text{Li}_{120}\text{Si}_{32}$ slabs, with 20 Ångstroms of vacuum between subsequent slabs. For the surface energy calculations, the middle surface layers are frozen and the remaining top and bottom surface layers are allowed to relax. The energy of all the surface slabs are calculated using 3x3x1 k-points and an energy cutoff of 520 eV. The surface energy, E_{surf} , is calculated as

$$E_{\text{surf}} = \frac{1}{2A} (E_{\text{slab}} - NE_{\text{bulk}}), \quad (6.1)$$

where E_{slab} and E_{bulk} are the total energies of the surface slab and bulk unit cell, respectively, N is the number of unit cells in the slab, and A is the surface area of one side of the surface slab. Here N = 4 for the LiSi surfaces and N = 2 for the $\text{Li}_{15}\text{Si}_4$ surfaces. The lowest energy surface facet is determined for each of the LiSi and $\text{Li}_{15}\text{Si}_4$ phases and used for the remaining calculations.

The binding energy calculations use $\text{Li}_{32}\text{Si}_{32}$ and $\text{Li}_{60}\text{Si}_{16}$ slabs. The structure of FEC is complex, and multiple binding orientations are possible. FEC is therefore

placed in different orientations across the two most stable LiSi and Li₁₅Si₄ surfaces to determine the lowest energy configurations of FEC on each surface. Four possible low energy binding orientations are chosen to probe for the lowest energy configuration: two with the FEC ring perpendicular to the surface and two with the FEC ring parallel to the surface. A course grid approach is employed at first to determine the lowest energy binding configuration while a fine grid approach is employed later for a more thorough analysis of the surface binding sites. Each initial orientation is placed in 25 different locations determined by a 5x5 even spaced mesh across the two surfaces. The bottom half of the Li₃₂Si₃₂ and Li₆₀Si₁₆ slabs are frozen while the top half of the slabs and the FEC are allowed to relax. The binding energy, E_{bind} , of FEC on the surface is calculated as

$$E_{\text{bind}} = E_{\text{slab+ads}} - (E_{\text{slab}} + E_{\text{FEC}}), \quad (6.2)$$

where $E_{\text{slab+ads}}$ is the energy of the slab with FEC adsorbed (either whole FEC or dissociated FEC), E_{slab} is the energy of the clean slab before FEC adsorption, and E_{FEC} is the energy of FEC in vacuum. The calculations to determine the FEC binding orientation are performed with an energy cutoff of 520 eV and 1x1x1 k-point. A single k-point is chosen here to determine the FEC orientation, and later more k-points are used to determine a converged binding energy. The FEC orientation with the lowest binding energy is used as the starting point in the following calculations.

A similar approach with an energy cutoff of 520 eV and 1x1x1 k-point is used to determine FEC binding locations on the surfaces. The LiSi and Li₁₅Si₄ surfaces are complicated, and a grid approach ensures that the entire surface is sampled to find where FEC binds with the most stability and starts to dissociate. While a course grid was applied to determine the lowest energy FEC binding configuration, a fine grid is applied to sample the entire surface to get the lowest energy binding sites on the surface. A 1 x 1 Ångstrom mesh is employed across each surface in which, for each different calculation, the FEC starts in the center of a different mesh box in its lowest energy binding configuration. The LiSi surface has x- and y-dimensions of about 9.2 and 11.1 Ångstroms, resulting in a 9x11 mesh on the surface. The Li₁₅Si₄ surface is a

square with x- and y-dimensions of about 10.2 Ångstroms each, resulting in a 10x10 mesh. Rotations about the axis perpendicular to the surface are also analyzed and include six rotations on the LiSi surface and three rotations on the Li₁₅Si₄ surface.

As FEC relaxes on the LiSi and Li₁₅Si₄ surfaces, it occasionally dissociates on the surface forming FEC breakdown products due to the low barrier kinetics. For the calculations in which FEC does not dissociate, further breakdown is initiated by manually breaking bonds and moving atoms into possible energy minima for the dissociated products, which are then relaxed again. The lowest energy configurations of FEC on the surfaces for each step in the reductive decomposition process are analyzed further. The lowest energy configurations for each step may come from different initial configurations and need not be from the same initial FEC molecule. The binding energies of the lowest energy FEC and FEC breakdown products are then converged using an energy cutoff of 520 eV and 3x3x1 k-points. Increasing the number of k-points to 5x5x1 only changes the binding energy of FEC by 3.6 meV on LiSi and 9.5 meV on Li₁₅Si₄. Increasing the cutoff energy to 600 eV only changes the binding energy of FEC by 0.7 meV on the LiSi surface and 1.6 meV on the Li₁₅Si₄ surface. The reaction energy of FEC dissociation is determined from the binding energy of the final FEC products.

Bader charges [37-40] are calculated for FEC and its breakdown products to determine the amount of charge transferred from the surface to the adsorbates as FEC dissociates. The Bader charges are calculated using 3x3x1 k-points and an energy cutoff of 520 eV. Density of states plots are also calculated for FEC on the LiSi and Li₁₅Si₄ surfaces to understand the electronic difference between the two lithium silicide surfaces. The density of states plots are calculated using 9x9x3 k-points and an energy cutoff of 520 eV.

Results and Discussion

Determining the Most Stable LiSi and Li₁₅Si₄ Surfaces

Surface energies are calculated for the low index surface facets of LiSi and Li₁₅Si₄ to determine the most stable surface facets. For the LiSi phase, five low-index surface facets are considered – the (100), (110), (011), (111), and (001) facets. The

LiSi surface facets are shown in Figure 6.3 and the surface energies are listed in Table 6.1. The (100) facet has the lowest surface energy, indicating that it is the most stable surface. The surface energies increase as $(100) < (110) \approx (011) < (111) < (001)$.

Segregation of certain elements to the surface can occur in alloys, so surface exchanges of Si for a subsurface Li are examined on the (100) facet. However, the unsubstituted (100) facet was determined to be the most stable of the surfaces and is used for further analysis of FEC breakdown on the LiSi phase.

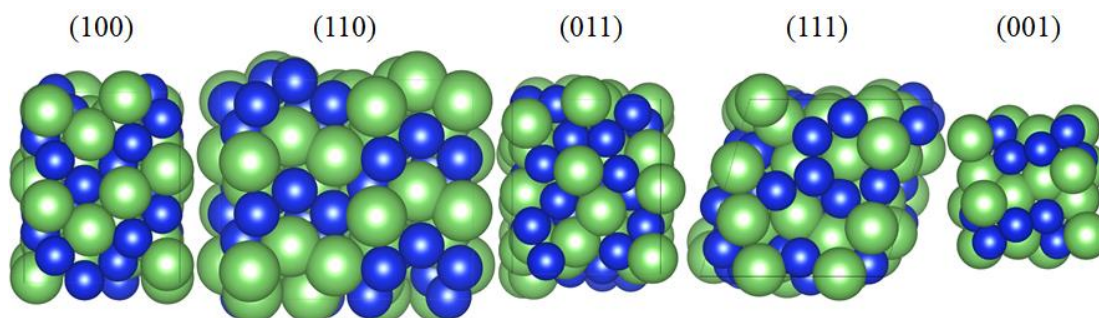


Figure 6.3 Representations of the five calculated low-index surface facets of LiSi. Larger green atoms are lithium and smaller blue atoms are silicon.

Table 6.1 Surface energies, J/m^2 , of the low-index LiSi surface facets.

Surface Facet	(100)	(110)	(011)	(111)	(001)
Surface Energy (J/m^2)	0.88	1.03	1.04	1.21	1.34

Due to the cubic nature of the $\text{Li}_{15}\text{Si}_4$ unit cell, only three low-index surface facets are considered – the (100), (110), and (111) facets. The $\text{Li}_{15}\text{Si}_4$ surface facets are shown in Figure 6.4 and the surface energies are listed in Table 6.2. The most stable facet is the (100) facet, and the surface energies increase as $(100) < (110) < (111)$. Atomic exchanges between the surface Si atoms and subsurface Li atoms are again examined, and the (100) surface with one surface exchange was found to be more stable, with the surface shown in Figure 6.4. The exchange of one surface Si atom with a subsurface Li atom, creates a Si trimer just below the surface. A second surface exchange on the (100) facet was also investigated, but this leads to a less stable surface than a surface with only one surface exchange. The (100) surface with

one surface exchange is therefore used for further analysis of FEC breakdown on the $\text{Li}_{15}\text{Si}_4$ phase.

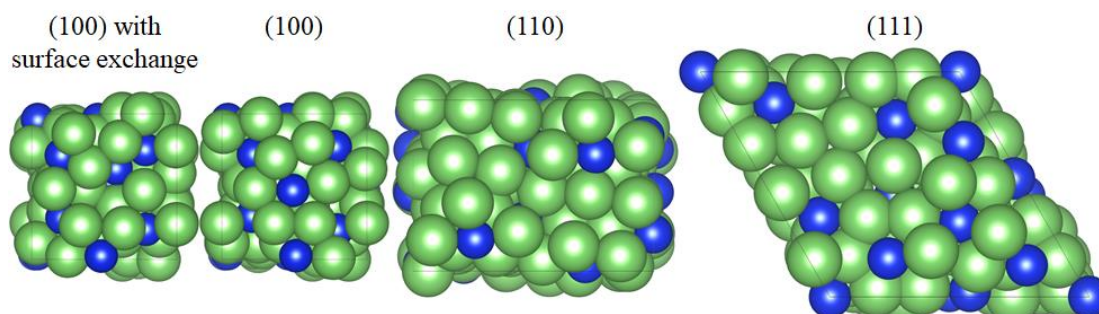


Figure 6.4 Representations of the three calculated low-index surface facets of $\text{Li}_{15}\text{Si}_4$. The (100) facet with one surface silicon atom exchanged for a subsurface lithium atom has the lowest surface energy. Larger green atoms are lithium and smaller blue atoms are silicon.

Table 6.2 Surface energies, J/m^2 , of the low-index $\text{Li}_{15}\text{Si}_4$ surface facets, including the (100) facet with a surface Si atom exchanged for a subsurface Li atom.

Surface Facet	(100) with surface exchange	(100)	(110)	(111)
Surface Energy (J/m^2)	1.05	1.12	1.18	1.21

Determining the Most Stable Fluoroethylene Carbonate Binding Configurations

The binding energies of FEC in different binding orientations on the surfaces are calculated in order to determine the most favorable configuration of FEC on the surface. Four different binding orientations of FEC on the LiSi and $\text{Li}_{15}\text{Si}_4$ surfaces are considered. As shown in Figure 6.5, two of the initial orientations have the FEC ring plane parallel to the surface, labeled F-up and F-down, and two have the FEC ring plane perpendicular to the surface, labeled O-up and O-down. After relaxation of FEC from the initial orientations, the lowest energy structures give the most stable binding configurations, shown in Figure 6.5. The most stable binding configuration for FEC on the LiSi surface has the FEC ring plane parallel to the surface. The two parallel configurations, labeled F-up and F-down, are equally favorable and are both used as starting configurations for sampling the entire LiSi surface for FEC binding. On the $\text{Li}_{15}\text{Si}_4$ surface, the most stable configuration has the FEC ring plane at an angle to the surface. This angled configuration with O_1 down and F up is taken as the

starting configuration when sampling the entire $\text{Li}_{15}\text{Si}_4$ surface for FEC binding and dissociation.

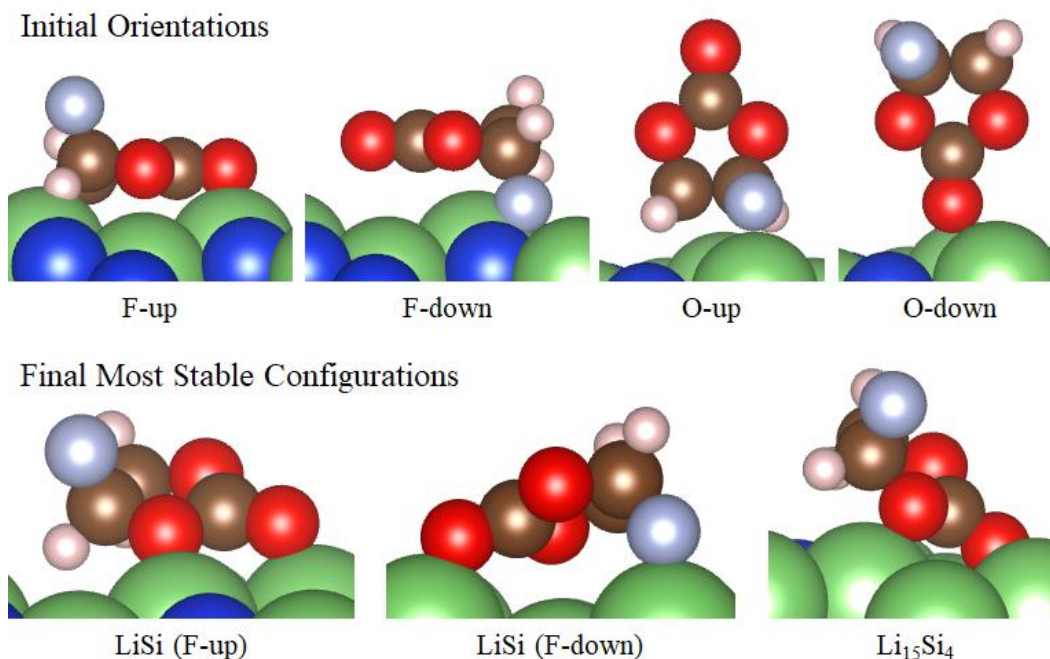


Figure 6.5 Side views of the initial FEC binding orientations and final most stable binding configurations for FEC on LiSi and $\text{Li}_{15}\text{Si}_4$. On LiSi there are two equally stable binding configurations, the F-up and F-down configurations. The elements Li, Si, O, C, H, and F are represented as green, blue, red, brown, white, and light blue, respectively.

Setting up the Surface Mesh

The binding energy landscape of FEC on the LiSi and $\text{Li}_{15}\text{Si}_4$ surfaces is complicated, and manually placing FEC at all of the different adsorption locations on the surface is not practical. Instead, we employ a fine surface mesh across the LiSi and $\text{Li}_{15}\text{Si}_4$ surfaces with one binding energy calculation for FEC in each box. The surfaces and mesh are shown in Figure 6.6. FEC in its most stable configuration is placed with its C_1 atom in the center of a different box in the surface mesh for each different calculation. The simulation cell for LiSi is repeated in the y-direction to ensure comparable surface area for LiSi and $\text{Li}_{15}\text{Si}_4$, so only the bottom five rows of the LiSi surface are explored. The entire $\text{Li}_{15}\text{Si}_4$ surface is explored.

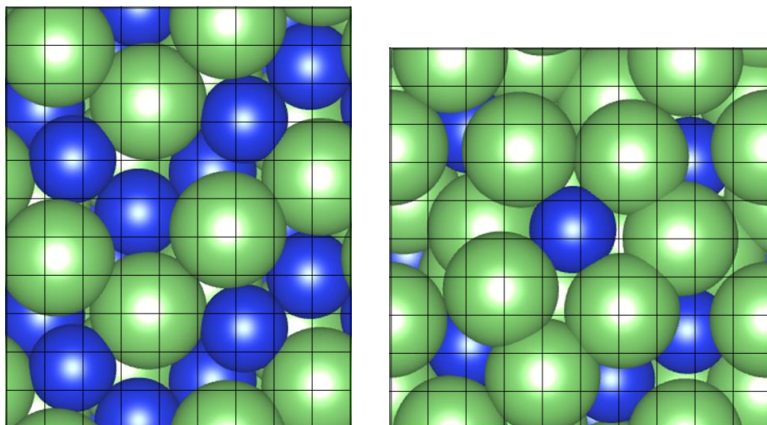


Figure 6.6 Top views of the 1 x 1 Ångstrom surface mesh employed across the LiSi (left) and $\text{Li}_{15}\text{Si}_4$ (right) surfaces to determine where FEC binds. Lithium atoms are larger and green while silicon atoms are smaller and blue.

The energy barrier for FEC dissociation on these two surfaces is small enough that FEC often dissociates during energy minimization. Figure 6.7 shows the various FEC dissociation products that form. Structure A is intact FEC in which no bonds have broken. Structure B is ring-opened FEC in which the $\text{C}_1\text{-O}_{2\text{F}}$ bond has broken. Structure C comes from Structure B in which the $\text{C}_{2\text{F}}\text{-F}$ bond has broken and F has dissociated. Structure D is formed from Structure C by the breaking of the $\text{C}_1\text{-O}_{2\text{H}}$ bond, resulting in the final products of CO, OCH_2CHO , and F. Structure E is also formed from Structure C by breaking of the $\text{O}_{2\text{H}}\text{-C}_{2\text{H}}$ bond, resulting in the formation of CO_2 , CH_2CHO , and F as final products. All five of these Structures are observed to form during FEC energy minimization on the $\text{Li}_{15}\text{Si}_4$ surface, and many also form on the LiSi surface.

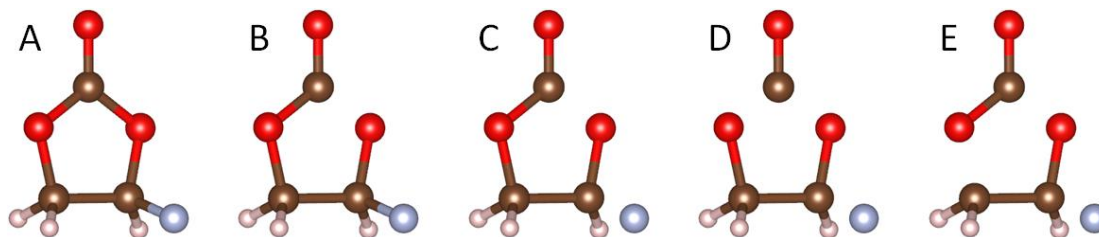


Figure 6.7 Molecular structure representations as fluoroethylene carbonate dissociates. The elements O, C, H, and F are represented by red, brown, white, and light blue, respectively.

Fluoroethylene Carbonate on LiSi

FEC is placed on the LiSi surface in each box of the lower half of the surface mesh in the F-up and F-down most stable configurations, shown in Figure 6.5, to determine where FEC binds. A total of twelve different initial configurations of FEC are used to probe the surface, in six different rotations about the axis perpendicular to the surface for each of the F-up and F-down configurations. The final products of FEC relaxation on the surface are indicated in Figure 6.8 by the different box colors. Figure 6.8a and g show the initial F-up and F-down orientations, and the subsequent images in Figure 6.8 have FEC rotated 60° counterclockwise about the C_1 atom.

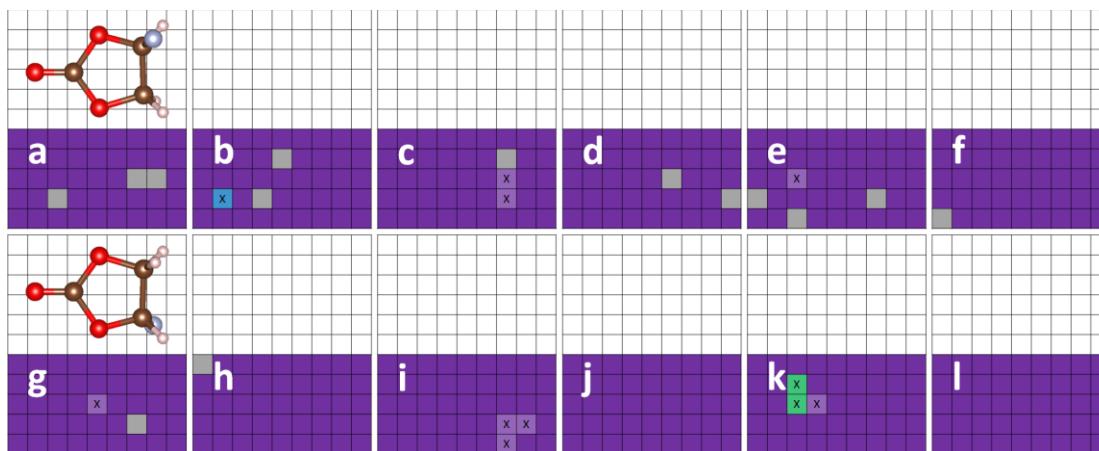


Figure 6.8 Final FEC configurations on LiSi after starting with FEC in the F-up configuration (a-f) and F-down configuration (g-l). Plots a and g start with FEC oriented as shown and subsequent plots have FEC rotated 60° counterclockwise. Each box in the lower half of the grids corresponds to a calculation in which the starting FEC orientation has its C_1 atom in the center of the surface mesh box. The colors refer to the different final Structures shown in Figure 6.7. Gray boxes indicate no FEC binding, purple boxes indicate FEC as Structure A, the blue box indicates Structure B, and green boxes indicate Structure C. A lighter box containing an X indicates that a C-Si bond is formed.

Most of the FEC minimizations on the LiSi surface result in intact FEC in Structure A, indicated by the purple boxes in Figure 6.8. The majority of the FEC adsorbates have only O-Li bonds and/or F-Li bonds present, but in a few instances the FEC molecule bends and the C_1 atom binds to a Si atom at the surface, indicated by the lighter purple boxes with an X in Figure 6.8. All spontaneous dissociation on the LiSi surface happens after a C-Si bond has formed. After binding to the surface and

forming a C-Si bond, the FEC begins to break down forming Structure B, indicated by the blue box in Figure 6.8b. Further FEC breakdown forming Structure C is observed with two different final configurations indicated by the green boxes in Figure 6.8k. The FEC dissociation Structures D and E are not observed to spontaneously form, so the three final configurations that have started to break down are further dissociated by manually moving atoms and breaking bonds followed by structural minimization. Of the three Structure D configurations that are formed, two of the configurations relax back to Structure C and only one remains as Structure D, due to similar binding energies of Structures C and D. All three Structure E configurations remained as Structure E after relaxation. The lowest energy binding configuration for each Structure is shown in Figure 6.9 and the binding energies are shown in Table 6.3.

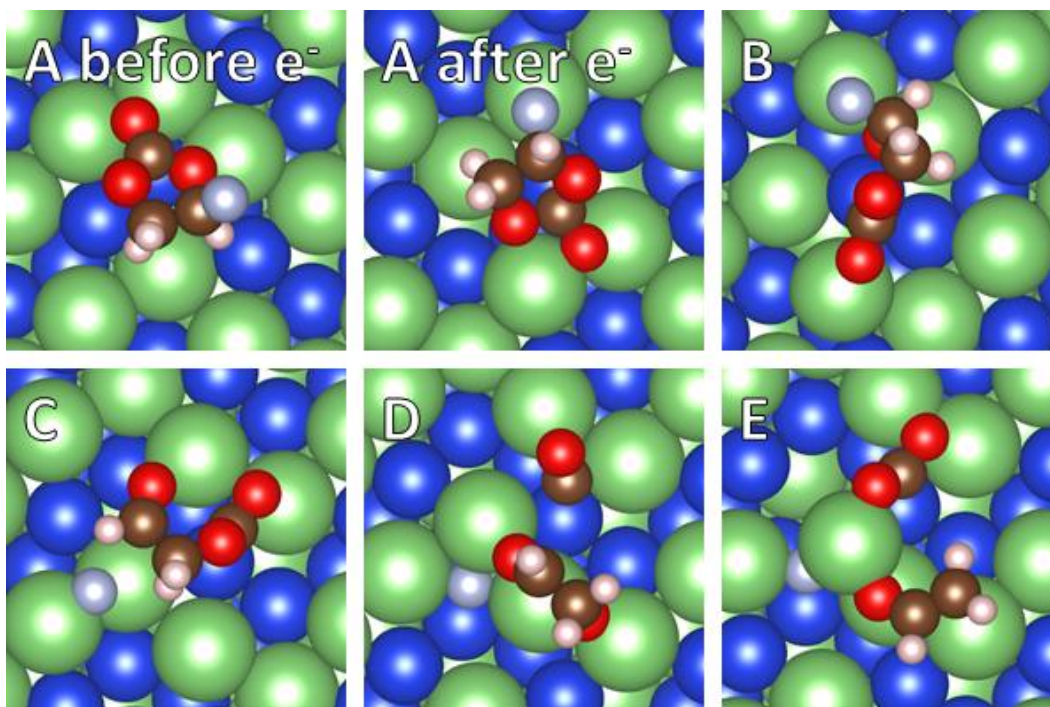


Figure 6.9 Binding configurations of FEC as it dissociates on the LiSi surface. The labels indicate the different Structures of FEC as it breaks down, shown in Figure 6.7, and the two Structure A configurations correspond to FEC before or after electron transfer from the surface. The structures represent the lowest energy configurations from all of the calculations and do not necessarily represent the same FEC molecule. The elements Li, Si, O, C, H, and F are represented as green, blue, red, brown, white, and light blue, respectively.

Table 6.3 Bader charge, $|e|$, and binding energy, eV, of FEC and its breakdown products on LiSi. Bader charges are given for each atom and the total adsorbate charge of the FEC molecule in vacuum and after FEC breaks down on the LiSi surface into the indicated Structures. Atom labels are indicated in Figure 6.2 and FEC Structures are indicated in Figure 6.7.

	vacuum	A before e^- transfer	A after e^- transfer	B	C	D	E
O ₁	-1.11	-1.23	-1.30	-1.20	-1.23	-1.12	-1.27
C ₁	2.07	2.11	0.87	0.85	0.82	-0.02	1.00
O _{2H}	-1.01	-1.02	-1.03	-1.03	-1.04	-1.32	-1.20
O _{2F}	-1.00	-1.06	-1.00	-1.40	-1.15	-1.20	-1.31
C _{2H}	0.40	0.34	0.44	0.42	0.37	0.58	-0.24
C _{2F}	0.98	0.92	0.97	0.95	0.92	0.86	0.57
H _{CH}	0.09	0.12	0.07	0.08	0.11	0.06	0.04
H _{CF}	0.12	0.13	0.04	0.11	0.09	0.05	0.02
H _F	0.12	0.15	0.09	0.09	0.13	0.07	0.04
F	-0.61	-0.61	-0.65	-0.63	-0.89	-0.94	-0.92
total	0.05	-0.16	-1.49	-1.77	-1.85	-2.97	-3.28
E _{bind}	-----	-1.04	-1.65	-1.63	-2.40	-2.50	-4.54

Bader charges for the FEC breakdown structures on LiSi are calculated and the charges for the lowest energy structures are shown in Table 6.3 alongside the charges for FEC in vacuum as a comparison. After FEC binds to the surface, but before it begins to break down, a significant amount of charge is transferred to FEC. The Bader charges for Structure A before and after the electron transfer are shown in Table 6.3. The binding configuration for Structure A before and after charge transfer is similar, as can be seen in Figure 6.9, except that in the structure with the electron transfer a C-Si bond is present. The two Structure A configurations in Figure 6.9 also happen to be flipped due to different starting configurations, but this has no major impact on FEC breakdown. The final charge of FEC in Structure A after the charge transfer is $-1.49 |e|$ with the majority of the charge residing on the C₁ atom, which is the atom in the C-Si bond. An additional charge of $-0.36 |e|$ is transferred to FEC as it passes through Structure B to become Structure C for a total Structure C charge of $-1.85 |e|$. When FEC breaks down into Structure D, the total charge on CO is $-1.14 |e|$, on OCH₂CHO is $-0.89 |e|$, and on F is $-0.94 |e|$ for a total charge of $-2.97 |e|$. When FEC breaks down into Structure E, the total charge is $-3.28 |e|$ with the charge on CO₂ at $-1.48 |e|$, OCH₂CH at $-0.88 |e|$, and F at $-0.92 |e|$. The total charge for each Structure

is directly proportional to the binding energy, as seen in Table 6.3, with stronger binding Structures having a more negative charge.

The two reaction pathways observed herein for the reductive dissociation of FEC on LiSi lead to either CO/OCH₂CHO/F with a total product charge of -2.97 |e| and a reaction energy of -2.50 eV or CO₂/CH₂CHO/F with a total product charge of -3.28 |e| and a reaction energy of -4.54 eV. The reaction to make CO₂/CH₂CHO/F is much more thermodynamically favorable than the reaction to make CO/OCH₂CHO/F by -2.04 eV. Producing CO₂/CH₂CHO/F also has a greater charge transfer from the surface by -0.31 |e| compared to producing CO/OCH₂CHO/F. These two reactions are similar to the reactions proposed previously on the LiSi surface [14, 15], but now the reaction energies have been quantified and the most thermodynamically favorable reaction mechanism determined.

Fluoroethylene Carbonate on Li₁₅Si₄

A surface mesh is applied across the entire Li₁₅Si₄ surface to determine where FEC binds. The most stable starting configuration of FEC angled with O₁ down and F up, shown in Figure 6.5, is placed on the surface in three different rotations about the axis perpendicular to the surface. The final products of the FEC relaxations on Li₁₅Si₄ are indicated in Figure 6.10 by the different colored boxes. In Figure 6.10a, the FEC is oriented with the O₁ atom farthest left, in the same rotation configuration as the FEC shown in Figure 6.8a and g. The subsequent images in Figure 6.10 have FEC rotated 120° counterclockwise about the C₁ atom.

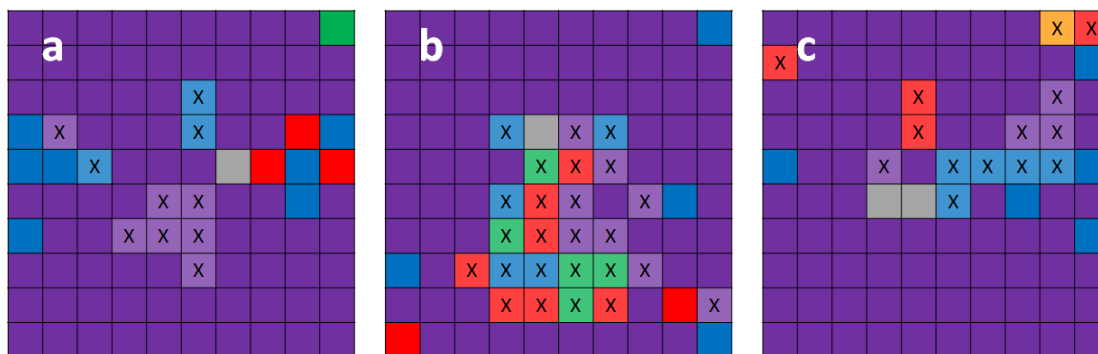


Figure 6.10 Final FEC configurations on $\text{Li}_{15}\text{Si}_4$ after starting with FEC in the angled configuration with O_1 down and F up. Plot a has the O_1 atom as the leftmost atom in FEC, and the subsequent plots have FEC rotated 120° counterclockwise. Each box of the grid corresponds to a calculation in which the starting FEC orientation has its C_1 atom in the center of the surface mesh box. The colors refer to the different final Structures shown in Figure 6.7. Gray boxes indicate no FEC binding, purple boxes indicate FEC as Structure A, blue boxes indicate Structure B, green boxes indicate Structure C, orange boxes represent Structure D, and red boxes indicate Structure E. A lighter box containing an X indicates that a C-Si bond is present.

The majority of the adsorbed FEC minimization calculations end with intact FEC bound to the $\text{Li}_{15}\text{Si}_4$ surface in Structure A, indicated by the purple boxes in Figure 6.10. Most of the final Structure A configurations have FEC bound on top of the surface with only O-Li bonds and/or F-Li bonds, however other configurations are also observed. The FEC can bind perpendicular to the surface with the $\text{O}_1\text{-C}_1$ bond bent out from the ring-plane, allowing a bond to form between the C_1 atom and a Si atom, indicated by the lighter purple boxes with an X in Figure 6.10. In addition, FEC without a C-Si bond is also stable perpendicular to the surface with a bent $\text{O}_1\text{-C}_1$ bond and is also stable buried into the surface. The binding energies of FEC buried into the surface are slightly stronger than perpendicular FEC with a C-Si bond, which are slightly stronger than perpendicular FEC without a C-Si bond. These three FEC configurations are all stronger than FEC bound on top of the surface with only O-Li and/or F-Li bonds.

The adsorbed FEC begins to break down into Structure B via a ring-opening step in the blue boxes in Figure 6.10 followed by F dissociation into Structure C in the green boxes. The orange box indicates complete dissociation of FEC into $\text{CO/OCH}_2\text{CHO/F}$ (Structure D) while red boxes indicate complete dissociation of FEC into $\text{CO}_2/\text{CH}_2\text{CHO/F}$ (Structure E). From looking at Figure 6.10, it is clear that

dissociation of FEC into $\text{CO}_2/\text{CH}_2\text{CHO}/\text{F}$ is the most favorable reaction compared with dissociation into $\text{CO}/\text{OCH}_2\text{CHO}/\text{F}$ because there are many more red boxes than orange boxes. Spontaneous breakdown of FEC on the $\text{Li}_{15}\text{Si}_4$ surface is observed with or without a C-Si bond. On the LiSi surface, a C-Si bond was needed before FEC could break down, but this is not the case on the $\text{Li}_{15}\text{Si}_4$ surface. This has not been reported in the literature previously, with all computational studies indicating the presence of a C-Si bond in spontaneous FEC decomposition [13-15]. For all final FEC configurations on $\text{Li}_{15}\text{Si}_4$ besides Structure D, all of the Structures are observed to exist both with or without a C-Si bond present. Binding configurations of FEC on the $\text{Li}_{15}\text{Si}_4$ surface are shown in Figure 6.11 for each Structure with the lowest binding energy. The binding energies for the lowest energy Structures are shown in Table 6.4.

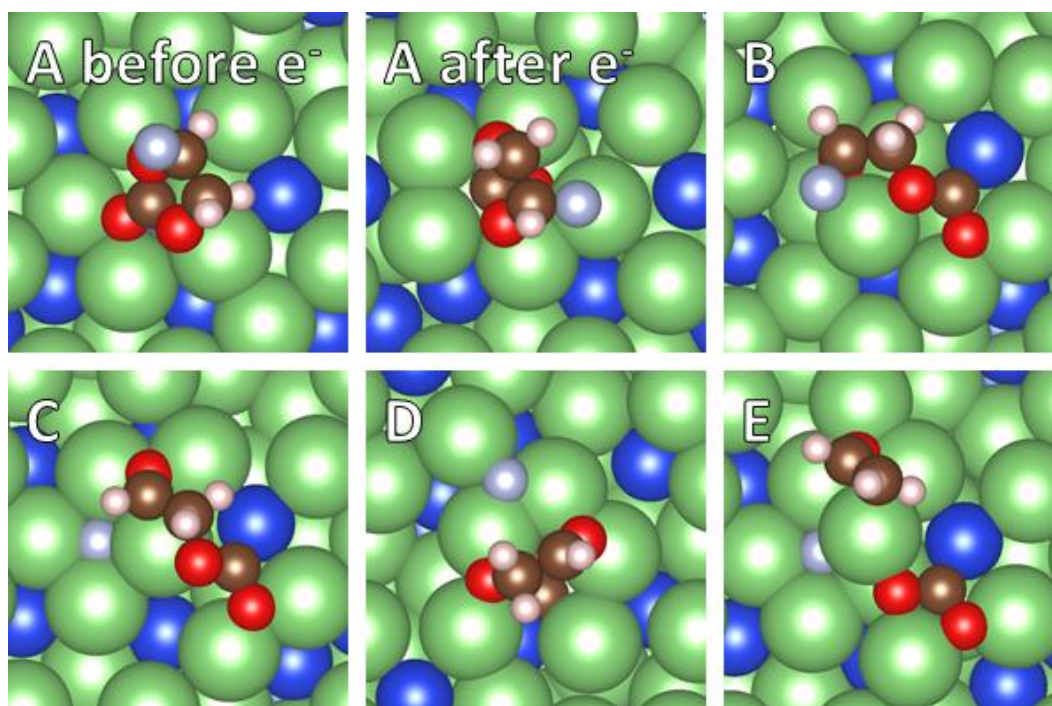


Figure 6.11 Binding configurations of FEC as it dissociates on the $\text{Li}_{15}\text{Si}_4$ surface. The labels indicate the different Structures of FEC as it breaks down, shown in Figure 6.7, and the two Structure A configurations correspond to FEC before or after electron transfer from the surface. The structures represent the lowest energy configurations from all of the calculations and do not represent the same FEC molecule. The elements Li, Si, O, C, H, and F are represented as green, blue, red, brown, white, and light blue, respectively.

Table 6.4 Bader charges, $|e|$, and binding energies, eV, for FEC and its breakdown products on $\text{Li}_{15}\text{Si}_4$. Bader charges are given for each atom and the total adsorbate charge of FEC molecule in vacuum and after FEC breaks down on the $\text{Li}_{15}\text{Si}_4$ surface into the indicated Structures. Atom labels are indicated in Figure 6.2 and FEC Structures are indicated in Figure 6.7.

	vacuum	A before e^- transfer	A after e^- transfer	B	C	D	E
O_1	-1.11	-1.30	-1.40	-1.30	-1.29	-1.37	-1.29
C_1	2.07	2.07	0.68	0.43	0.57	-0.58	0.62
$\text{O}_{2\text{H}}$	-1.01	-1.07	-1.06	-1.06	-1.01	-1.32	-1.31
$\text{O}_{2\text{F}}$	-1.00	-1.06	-1.07	-1.42	-1.32	-1.23	-1.38
$\text{C}_{2\text{H}}$	0.40	0.28	0.39	0.37	0.22	0.62	-0.17
$\text{C}_{2\text{F}}$	0.98	0.90	0.96	1.00	0.51	0.87	0.42
H_{CH}	0.09	0.16	0.05	0.03	0.07	0.03	0.06
H_{CF}	0.12	0.13	0.10	0.09	0.05	0.04	0.07
H_{F}	0.12	0.15	0.12	0.03	0.05	0.07	0.06
F	-0.61	-0.61	-0.65	-0.63	-0.97	-0.92	-0.97
total	0.05	-0.35	-1.89	-2.46	-3.10	-3.79	-3.89
E_{bind}	-----	-1.37	-2.80	-4.80	-5.87	-4.70	-8.95

The Bader charges for each step in the reductive decomposition of FEC on the $\text{Li}_{15}\text{Si}_4$ surface are shown in Table 6.4 for the lowest binding energy configuration of each Structure. Structure A on the surface is present before and after charge is transferred from the surface to FEC, with the charge for each configuration in Table 6.4 and the lowest energy binding configurations shown for each in Figure 6.11. The configuration of Structure A on the $\text{Li}_{15}\text{Si}_4$ surface before and after electron transfer is very different, in contrast to what was observed on the LiSi surface. Before charge transfer, FEC is bound on top of the surface, but the FEC configuration after charge transfer either has a C-Si bond or has FEC buried into the surface. The image in Figure 6.11 of Structure A after electron transfer is shown for FEC buried into the surface, however the FEC configuration is similar for Structure A with a C-Si bond. Stronger binding corresponds with a larger charge transfer, as seen in Table 6.3 and Table 6.4. Because buried Structure A binds slightly stronger than Structure A with a C-Si bond, buried Structure A also has a slightly more negative charge. The charge on Structure A after electron transfer is $-1.89 |e|$ with most of the charge residing on the C_1 atom, which would be the atom in the C-Si bond if it were present.

An additional charge of $-1.21 |e|$ is transferred to the FEC breakdown product as it becomes Structure C, with the charge distributing itself throughout all the atoms. If the reaction proceeds to Structure D, an additional $-0.69 |e|$ is transferred from the anode for a total product charge of $-3.79 |e|$. The final charge on CO is $-1.95 |e|$, on OCH₂CHO is $-0.91 |e|$, and on F is $-0.92 |e|$. If the reaction proceeds to Structure E from Structure C, an additional $-0.79 |e|$ is transferred for a total product charge of $-3.89 |e|$. This leaves CO₂ with a charge of $-1.98 |e|$, CH₂CHO with a charge of $-0.94 |e|$, and F with a charge of $-0.97 |e|$.

The two reaction mechanisms observed herein for the breakdown of FEC on Li₁₅Si₄ are similar to reaction mechanisms proposed previously [14, 15], but now the reaction energy is quantified. The reaction producing CO/OCH₂CHO/F has a reaction energy of -4.70 eV and a total product charge of $-3.79 |e|$ while the reaction producing CO₂/CH₂CHO/F has a reaction energy of -8.95 eV and a total product charge of $-3.89 |e|$. The reaction producing CO₂/CH₂CHO/F transfers $-0.10 |e|$ more charge and is -4.25 eV more favorable than the reaction producing CO/OCH₂CHO/F, meaning that Structure E contains the most favorable products for FEC decomposition on Li₁₅Si₄.

Comparing Fluoroethylene Carbonate Reduction on LiSi and Li₁₅Si₄

The decomposition products of FEC on the LiSi and Li₁₅Si₄ surfaces are the same, in agreement with a previous studies that found the FEC reduction products to be independent of the degree of silicon lithiation [15]. The difference between the LiSi and Li₁₅Si₄ surfaces is in the FEC reductive decomposition reaction energies and the amount of charge transferred. FEC dissociates almost two times more favorably on the Li₁₅Si₄ surface than the LiSi surface with a larger amount of charge transferred to the FEC products on the Li₁₅Si₄ surface. On both surfaces, forming CO₂/CH₂CHO/F is much more favorable than forming CO/OCH₂CHO/F. Producing CO/OCH₂CHO/F is -2.20 eV more favorable on Li₁₅Si₄ than LiSi and producing CO₂/CH₂CHO/F is -4.41 eV more favorable on Li₁₅Si₄ than LiSi. On the Li₁₅Si₄ surface compared to the LiSi surface, $-0.82 |e|$ more charge is transferred to CO/OCH₂CHO/F while $-0.61 |e|$ more charge is transferred to CO₂/CH₂CHO/F.

The density of states plots of FEC on the LiSi and Li₁₅Si₄ surfaces, shown in Figure 6.12, are calculated to understand the difference between the two surfaces. The density of states plots show the number of electronic states at each electronic energy level relative to the Fermi level, and here represent intact FEC on the surface before charge transfer or FEC bond breaking occurs. The bands shown in Figure 6.12 represent the total s and p states and the surface band includes all of the Li and Si atoms in the slab. Once adsorbed on the surface, the lowest unoccupied electronic states of FEC line up with the surface electronic states at the Fermi level. As can be seen in Figure 6.12, the number of LiSi surface electronic states almost goes to zero near the Fermi level, while the number of Li₁₅Si₄ surface electronic states remains continuous around the Fermi level. This indicates that the Li₁₅Si₄ surface is more metallic with a continuous valence band and conduction band, which can be attributed to the higher amount of Li metal in the surface. The LiSi surface almost has a band gap separating the valence band and the conduction band, which is due to LiSi having an equal ratio of conducting Li and semiconducting Si.

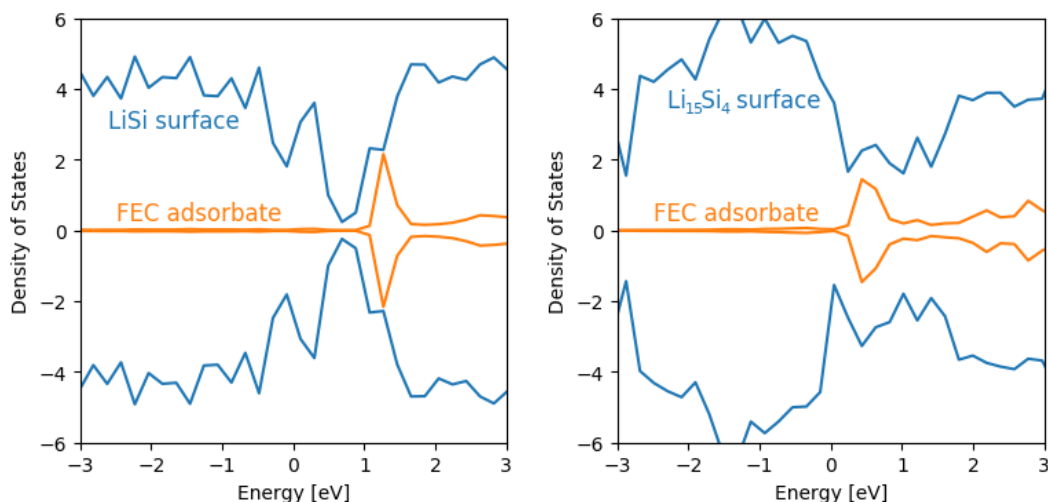


Figure 6.12 Density of states plots of intact FEC on the LiSi and Li₁₅Si₄ surfaces before charge transfer or decomposition occurs. The density of states are the total s and p states, and the electronic energy is relative to the Fermi energy.

Conclusions

The reductive decomposition of fluoroethylene carbonate (FEC) on LiSi and Li₁₅Si₄ was explored using density functional theory. The same two FEC breakdown mechanisms are observed on both surfaces, but with very different reaction energies and slightly different charge transfer amounts. The most favorable dissociation mechanism produces CO₂, CH₂CHO, and F, but a mechanism to produce CO, OCH₂CHO, and F is also observed. On the LiSi surface, the FEC reductive decomposition to CO, OCH₂CHO, and F has a reaction energy of -2.50 eV and the products have a total charge of -2.97 |e|. The reductive decomposition to CO₂, CH₂CHO, and F on the LiSi surface has a reaction energy of -4.54 eV and the FEC products have a total charge of -3.28 |e|. On the Li₁₅Si₄ surface, the reaction to produce CO, OCH₂CHO, and F has a reaction energy of -4.70 eV and the products have a total charge of -3.79 |e|. The reaction to produce CO₂, CH₂CHO, and F on the Li₁₅Si₄ surface has a reaction energy of -8.95 eV and the products have a total charge of -3.89 |e|.

The breakdown of FEC on both the LiSi and Li₁₅Si₄ surfaces is very exothermic and likely to be fast. More charge is transferred to the FEC breakdown products on the Li₁₅Si₄ surface than on the LiSi surface. Decomposition of FEC is almost two times more favorable on the Li₁₅Si₄ surface compared to the LiSi surface. This implies that at higher lithiation states of the silicon anode, or higher charge states of the battery, FEC will break down much more readily.

Acknowledgements

This material is based upon work supported by the U. S. Department of Energy, Office of Science, Office of Workforce Development for Teachers and Scientists, Office of Science Graduate Student Research (SCGSR) program. The SCGSR program is administered by the Oak Ridge Institute for Science and Education (ORISE) for the DOE. ORISE is managed by ORAU under contract number DE-SC0014664. Use of the Center for Nanoscale Materials, an Office of Science user facility, is supported by the U. S. Department of Energy, Office of

Science, Office of Basic Energy Sciences, under contract number DE-AC02-06CH11357.

References

- [1] K. Feng, M. Li, W.W. Liu, A.G. Kashkooli, X.C. Xiao, M. Cai, Z.W. Chen, Silicon-Based Anodes for Lithium-Ion Batteries: From Fundamentals to Practical Applications, *Small*, 14 (2018).
- [2] W. Luo, X.Q. Chen, Y. Xia, M. Chen, L.J. Wang, Q.Q. Wang, W. Li, J.P. Yang, Surface and Interface Engineering of Silicon-Based Anode Materials for Lithium-Ion Batteries, *Advanced Energy Materials*, 7 (2017).
- [3] A. Franco Gonzalez, N.-H. Yang, R.-S. Liu, Silicon Anode Design for Lithium-Ion Batteries: Progress and Perspectives, *The Journal of Physical Chemistry C*, 121 (2017) 27775-27787.
- [4] A.P. Wang, S. Kadam, H. Li, S.Q. Shi, Y. Qi, Review on Modeling of the Anode Solid Electrolyte Interphase (SEI) for Lithium-Ion Batteries, *NPJ Computational Materials*, 4 (2018).
- [5] S. Zhang, M.N. He, C.C. Su, Z.C. Zhang, Advanced Electrolyte/Additive for Lithium-Ion Batteries with Silicon Anode, *Current Opinion in Chemical Engineering*, 13 (2016) 24-35.
- [6] C.K. Chan, R. Ruffo, S.S. Hong, Y. Cui, Surface Chemistry and Morphology of the Solid Electrolyte Interphase on Silicon Nanowire Lithium-Ion Battery Anodes, *Journal of Power Sources*, 189 (2009) 1132-1140.
- [7] M.Y. Nie, D.P. Abraham, Y.J. Chen, A. Bose, B.L. Lucht, Silicon Solid Electrolyte Interphase (SEI) of Lithium Ion Battery Characterized by Microscopy and Spectroscopy, *Journal of Physical Chemistry C*, 117 (2013) 13403-13412.
- [8] N.-S. Choi, K.H. Yew, K.Y. Lee, M. Sung, H. Kim, S.-S. Kim, Effect of Fluoroethylene Carbonate Additive on Interfacial Properties of Silicon Thin-Film Electrode, *Journal of Power Sources*, 161 (2006) 1254-1259.
- [9] C. Xu, F. Lindgren, B. Philippe, M. Gorgoi, F. Bjorefors, K. Edstrom, T. Gustafsson, Improved Performance of the Silicon Anode for Li-Ion Batteries: Understanding the Surface Modification Mechanism of Fluoroethylene Carbonate as an Effective Electrolyte Additive, *Chemistry of Materials*, 27 (2015) 2591-2599.
- [10] E. Markevich, K. Fridman, R. Sharabi, R. Elazari, G. Salitra, H.E. Gottlieb, G. Gershinsky, A. Garsuch, G. Semrau, M.A. Schmidt, D. Aurbach, Amorphous Columnar Silicon Anodes for Advanced High Voltage Lithium Ion Full Cells: Dominant Factors Governing Cycling Performance, *Journal of the Electrochemical Society*, 160 (2013) A1824-A1833.

- [11] F.A. Soto, J.M. Martinez de la Hoz, J.M. Seminario, P.B. Balbuena, Modeling Solid-Electrolyte Interfacial Phenomena in Silicon Anodes, *Current Opinion in Chemical Engineering*, 13 (2016) 179-185.
- [12] J.M. Martinez de la Hoz, K. Leung, P.B. Balbuena, Reduction Mechanisms of Ethylene Carbonate on Si Anodes of Lithium-Ion Batteries: Effects of Degree of Lithiation and Nature of Exposed Surface, *ACS Applied Materials & Interfaces*, 5 (2013) 13457-13465.
- [13] K. Leung, S.B. Rempe, M.E. Foster, Y. Ma, J.M. Martinez de la Hoz, N. Sai, P.B. Balbuena, Modeling Electrochemical Decomposition of Fluoroethylene Carbonate on Silicon Anode Surfaces in Lithium Ion Batteries, *Journal of the Electrochemical Society*, 161 (2014) A213-A221.
- [14] J.M. Martinez de la Hoz, F.A. Soto, P.B. Balbuena, Effect of the Electrolyte Composition on SEI Reactions at Si Anodes of Li-Ion Batteries, *Journal of Physical Chemistry C*, 119 (2015) 7060-7068.
- [15] J.M. Martinez de la Hoz, P.B. Balbuena, Reduction Mechanisms of Additives on Si Anodes of Li-Ion Batteries, *Physical Chemistry Chemical Physics*, 16 (2014) 17091-17098.
- [16] A. Carvalho, M.J. Rayson, P.R. Briddon, S. Manzhos, Effect of the adsorption of ethylene carbonate on Si surfaces on the Li insertion behavior, *Chemical Physics Letters*, 585 (2013) 157-161.
- [17] J. Rohrer, P. Kaghazchi, Structure Sensitivity in the Decomposition of Ethylene Carbonate on Si Anodes, *Chemphyschem*, 15 (2014) 3950-3954.
- [18] Y. Ma, P.B. Balbuena, DFT Study of Reduction Mechanisms of Ethylene Carbonate and Fluoroethylene Carbonate on Li+-Adsorbed Si Clusters, *Journal of the Electrochemical Society*, 161 (2014) E3097-E3109.
- [19] Y.X. Wang, S. Nakamura, M. Ue, P.B. Balbuena, Theoretical Studies to Understand Surface Chemistry on Carbon Anodes for Lithium-Ion Batteries: Reduction Mechanisms of Ethylene Carbonate, *Journal of the American Chemical Society*, 123 (2001) 11708-11718.
- [20] G. Kresse, J. Hafner, Ab Initio Molecular Dynamics for Liquid Metals, *Physical Review B*, 47 (1993) 558-561.
- [21] G. Kresse, J. Hafner, Ab Initio Molecular-Dynamics Simulation of the Liquid-Metal-Amorphous-Semiconductor Transition in Germanium, *Physical Review B*, 49 (1994) 14251-14269.
- [22] G. Kresse, J. Furthmuller, Efficiency of Ab-Initio Total Energy Calculations for Metals and Semiconductors Using a Plane-Wave Basis Set, *Computational Materials Science*, 6 (1996) 15-50.
- [23] G. Kresse, J. Furthmuller, Efficient Iterative Schemes for Ab Initio Total-Energy Calculations Using a Plane-Wave Basis Set, *Physical Review B*, 54 (1996) 11169-11186.

- [24] J.P. Perdew, K. Burke, M. Ernzerhof, Generalized Gradient Approximation Made Simple, *Physical Review Letters*, 77 (1996) 3865-3868.
- [25] J.P. Perdew, K. Burke, M. Ernzerhof, Errata: Generalized Gradient Approximation Made Simple, *Physical Review Letters*, 78 (1997) 1396-1396.
- [26] P.E. Blöchl, Projector Augmented-Wave Method, *Physical Review B*, 50 (1994) 17953-17979.
- [27] G. Kresse, D. Joubert, From Ultrasoft Pseudopotentials to the Projector Augmented-Wave Method, *Physical Review B*, 59 (1999) 1758-1775.
- [28] S. Grimme, Accurate Description of van der Waals Complexes by Density Functional Theory Including Empirical Corrections, *Journal of Computational Chemistry*, 25 (2004) 1463-1473.
- [29] S. Grimme, J. Antony, S. Ehrlich, H. Krieg, A Consistent and Accurate Ab Initio Parametrization of Density Functional Dispersion Correction (DFT-D) for the 94 Elements H-Pu, *Journal of Chemical Physics*, 132 (2010).
- [30] A. Jain, S.P. Ong, G. Hautier, W. Chen, W.D. Richards, S. Dacek, S. Cholia, D. Gunter, D. Skinner, G. Ceder, K.A. Persson, Commentary: The Materials Project: A Materials Genome Approach to Accelerating Materials Innovation, *APL Mater.*, 1 (2013) 11.
- [31] Y. Kubota, M.C.S. Escano, H. Nakanishi, H. Kasai, Electronic Structure of LiSi, *Journal of Alloys and Compounds*, 458 (2008) 151-157.
- [32] K. Persson, Materials Data on LiSi (SG:88) by Materials Project, 2016.
- [33] Y. Kubota, M.C.S. Escano, H. Nakanishi, H. Kasai, Crystal and Electronic Structure of Li₁₅Si₄, *Journal of Applied Physics*, 102 (2007).
- [34] K. Persson, Materials Data on Li₁₅Si₄ (SG:220) by Materials Project, 2016.
- [35] S.R. Bahn, K.W. Jacobsen, An Object-Oriented Scripting Interface to a Legacy Electronic Structure Code, *Computing in Science & Engineering*, 4 (2002) 56-66.
- [36] A.H. Larsen, J.J. Mortensen, J. Blomqvist, I.E. Castelli, R. Christensen, M. Dulak, J. Friis, M.N. Groves, B. Hammer, C. Hargus, E.D. Hermes, P.C. Jennings, P.B. Jensen, J. Kermode, J.R. Kitchin, E.L. Kolsbjerg, J. Kubal, K. Kaasbjerg, S. Lysgaard, J.B. Maronsson, T. Maxson, T. Olsen, L. Pastewka, A. Peterson, C. Rostgaard, J. Schiøtz, O. Schutt, M. Strange, K.S. Thygesen, T. Vegge, L. Vilhelmsen, M. Walter, Z.H. Zeng, K.W. Jacobsen, The Atomic Simulation Environment-A Python Library for Working with Atoms, *Journal of Physics-Condensed Matter*, 29 (2017).
- [37] G. Henkelman, A. Arnaldsson, H. Jónsson, A Fast and Robust Algorithm for Bader Decomposition of Charge Density, *Computational Materials Science*, 36 (2006) 354-360.

- [38] E. Sanville, S.D. Kenny, R. Smith, G. Henkelman, Improved Grid-Based Algorithm for Bader Charge Allocation, *Journal of Computational Chemistry*, 28 (2007) 899-908.
- [39] W. Tang, E. Sanville, G. Henkelman, A Grid-Based Bader Analysis Algorithm Without Lattice Bias, *Journal of Physics-Condensed Matter*, 21 (2009).
- [40] M. Yu, D.R. Trinkle, Accurate and Efficient Algorithm for Bader Charge Integration, *Journal of Chemical Physics*, 134 (2011).

CHAPTER 7
CONCLUSION

General Conclusions

Interactions of chemical species with solid surfaces were analyzed using density functional theory. A model for calculating the surface entropy was developed, benchmarked, and implemented into existing python packages for thermodynamic and kinetic analyses. In addition, surface energies were calculated to determine reaction mechanisms and the effect of varying the surfaces on the reactions for applications in corrosion resistant metals and lithium-ion battery anodes.

The hindered translator and hindered rotor model was developed as a way to calculate partition functions and entropies of adsorbed species more accurately. The entropies can then be used in calculations of rate constant and equilibrium constants to better understand chemical reactions at solid interfaces. The two limits for calculating the entropy of an adsorbed species are the harmonic oscillator limit, which assumes that all modes of motion are vibrational modes, and the free translator and free rotor limit, which models the three modes of motion parallel to the surface as two free translators and one free rotor. The hindered translator and hindered rotor model was developed as a way to bridge the gap between the two limiting cases by representing the three modes of motion parallel to the surface as two hindered translators and one hindered rotor. When the temperature of the system is higher than the energy barrier for translation (rotation), the adsorbate can easily translate (rotate) on the surface and acts almost like a free translator (rotor). On the contrary, when the temperature of the system is lower than the energy barrier for translation (rotation), the adsorbate can only vibrate and behaves like a harmonic oscillator. The hindered translator and hindered rotor model successfully transitions between the two limiting cases and may be applied at any temperature. In addition to calculating the entropy differently with the hindered translator and hindered rotor model, the lowest frequencies, which correspond to motion parallel to the surface, are also calculated differently. The harmonic oscillator approximation models the potential energy surface as a parabolic surface and gives frequencies that are too high, resulting in an entropy that is too low. The hindered translator and hindered rotor model instead models the potential energy surface as a sinusoidal surface and gives smaller frequencies that result in larger entropies.

The hindered translator and hindered rotor model was used to determine surface entropies of methanol, propane, ethane, and methane on a Pt(111) surface, and the entropies were found to agree favorably with experiments. Bajpai et al. [1] calculated the free energies and entropies of H, C, N, O, and S on Au(100) and Pt(100) and found the hindered translator model to perform best when the potential energy surface is flatter, such as when the adsorbate is bound at a bridge site or has a low translational energy barrier, and the harmonic oscillator approximation to perform better when the adsorbate has a higher translational energy barrier and the potential energy surface is steeper. Jørgensen and Grönbeck [2] extended the hindered translator model to a microkinetic model for CO oxidation on Pt(111). They found that the hindered translator model slightly skews towards the free translator model from the exact potential energy surface, but concluded that the hindered translator model performs very well for calculations of the turnover frequency, coverage, and light-off temperature. The hindered translator and hindered rotor model has also been coded into two existing python packages so that the model is more accessible and can more easily be implemented by all researchers.

The interactions of O, C, and CO with two different facets of twelve nickel-based alloy surfaces were studied to determine the influence of the surface on the CO breakdown mechanism. The CO binds similarly to all alloy surfaces and both the (100) and (111) facets, meaning that the CO breakdown mechanism depends entirely on how C and O bind to the different surfaces. The C binds weaker to all surfaces than CO binds to the surfaces, resulting in the Boudaourd reactions being endothermic on all surfaces. The (100) facet for all alloys binds C stronger than the (111) facet, resulting in the CO dissociation reaction being exothermic on all (100) surfaces and endothermic on all (111) surfaces. The pure Ni surface and Ni individually alloyed with Cu, Co, Fe, Al, and Mn bind O weakest, resulting in the dissociation of CO into C+O being less favorable on these alloy surfaces. In contrast, the Ni surfaces individually alloyed with W, V, Ti, Mo, Cr, and Nb bind O stronger and result in CO dissociation being more favorable. The CO breakdown mechanism is thermodynamically most favorable via direct CO dissociation on the (100) facet of Ni alloyed with W, Mo, V, Ti, Nb, or Cr.

The electro-reductive breakdown of fluoroethylene carbonate on the LiSi and $\text{Li}_{15}\text{Si}_4$ surfaces was studied to determine the most favorable breakdown mechanisms and to understand how the surface lithiation affects the breakdown thermodynamics. The amount of lithium in the silicon surface is a result of the charge state of the battery, with the LiSi surface corresponding to a low battery charge state and the $\text{Li}_{15}\text{Si}_4$ surface corresponding to a high battery charge state. Fluoroethylene carbonate breaks down with similar mechanisms on the two surfaces, and the breakdown is always very exothermic with a significant amount of charge transferred to the breakdown products from the surface. The most thermodynamically favorable products are CO_2 , F, and CH_2CHO , although CO, F, and OCH_2CHO are also favorable, but by about half as much. The amount of charge transferred to the breakdown products is somewhat higher on the $\text{Li}_{15}\text{Si}_4$ surface than on the LiSi surface, and the breakdown reaction energies are almost two times more favorable on the $\text{Li}_{15}\text{Si}_4$ surface than on the LiSi surface. The reductive decomposition of fluoroethylene carbonate is much more thermodynamically favorable at a high battery charge state than a low battery charge state.

Overall, the interactions of chemical species with solid surfaces have been analyzed to improved future surface reaction modeling through the hindered translator and hindered rotor model and to further understand surface reactions with applications in corrosion and lithium-ion batteries. This work should serve to advance the field of surface science.

Future Work

Initial results from the hindered translator and hindered rotor model are promising, showing that it can be a practical and effective model for calculating the entropy of adsorbed species. Future work should be done to more comprehensively evaluate the hindered translator and hindered rotor model for all types of adsorbates. This could be done by making a microkinetic model of a larger reaction mechanism, such as the complete oxidation of acetic acid on a Pd surface. Acetic acid oxidation involves 23 different adsorbates of various size, surface binding locations (hollow, top, bridge), adsorbate binding configurations (monodentate, bidentate, tridentate),

binding strengths, translational and rotational barrier heights, and number of surface parallel modes of motion, making acetic acid oxidation a great reaction scheme to investigate. Well studied reaction mechanisms such as methanol oxidation could also be a good candidate for future study because new models can readily be compared to experimental data and previous microkinetic models.

Another interesting problem in analyzing the kinetics of surface reactions is in calculating the partition function and entropy of a transition state. The hindered translator and hindered rotor model was designed as an alternative to the harmonic oscillator approximation for adsorbates in their true minimum energy state, but there is no alternative to the harmonic oscillator approximation for transition states. A better model for calculating the partition function and entropy of the transition state would further advance microkinetic modeling of surface reactions.

The development of corrosion resistant alloys is a challenge that is complicated by the abundant number of elements and the even more generous number of element combinations. Future work to develop corrosion resistant materials for supercritical CO₂ environments should include the modeling of surfaces containing multiple alloying elements with the goal to identify trends in alloying composition and corrosion resistance, which could lead to new design principles. The interactions of the corrosive species with nickel surfaces containing a single alloying element have been understood and can serve as a foundation to understand the interactions of the corrosive species on multi-element alloys. Commercial alloys contain many alloying elements and this needs to be taken into account.

The chemical composition of a lithium-ion battery electrolyte is quite complex and a logical next step in understanding electrolyte breakdown on silicon anode surfaces would be to include multiple electrolyte molecules. It is computationally more challenging to sample the configurations of multiple electrolyte molecules, but a next step could be to include an ethylene carbonate molecule along with the fluoroethylene carbonate or include a second fluoroethylene carbonate molecule. In a battery, one electrolyte molecule may start to breakdown on the surface and then react with another nearby electrolyte molecule to form an oligomer. The breakdown reaction mechanism and energetics of one fluoroethylene carbonate molecule has

been explored, but with more electrolyte molecules present, other reaction mechanisms may take place.

References

- [1] A. Bajpai, P. Mehta, K. Frey, A.M. Lehmer, W.F. Schneider, Benchmark First-Principles Calculations of Adsorbate Free Energies, *ACS Catalysis*, 8 (2018) 1945-1954.
- [2] M. Jørgensen, H. Grönbeck, Adsorbate Entropies with Complete Potential Energy Sampling in Microkinetic Modeling, *Journal of Physical Chemistry C*, 121 (2017) 7199-7207.